Design and Development of Laser Patterned Eco-Friendly Nanogenerators for Energy Harvesting Applications

Ph.D. Thesis

By

MANIKANDAN M

DEPARTMENT OF MECHANICAL ENGINEERING

INDIAN INSTITUTE OF TECHNOLOGY INDORE

OCTOBER 2022

Design and Development of Laser Patterned Eco-Friendly Nanogenerators for Energy Harvesting Applications

A THESIS

Submitted in partial fulfillment of the
requirements for the award of the degree
of
DOCTOR OF PHILOSOPHY

by
MANIKANDAN M

DEPARTMENT OF MECHANICAL ENGINEERING
INDIAN INSTITUTE OF TECHNOLOGY INDORE
OCTOBER 2022

INDIAN INSTITUTE OF TECHNOLOGY INDORE

I hereby certify that the work which is being presented in the thesis entitled **Design and Development of Laser Patterned Eco-Friendly Nanogenerators for Energy Harvesting Applications** in the partial fulfilment of the requirements for the award of the degree of **DOCTOR OF PHILOSOPHY** and submitted in the **DEPARTMENT OF MECHANICAL ENGINEERING, Indian Institute of Technology Indore**, is an authentic record of my own work carried out during the time period from July 2018 to October 2022 under the supervision of Prof. I. A. Palani, Professor, Department of Mechanical Engineering and Prof. Vipul Singh, Professor, Department of Electrical Engineering.

The matter presented in this thesis has not been submitted by me for the award of any other degree of this or any other institute.

signature of the student with date
(MANIKANDAN M)

This is to certify that the above statement made by the candidate is correct to the best of my/our knowledge.

Signature of Thesis Supervisor
Prof. I. A. PALANI

Signature of Thesis Supervisor
Prof. VIPUL SINGH

MANIKANDAN M. has successfully given his Ph.D. Oral Examination held on **04-October-2022**

Signature of Thesis Supervisor
Prof. I.A.PALANI

Signature of Thesis Supervisor
Prof. VIPUL SINGH

ACKNOWLEDGMENTS

I would like to express my sincere gratitude to my supervisors, **Prof. I. A. Palani and Prof. Vipul Singh,** for invigorating motivation and guidance. Prof. I. A. Palani has constantly supported me with the necessary facilities to complete the work in stipulated tenure successfully. His consistent discussions have yielded fruitful suggestions and ideas to carry out the thesis work comprehensively. He has taught me the value of hard work in any profession and ethics, which helped me swiftly through the rollercoaster of my Ph.D. I sincerely thank Prof. Vipul Singh for sharing his deep knowledge. His insightful remarks and questions have helped me in acquiring a better understanding and elevating the quality of my work.

I convey special thanks to **Prof. Wenzhuo Wu, Department of Industrial Engineering, Purdue University USA** as a host of Purdue India SERB Overseas Doctoral fellowship. His constant support, valuable advice, constructive criticism, and the extensive discussion helped me accomplish my Ph.D.

I sincerely thank my senior, **Dr. Rajagopalan P.,** for his critically reviewing, irreplaceable support, and directions throughout my Ph.D. Also, I want to especially thank, **Dr. Akash Kumar, Dr. Mani Prabhu, Dr. Jayachandran S, Dr. Muralidharan M, Dr Nandhini Patra** for their support, mentorship, constant motivation and assistance in the entire duration of Ph.D. I would like to express my gratitude in particular to **Mr. Sarathkumar K** for reviewing all my manuscripts and thesis. I owe a debt of gratitude to these brilliant individuals who have contributed significantly to molding me into a persistent researcher.

I would like to thank **Prof. Suhas Joshi**, Director, IIT Indore, and **Prof. Santosh K. Sahu**, Department of Mechanical Engineering Head, for the opportunity and support to conduct my research. I thank the PSPC members **Dr. Amod Umarikar and Dr. Shailesh Kundalwal** for their valuable suggestions. I am thankful to DPGC convener **Dr. Satyanarayan Patel** for the support.

I convey my sincere thanks to the **Ministry of Human Resource and Development (MHRD),** India for funding me from July 2018 to April 2021, and the **Science Engineering Research Board** for selecting me as a candidate for Purdue-India OVDF and providing funds for one and half years. I would like to thank **Dr. Pravin Kumar,** SERB Scientist, and **Mrs. Heidi Alora,** Purdue University, for providing the necessary support during my OVDF tenure.

I am thankful to my senior **Dr. S. Shiva, Dr. Tameshwer Nath, Dr. Ashish K. Shukla, Dr. D. Suresh, Dr. Gowtham Raju, Dr. Iyyappan, Dr. Deepak Selvakumar, Dr. MS Arjun**, for their constant encouragement and discussions.

I want to thank my colleagues of opto-mechatronics laboratory, **Dr. Sooraj S Mr Anshu Shahu, Mr Arpit singh, Mr. Kaushik;** colleagues of MNRG, **Dr. Pramila, Dr. Jitesh;** colleagues of Prof. Wu laboratory **Mr Shujia Xu, Mr Meng Hao Lee, Mr Mingyi Wang, Ms Jing Jiang, Ms Rufiang** for their motivation and support in this journey.

I extend my cordial thanks to **Mr. Tapesh Parihar, Mr. Ashwin Wagh, and Mr Krishna Tomar, Mr Kinny Pandey, Mr Nitin** of IIT Indore for their kind cooperation and support.

I would like to express my gratitude towards **Dr U Natarajan** for his mentorship during my M.E. (2015-2017) which sowed seeds of research and encouraged me to pursue Ph.D. Also, I express my gratitude to **Mrs Shanmuga Priya** and **Dr Mohana Sundari** for their support and encouragement.

I would further like to thank my friends **Dr. Dhivya Krishnan, Mr. Vignesh P, Mr. Parthiban R**, **Mr. Simson, Mr. Annamalai, Mr Sakthi Sadhasivam, Ms Hema Priya, Ms Surya S, Mrs Athira** for always being enthusiast and encouraging.

None of this would have been possible without the love and support of my families **Mr Muthu (Appa), Mrs Sagunthala (Amma), Mrs Sabitha Prakasam (Akka), Mr Rathinam (Thambi), Ms Haritha (pappa)**. Especially, I am thankful to my mother **Mrs Ponnaya Muthu (Amma)** for her trust and constant motivation throughout my life which has enabled to be better person who I am today. Also, I wish to thank my sisters, Ms Sasi, Ms Varsha, Dr Janani for their unconditional love and support.

Last but not least, I wish to thank my wife **Dr Indumathi** and Daughter **Ms Tamizhaadhini,** for showering me with endless love and who supporting and encouraging me in all the tough situation.

Dedicated to

My Amma (Mrs Ponnaya)

my wife (Dr Indumathi)

my daughter (Ms Tamizhaadhini)

for their unconditional love and care

List of Publications

Peer-reviewed journals:

1. **Manikandan M,** Rajagopalan Pandey, Shujia Xu, Palani IA, Vipul Singh, Xiaozhi Wang, Wenzhuo Wu, 2021 "Enhancement of Patterned Triboelectric Output Performance by Interfacial polymer Layer for Energy Harvesting Application" Nanoscale, 13, 20615-20624. **(IF: 8.307)**
2. **Manikandan M,** Rajagopalan P, Xiaozhi Wang, Arunkumar C, Palani IA, Vipul Singh,2020 "Enhancement of Triboelectric Nanogenerator Output Performance by Laser 3D-Surface Pattern Method for Energy Harvesting Application" Nano Energy (78) P, 105205. **(IF:19.069)**
3. **Manikandan M,** P Rajagopalan, Nandhini Patra, Jayachandran S, Muralidharan M, Mani prabu SS, I.A Palani, Vipul Singh "Development of Sn doped ZnO based Ecofriendly Piezoelectric Nanogenerator for Energy Harvesting Application" IOP Nanotechnology 31 (2020) 185401 (9pp). **(IF: 3.953).**
4. **Manikandan M,** Shujia Xu, Palani IA, Vipul Singh, Wenzhuo Wu, "Liquid and Wide-bandgap Semiconductor Based DC Triboelectric Nanogenerator for Energy Harvesting Application by Tribovoltaic Effect" (under review).

Oral and poster presentation:

1. **Manikandan M,** IA Palani, Vipul Singh "Enhancement of Laser patterned Triboelectric Nanogenerator for Energy Harvesting Applications" 31st Annual Meeting of Material Research Society Japan, Dec 2021.
2. **Manikandan M,** IA Palani, Vipul Singh "Development of Laser Surface Modified Triboelectric Nanogenerator for Energy Harvesting Applications" 30th Annual Meeting of Material Research Society Japan, Dec 2020.
3. **Manikandan M,** N Yashwanth, Hampa Faazil, Muralidharan M, IA Palani, Vipul Singh "Development of ZnO Nanocomposite Based Flexible and Eco-Friendly Piezoelectric Nanogenerator" COPEN-2019 conference.

Preface

This research work concentrated on developing eco-friendly piezoelectric and triboelectric nanogenerators for energy harvesting applications. The majority of eco-friendly piezo and triboelectric materials have lower output due to material properties. To enhance the device's performance, doping and laser surface modification approaches have been deployed in this work. Furthermore, both doping concentration and laser parameters are systematically optimized.

Primarily, the Zinc Oxide (ZnO)-based piezoelectric nanogenerator was fabricated and demonstrated to generate energy from a uniform and non-uniform mechanical load conditions. Different concentrations of Sn element were doped into ZnO to enhance the pristine device performance, ranging from 0-5% with an interval of 2.5%. It was noticed that 2.5% of Sn doped ZnO piezoelectric nanogenerator was optimum and generated maximum output than pristine and 5% Sn doped device. It is due to the augmentation of carrier concentration when increasing the doping percentage. Finally, all the devices were deployed into non-uniform mechanical loading conditions like musical drums to study their functionality and ability. It confirms that the device is capable to generate significant output to power the low-power electronics.

The laser power was optimized based on voltage value. It was noticed that the 30 W laser power obtained maximum output due to the enhanced surface contact area and chemical changes in the PET (Polyethylene terephthalate) material. In addition, the patterning geometries have been varied, such as line, X, and circle patterns, to study the influence of output performance. The line patterned triboelectric nanogenerator (TENG) attains higher output performance than other patterns and plain PET. Furthermore, we tested the device under various mechanical parameter conditions such as the force of 10-100 N, frequency of 1-5 Hz, and separation distance of 2-12 mm. The maximum V_{oc} of 35.7 V and I_{sc} of 0.46 μA were generated by the optimum device parameter of 50 N, 5 Hz, and 4 mm distance, respectively.

Further enhancing the line pattern TENG output, two different interfacial layers have been introduced, such as Polyvinyl alcohol (PVA) and polyethylene oxide (PEO). The PEO coated line pattern has attained a maximum V_{oc} of 131.85 V, I_{sc} of 2.323 μA, and power density of 41.6 $\mu W/cm^2$. Also, the generated power was stored in a commercial capacitor and glowed 10 LEDs with higher intensity. Therefore, the main objectives have been accomplished.

TABLE OF CONTENTS

List of Figures

List of Tables

List of Abbreviations

Notations

MEMS	Microelectromechanical system
PENG	Piezoelectric nanogenerator
TENG	Triboelectric nanogenerator
PZT	Lead Zirconium Titanate
BaTiO3	Barium Titanate
AlN	Aluminium Nitrate
ZnO	Zinc Oxide
Sn	Tin
PVDF	Polyvinyildene fluoride
GaN	Gallium nitride
PA6	Nylon 6
PET	Polyethylene terephthalate
PDMS	Polydimethylsiloxane
PTFE	Polytetrafluoroethylene
PEO	Polyethylene oxide
HMTA	Hexamethylenetetramine
PVA	Poly Vinyl Alcohol
LSP	Laser surface patterning
PEH	Piezoelectric energy harvester
LED	Lighting emitting diode
NWs	Nanowires
CTT	Conductive textile tape
CCL	Charge collecting layer
CTL	Charge transmitting layer
FESEM	Field emission scanning electron microscope
EDS	Energy dispersive spectroscopy
XRD	X-ray diffraction
FTIR	Fourier-transform infrared spectroscopy
M	Mass

SONAR	Sound navigation and ranging
V	Voltage
$\emptyset_{1,2}$	Charge
e	Electron
AC	Alternating current
cm	Centimetre
W	Watt
A	Ampere
C	Coulomb
Ω	Ohm
N	Newton
ρ	Charge Density
A	Area
σ	Surface charge density
V_{oc}	Open circuit voltage
I_{sc}	Short circuit current
d_0	Distance
R	Resistance
I	Current
P	Power
F	Farad
ε	dielectric constants

Chapter 1

Introduction

1.1 Introduction

In Industry 4.0, the miniaturization of electronics and MEMS devices are playing significant role in empowering modern human society. Devices such as intelligent sensors, actuators, and microprocessors have become an integral part of our routine activities [1-3]. The growth rate of devices connected with the human population is depicted in Figure 1.1. In such devices, electrical power is a determining factor in addressing the flexibility and portability of the device. In this regard, there is a remarkable technical challenge to power these devices and perform the required function, viz., sensing, collecting, transmitting/analyzing the data [4,5]. The issue of recharging and replacement of batteries eventually degrades the operational effectiveness of the device. As a result, integrating an energy harvesting device with electronic gadgets can supplement the battery and it will improve the viability for different applications [6]. Different kinds of energies, such as solar energy, heat energy, mechanical energy, wind energy, etc., are ubiquitous [5,7,8].

Mostly these forms of energy are harvested from the environment and converted into useful electrical potential. Among them, solar energy is an enormously available and long-lasting energy source. Also, massive research work has been conducted to develop efficient solar cells. However, it is limited to various environmental factors, like weather, location, and time. As a result, designing and developing unique methods to harvest energy in multiple forms, such as motion, sound waves, and heat, is critical in order to build energy harvesting solutions. The generated energy can be combined with batteries to meet the power demands of sensors and electronic circuits. Therefore, a self-powered system has the ability to harness the energy from ubiquitous to fulfill its power demands. Also, it will have potential applications such as

biomedical, structural monitoring, human health monitoring, and wearable technologies.

Therefore, the mechanical energy harvester has been extensively attracted in recent years due to wide resource availability, gives higher output with low fabrication cost, flexibility, and no external power source required. This chapter provides a review of different mechanical energy harvesting technologies for low-power electronics, as well as an introduction to piezoelectric and triboelectric energy harvesting, in order to set the stage for this thesis study.

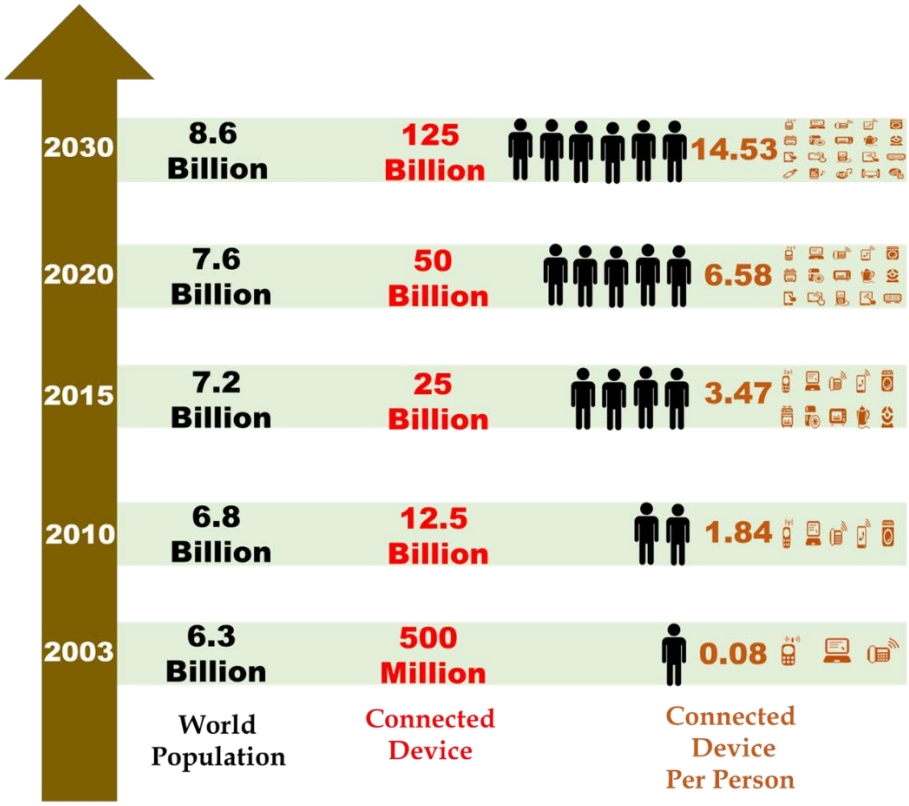

Figure 1.1 statistics of connected electronic devices with human population *Source: Cisco IBSG blog*.

1.2 Mechanical energy harvesting:

In particular, mechanical energies are abundantly available and specialized due to motion-related applications. Those mechanical stimuli are present in the form of stress, elongation, vibration, and tension, even in human movements, respiration, cardiac pulse, motor vehicle motion, and vibrations.

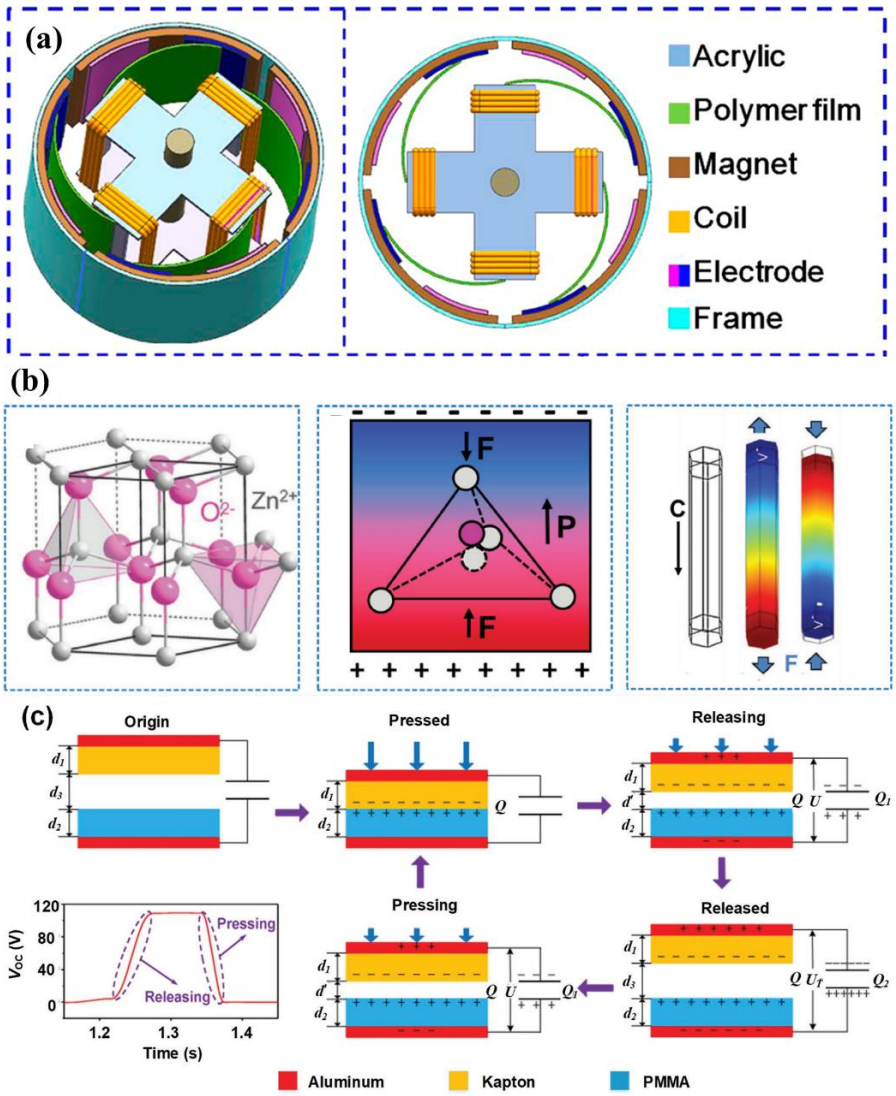

Figure 1.2 (a)schematic diagram of hybrid electromagnetic and TENG [9], (b) PENG, and (c) TENG working mechanism [15,16]

Conventionally three mechanisms have been used to convert mechanical to electrical energy.

- Electromagnetic effect
- Piezoelectric effect
- Triboelectric effect

Electromagnetic generator (EMG) is working based on Faraday's law of induction. It consists of macro-micro features, an electric coil, and magnetic materials, though it has limitations in the miniaturization of the EMG device fabrication (Figure 1.2(a)) [9,10]. Hence, to harvest mechanical energy, piezoelectric nanogenerator (PENG) and triboelectric nanogenerators (TENG) have been utilized as the most

promising energy harvesting device [11-14]. The piezoelectric mechanism works based on the material property of piezoelectricity (Figure 1.2(b)) [15]. Figure 1.2(b) illustrates the wurtzite structured ZnO crystal, where the layers of tetrahedrally bounded Zn^{2+} and O^{2-} are deposited along the c-axis. At the initial condition, both cations and anions are lined up at the center. When an external force is applied to the crystal, the structure is deformed, which results in the separation of positive and negative charge centers caused by the electric dipole. The alternative bending and releasing process generates the electrons and drives them through the external circuit. The triboelectric mechanism is a conjugation of triboelectrification and electrostatic induction as shown in Figure 1.2(c) [16]. Both devices are utilized in real-time MEMS systems due to their inherent properties, such as higher potential difference, biocompatibility, and better lifetime. As a result, significant research has been reported on different sensor and energy harvesting applications such as self-powered force sensors, monitoring systems, and energy from the vibrations of human organs, etc [1-5, 19-20].

1.2.1. Mechanism of piezoelectric nanogenerator (PENG):

In mechanical energy harvesters, the piezoelectric mechanism is the most widely used and well-studied approach for low-power electronic applications. It was discovered by the Curie brothers in 1880 upon quartz materials that generate current when applied the mechanical force, which is called the direct piezoelectric effect [17]. In 1881, the indirect piezoelectric effect was observed from fundamental thermodynamics theories by Gabriel Lippman [18]. Additionally, it was proved experimentally that a piezoelectric device or crystal will expand or contract in response to an electric field's amplitude.

Therefore, the ability of materials to create charge (or voltage) when triggered by mechanical stress is known as piezoelectricity as illustrated in Figure 1.3(a) [15]. It is owing to non-centrosymmetric in the crystal lattice, which induce the strain, thus generating a dipole. The piezoelectric effect can be explained using a molecular model in which the lattice is in equilibrium. The lattice disturbed the center of charges

when external force was deployed on the material, resulting in forming a small dipole. All tiny dipole combined together forms a net dipole in the material. This phenomenon of the materials is called piezoelectricity. Quartz, lead zirconate titanate (PZT), barium titanate (BaTiO3), aluminum nitride (AlN), zinc oxide (ZnO), and polyvinylidene fluoride (PVDF) [19,20] are some of the most common materials that show piezoelectricity.

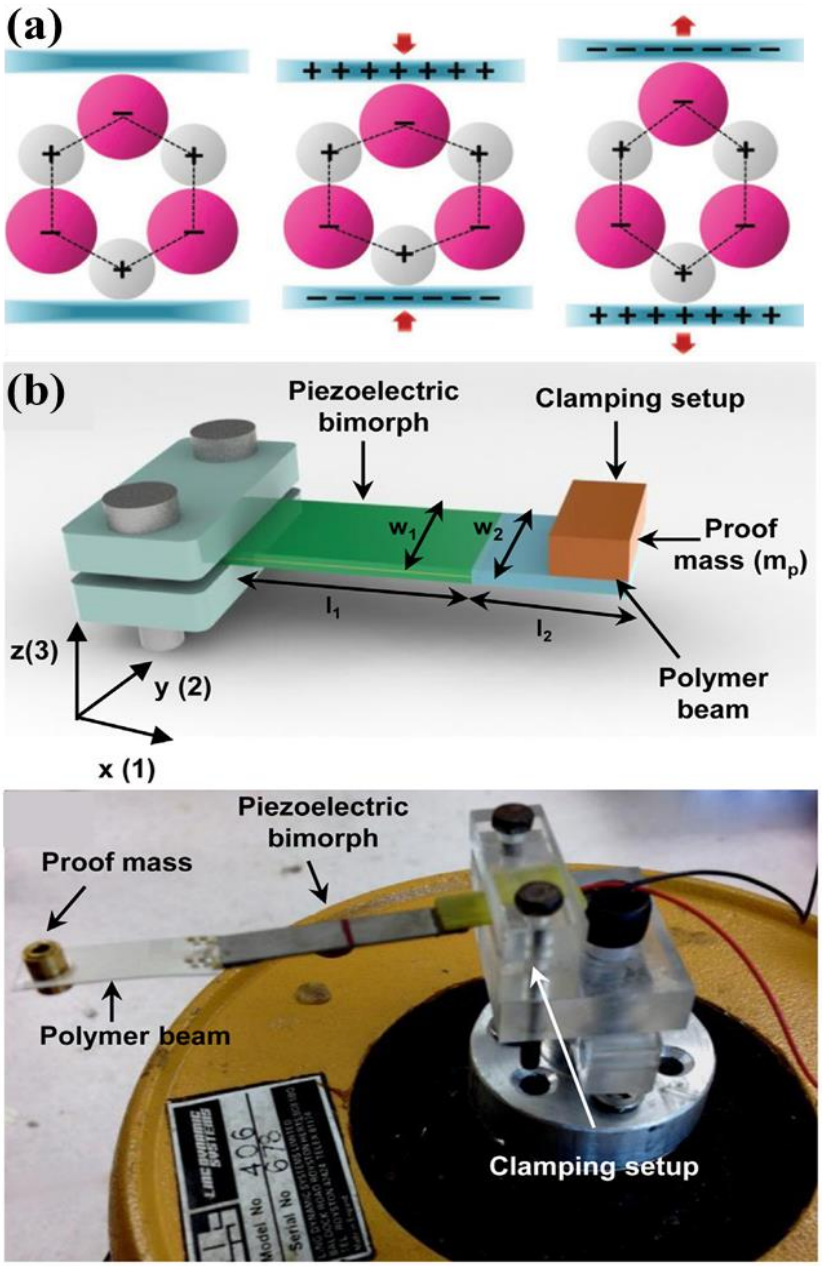

Figure 1.3(a) schematic of piezoelectric mechanism with the crystal lattice [15] (b) basic model of cantilever beam piezoelectric device [23].

1.2.2 History of PENG device:

Researchers have exploited the piezoelectric effect to capture mechanical energy and transfer it to electrical energy. The cantilever beam is the most frequent structure and design for piezoelectric energy harvesters (PEH) [21,22]. Figure 1.3 (b) depicts a standard PEH setup using a cantilever [23]. Once the excitation force reaches the inertial forces, the cantilever goes through a tension and compression phase around a neutral axis. As a result of the repeated stress, a cyclic voltage/current signal is generated between the current collecting electrodes of the piezoelectric layer. To enhance the stress levels in the piezoelectric layer, a proof mass (M) is usually placed at the tip of the cantilever beam. Thus, the voltage created at the electrodes has a larger magnitude. The other most widely used configuration of piezoelectric energy harvester is based on thick/thin film for flexible wearable applications. Paradiso et al. was the foremost researcher who demonstrated a shoe sole energy harvesting device in 1998 with PZT composite for wearable applications [24].

1.2.3 PENG applications:

The recent developments in the piezoelectric nanogenerators are discussed in the following section. After discovering the piezoelectric effect in quartz crystal in1880, the research community was fascinated to develop the higher-performance device. Early 20th century, Quartz and Rochelle salt-based device was used for high-frequency SONAR application [25]. The demand for piezoelectric crystals has significantly increased for navigation and communication purposes during the second world war. Consequently, barium titanate and the family of perovskite materials have been discovered, such as PZT, lithium niobates/tantalates, and PMN-Pt [26-30]. Due to the increasing demand for portable or wireless devices and systems with long life spans for many possible applications, recent breakthroughs in energy harvesting have accelerated. Piezoelectric energy harvesting (PEH) devices have been systematically constructed to harvest ambient energy and assist the sensor as a standalone module or in conjunction with the electronics to increase its lifespan. This section depicts some PEH, including human

gait movements, wearable and implantable devices, vibration energy harvesters, and self-powered sensors [31-34].

Human interaction-based energy harvesting PENG device:

The MIT Media Lab's Shenck and Paradiso have developed a novel energy harvesting device featuring a power circuit for harvesting energy from shoe soles [35]. When the user moves, the RF circuit sends a short range of 12-bit wireless recognition code (Figure 1.4(a)). Similarly, Figure (1.4 (b)) depicts a foldable large area pedometer device for self-powered human recognize walking and energy harvesting, which consists of a 2 V organic pedometer circuit and PVDF wrap for pulse and power generation [36]. The generated energy was used to power a pseudo-CMOS 14bit chip that served as a step counter and could track up to 16383 steps taken by a person. A PEH device was fabricated to quantify the human activity recognition from kinetic energy, illustrated in figure 1.4(c) [37]. The device determined human activity with 79% of power-saving without an accelerometer. Likewise, A wearable N95 respirator was embedded with a PVDF thin film for harvesting energy from human breathing, as shown in figure 1.4(d) [38].

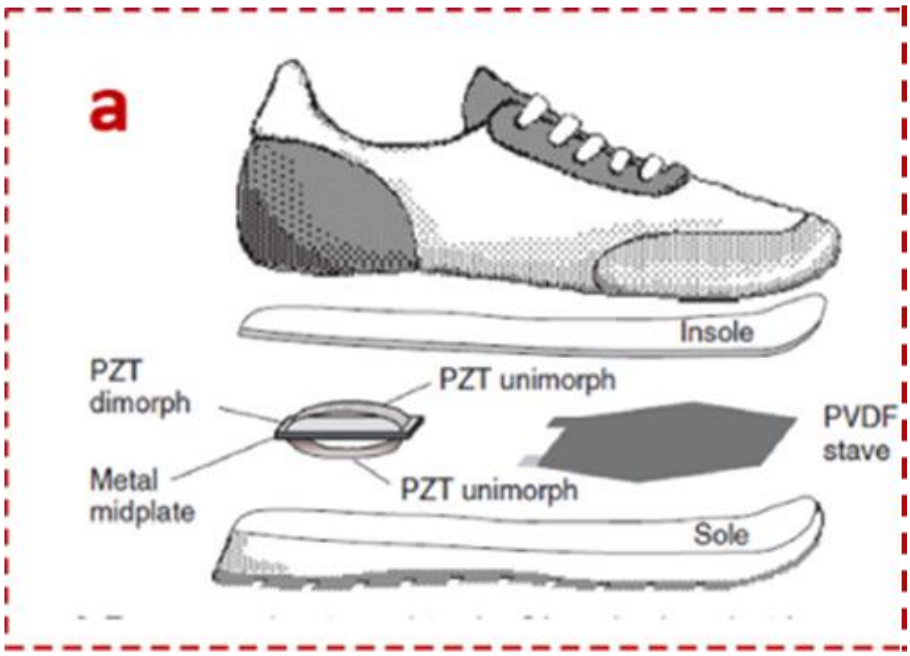

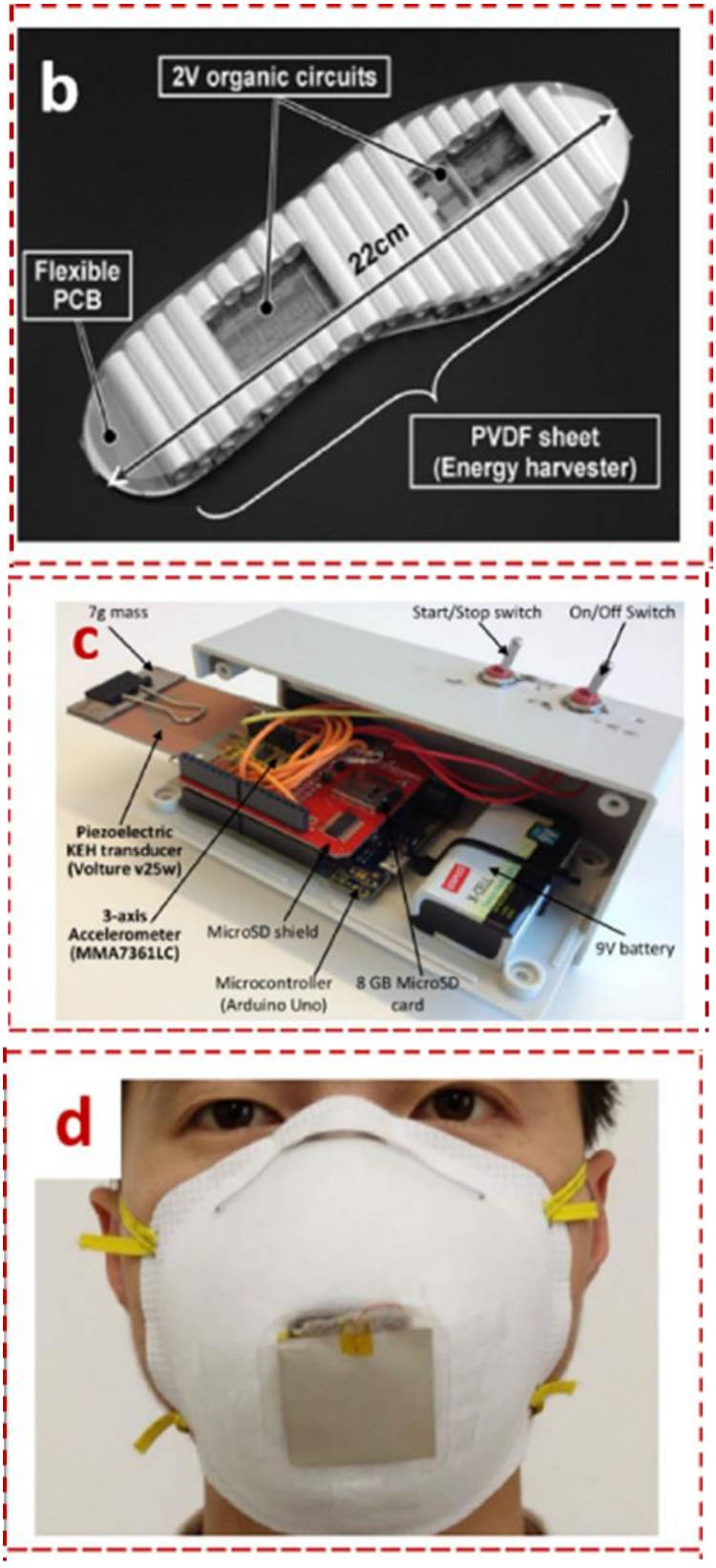

Figure 1.4 PENG energy harvesting device from various human motion (a) shoe sole [35], (b) shoe sole pedometer [36], (c) kinetic energy harvester for human activity recognition [37], and (d) energy harvesting from human breathing [38].

Implantable PENG device:

Figure 1.5(a) shows the micro spiral PEH device was fabricated for harvesting energy from the cardiac environment [39]. It is a potential device to provide long-lasting and compact biomedical implantable devices such as pacemakers without leads. This device attained three $\mu J/cm^3$ during the experimental testing. Similarly, a lead-based PEH was implanted into the animal for self-powered sensing and power generation application using biomechanical resources, as shown in figure 1.5 (b-d) [40-42].

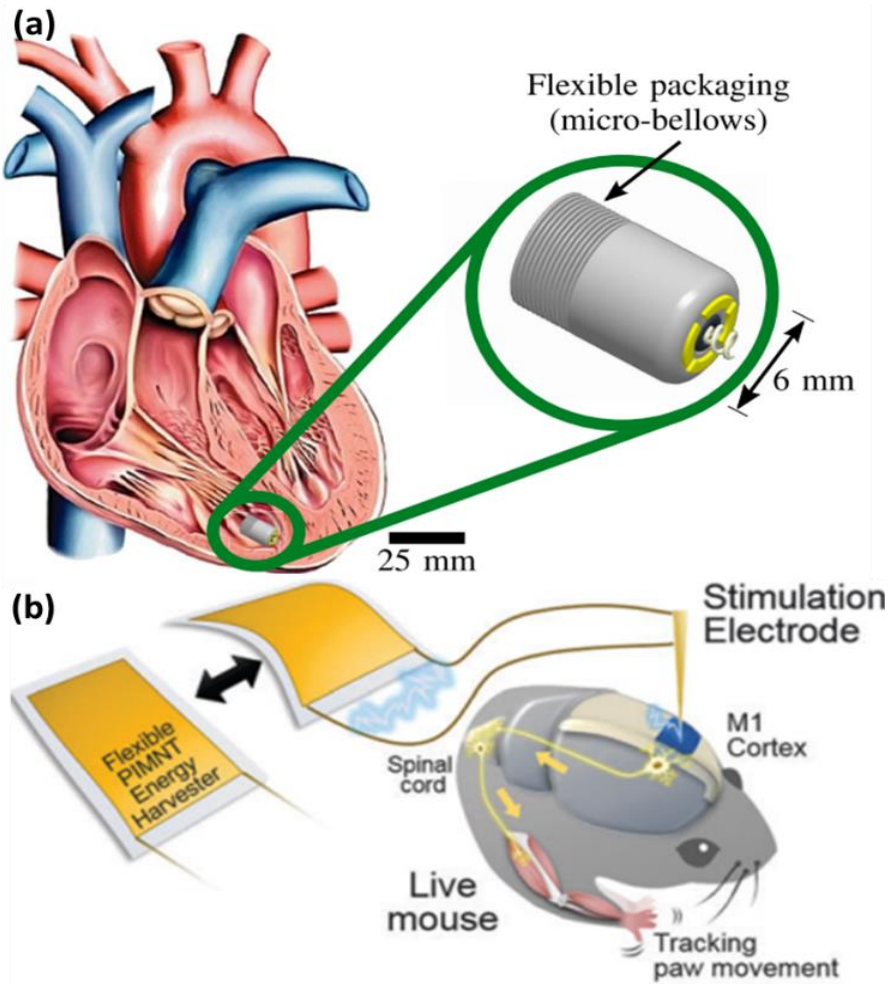

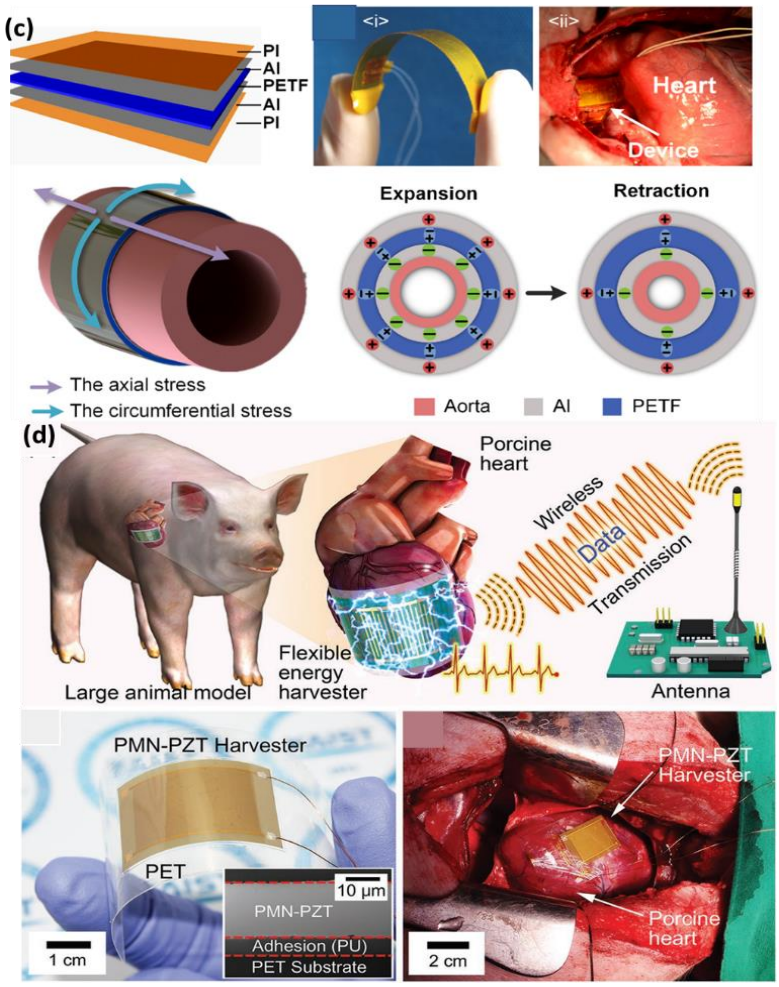

Figure 1.5 depicts the PEH device development in various biomedical applications [39-42].

The majority of the existed research works have developed the PENG device with lead-based materials because it generates higher output performance and wider applications. However, it has significant drawbacks, such as less biodegradability and rigid substrates. Though there are several biocompatible piezoelectric materials, flexible substrates are exhibited, but it yields lower power density. Therefore, choosing biocompatible materials with a higher piezoelectric coefficient is a challenging part of the development of PENG. An appropriate and alternative approach is required to overcome these drawbacks.

Hence, the triboelectric nanogenerator will be one of the predominant alternatives for mechanical energy harvesting and self-powered sensor applications. The following section discusses the triboelectric nanogenerator mechanism and its applications.

1.3 Mechanism of Triboelectric nanogenerator (TENG):

The triboelectric nanogenerator works fundamentally by integrating two ideas, such as triboelectrification (also known as contact electrification) and electrostatic induction. Contact electrification is a phenomenon that charges the surface when two different surface polarity material contacts each other. Electrostatic induction is the redistribution of electric charge in the material. Several concepts have been proposed to describe the phenomenon of contact electrification [43]. However, the theory of electron transfer in various materials is defined by a well-established model of the work function concept [44]. Based on this concept, when two metal surfaces contact each other, the tunnelling effect causes the electron transfer to persist in the thermodynamic equilibrium. The electric potential that can measure between metals caused by charge transfer is expressed in the following Eqn. (1.1).

$$V_{1/2} = \frac{\emptyset_1 - \emptyset_2}{e} \quad \text{..... (1.1)}$$

$V_{1/2}$ is a potential difference between two metals, $\emptyset_1$ and $\emptyset_2$ are work function of metal 1 and metal 2, and e is the elementary charge. The same work function theory can describe the charge transfer in the metal-insulator and insulator-insulator models [45,46]. Figure 1.6 Fig. 1 graphically depicts two metals with different work functions, $\emptyset_1$ and $\emptyset_2$, in contact [43].

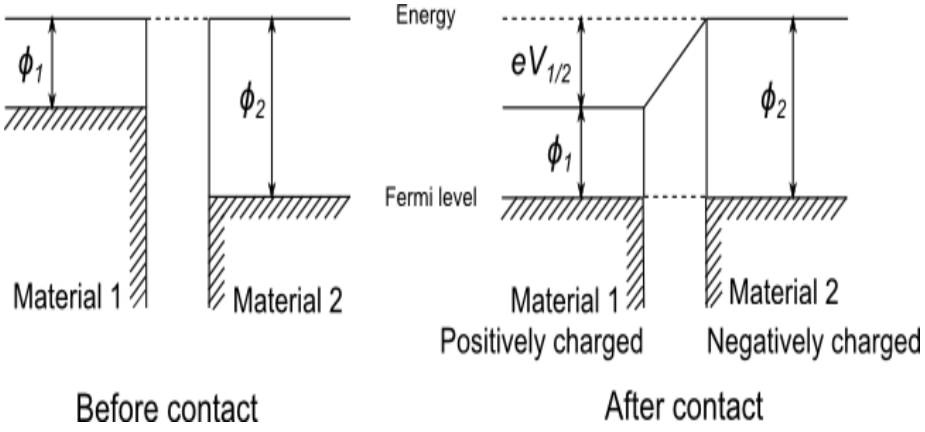

Figure 1.6 Charge transfer model for metal-metal contact [43]

Due to the material property and chemical structure, the materials can lose or gain electrons in various materials. Thus, when two triboelectric layers come into contact and then separate, the contact electrification

process causes both layers to become electrically charged. Several metals and dielectric materials have been arranged based on the surface charge density, as shown in figure 1.7 [47,48]. In comparison to the elements on the negative side of the series, the positive side materials tend to give electrons. This indicates that positive elements tend to become positively charged and vice versa. It is possible to anticipate and select the polarity of the charges generated when two materials come into contact with one another using the relative locations of the materials in a triboelectric series. When designing TENGs, this guideline is vital for material selection.

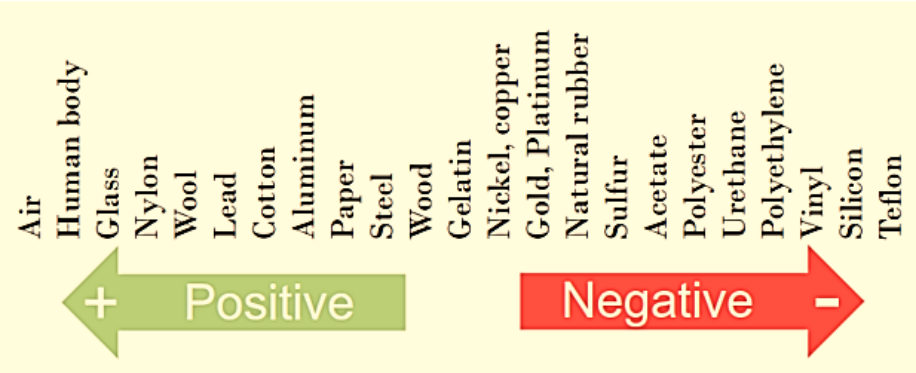

Figure 1.7 Triboelectric material series arranged based on the electron surface charge [47, 48].

The triboelectric mechanism can be further distinguished into two categories based on the mechanical operating condition, such as (i) out-of-plane contact-separation mechanism and (ii) in-plane sliding mechanism. These two mechanisms are broadly described in the following section.

1.3.1 Out of plane contact separation:

In this process, the triboelectric layers are pushed to the plane of contact by the relative motion, leading to contact and separation. The primary stage of the TENG is contact electrification, in which both tribo layers are equally charged positively and negatively. Further, the charged surface leads to electrostatic induction on the metal electrode in the TENG device as shown in Figure 1.8. Primarily, both layers are kept at a distance of x (1). When the external force is applied to the TENG device, the two different dielectric materials come into contact to form

chemical bonds (2). The formation of chemical bonds helps to migrate the charge between two surfaces to equalize the electrochemical potential. Then the electron will flow from the top electrode to the dielectric surface to fill surface states with negligible decay. The electric field builds up during the separation or increasing distance (x) between each triboelectric surface and induces the potential difference (V). This potential difference drives the electron from top to bottom electrode that, results in a negative current with the external circuit (3). Once the device reaches the initial position (1,4), the surface charge distribution reverts to the equilibrium state. Subsequently, the device surfaces close to each other induce the reverse electrostatic field to bring back the electron from the bottom to the top electrode and attain the positive current (5). This concept is close to the parallel plate capacitor and can be considered for developing a theoretical model of TENG.

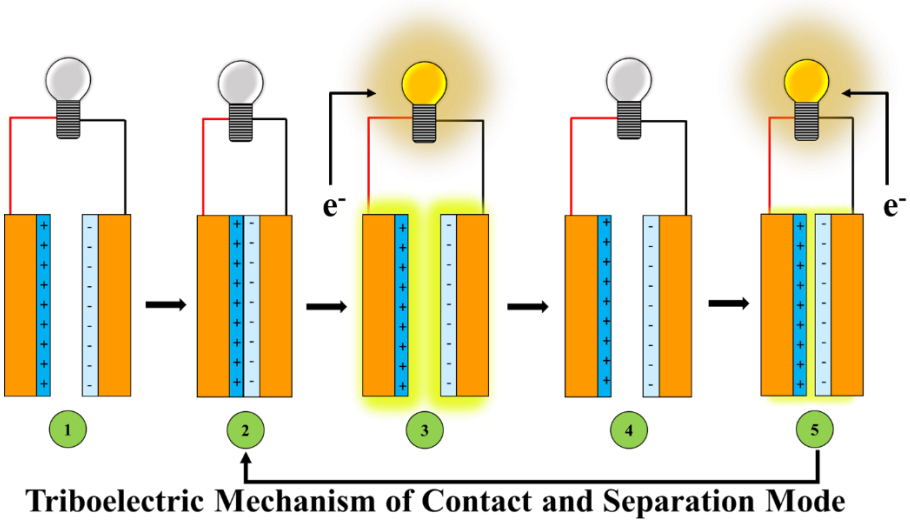

Figure 1.8 illustrates the out-of-place contact separation triboelectric mechanism [49]

Out-of-plane TENG Application:

TENG is not only an energy harvester, and it can be used as a self-powered sensors and energy storage device, it is due to its diversified device operational mode. An enormous need for small standalone power units with huge capacities and high durability is being expressed by the significant increase in wearable electronics. As illustrated in Figure

1.9(a), integrating TENG and storage devices offers a possible way to realize the objective of a sustainable power unit [50]. A carbon fiber-made TENG device combined flexible MXene supercapacitor was developed for energy harvesting and simultaneously storing the electricity. On the other hand, TENG can also function as a self-powered sensor. Figure 1.9(b) illustrates the eye motion sensor by the TENG mechanism [51]. This device can measure the micro-motion of human activities and shows the potential application in human-machine interfaces.

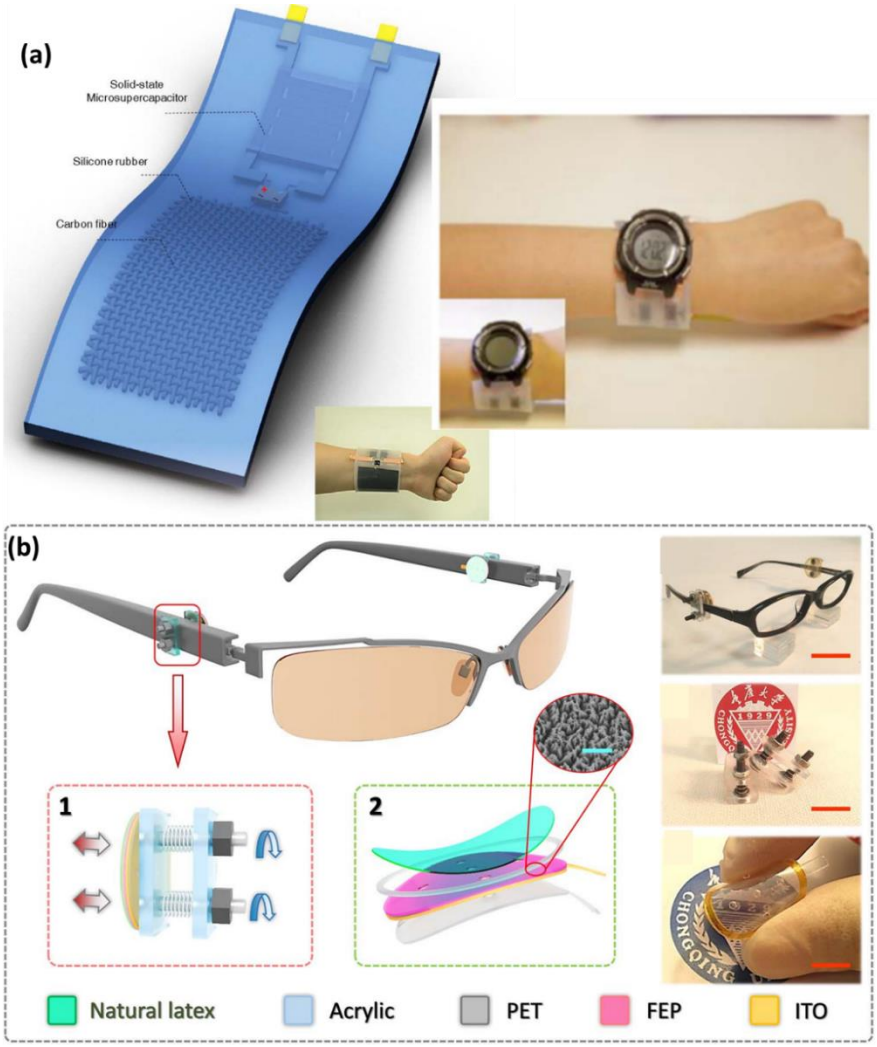

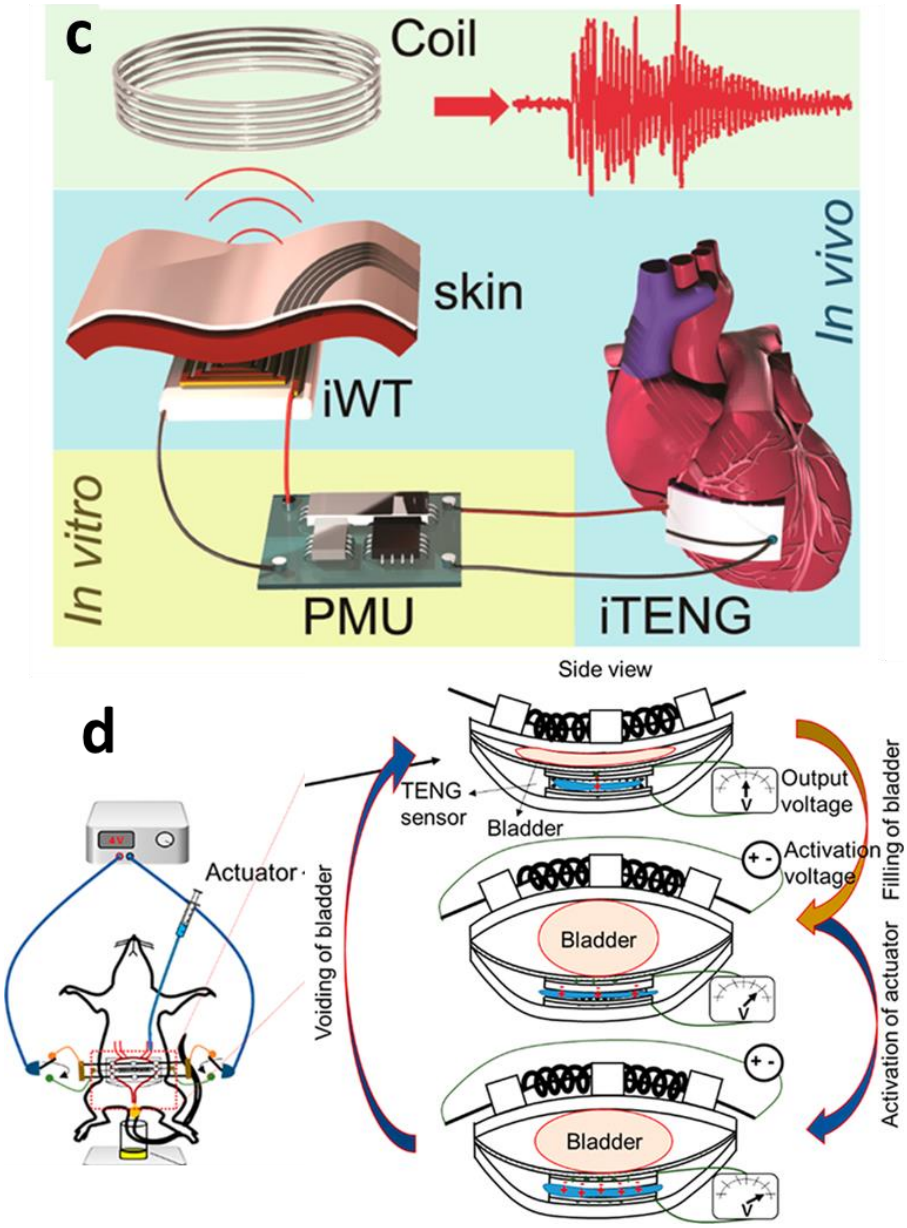

Figure 1.9 depicts various contact separation applications (a) MXene supercapacitor [50], (b) eye motion sensor [51], (c) cardiac monitoring [52], and (d) UAB syndrome monitor [53].

Health condition monitoring and drug delivery have played a vital role in the contemporary wearable and implantable electronic devices to empower the quality of everyday life. Figure 1.9 (c) depicts the TENG-based cardiac monitoring system implanted in adult swine [52]. It was implanted in in-vivo and monitored the heartbeat for 72 hrs continuously. Likewise, in figure 1.9 (d), the TENG-based drug delivery system and underactive bladder (UAB) syndrome monitoring are

demonstrated [53]. The drug delivery system was developed with an intelligent actuator and self-powered sensor. In the case of the UAB system, the self-control TENG pressure sensor was made for rat bladder monitoring.

1.3.2 In-plane sliding:

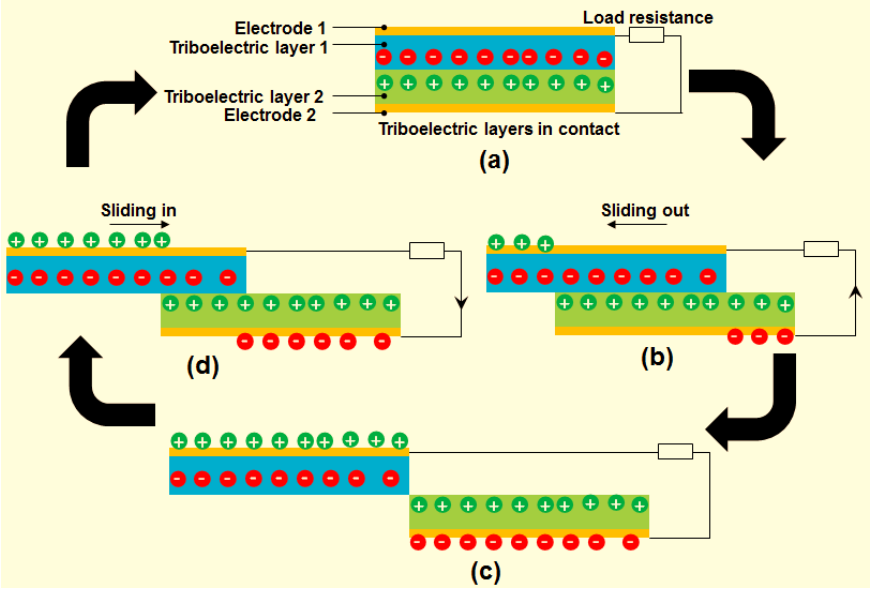

Figure 1.10 represent the in-plane sliding TENG mechanism [54]

In this mechanism, both triboelectric layers are entirely in contact condition at the initial step. The contact area decreases when the triboelectric layers move forward or backward. During this process, the equilibrium state gets disturbed and creates an imbalance in the surface charge equilibrium. The electrostatic induction stimulates charge in the back electrodes to maintain the surface charges with equilibrium. Figure 1.10 depicts the fundamental steps in the in-plane TENG mechanism.

In-plane sliding TENG application:

A self-powered electrospinning system has been developed with TENG rotational disk energy harvester (Figure 1.11(a)) [55]. This system generated an AC voltage of 1400 V and rectified with double rectification to increase the output. In addition, the rotating disk-based TENG device has been demonstrated in a molecular mass spectrometer to attain the control of ionization charges, as shown in Figure 1.11 (b) [56].

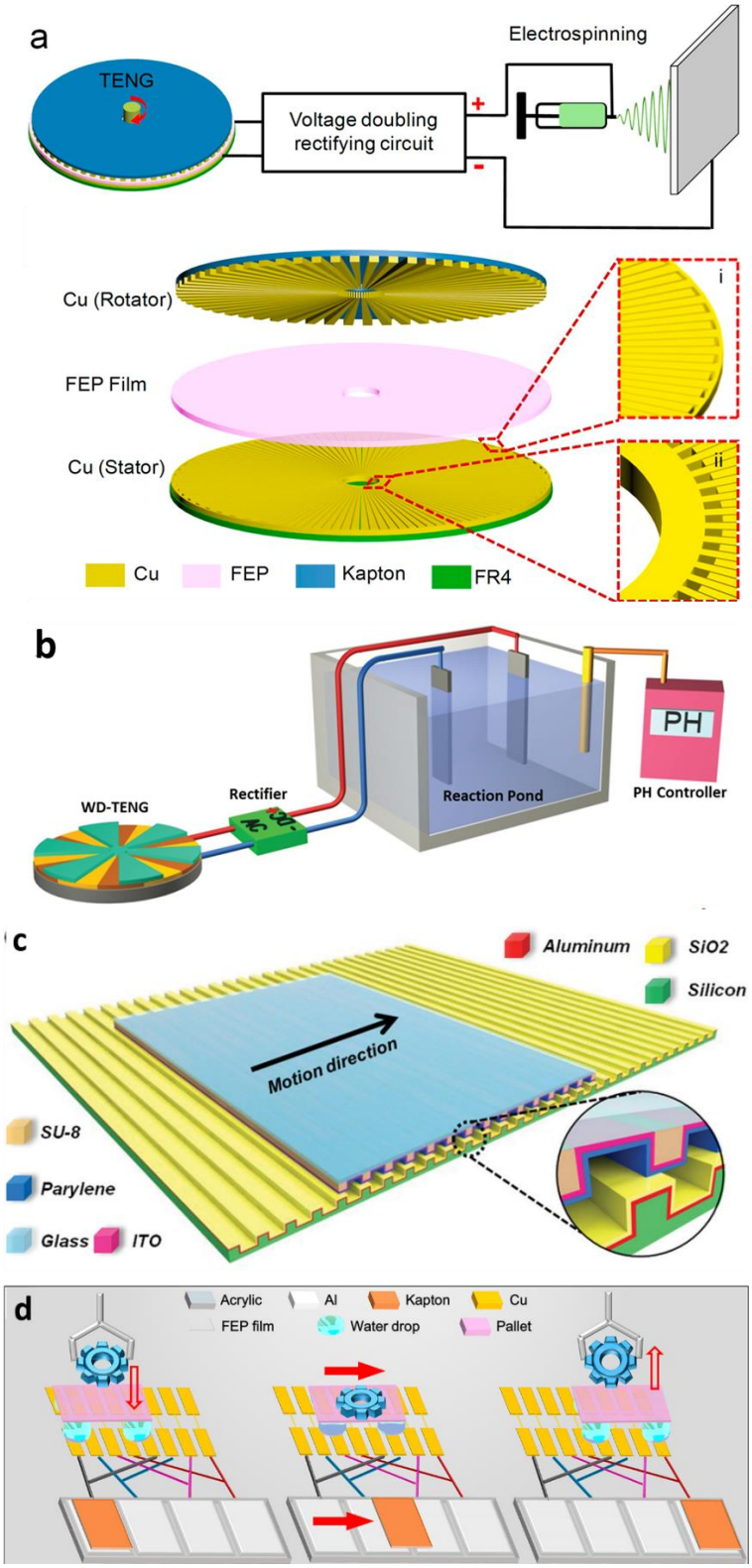

Figure 1.11 sliding mode TENG integrates with various functional intelligent micro/nano systems (a) self-powered electrospinning [55], (b) charge ionizer [56], (c) TENG motion sensor [57], (d) microfluidic droplet manipulator [58].

A High-resolution speed sensor with sliding mode TENG was developed with a line grating structure and shown in Figure 1.11 (c) [57]. The displacement and the movement speed may be obtained from the output waveform owing to this specific geometry grating arrangement. Similarly, Figure 1.11(d) illustrates a free-standing mode TENG-developed self-powered microfluidic droplet manipulator. [58] When the Kapton tribo layer is traced on the electrode, the as-developed mini-vehicle carries the drug and transports it from one side to the other.

Most of the materials are being utilized for TENG device manufacture and real-time application demonstration. Also, most of the devices consist of non-biocompatible or not eco-friendly materials been integrated. Though some eco-friendly devices have been demonstrated, it shows lower power density compared to others. However, there is a further study that needs to be done in order to improve the existing TENG performance. Surface functionalization is an appropriate method and can improve the performance of environmentally friendly materials.

1.4 Motivation:

Despite having several merits of PENG and TENG devices, the device implementation towards sustainability and higher output performance still in its infant stage. In the case of PENG devices, a wide variety of materials such as PZT, ZnO, ZnS, $BaTiO_3$, PVDF, AlN, GaN, and so on has been demonstrated. Among them, ZnO-based piezoelectric materials have gained tremendous interest due to their unique features such as non-centrosymmetric structure, low fabrication cost, and eco-friendliness. Based on the literature, doping is identified as one of the effective approaches to enhance the PENG device performance. Hence, to improve the performance of pristine ZnO-based devices, doping with III-IV group elements (B, Al, Ga, In, Pb, Sn) has been employed due to similar ionic radii with Zn^{2+}. Besides, most ZnO-based PENG devices have been developed on a rigid substrate such as ITO, GaN, sapphire glass, silicon, metal sheets, and plastic fibers. But it has been observed that these substrates are rigid, not even biodegradable, through which the mechanical energy is difficult to harvest from an intricate position

of the substrate. Moreover, such substrates increase environmental pollution and reduce the profit in the consumer trades. Therefore, green and recyclable substrates could be an appropriate alternative for fabricating electronic devices.

In the context of TENG, the materials are arranged based on the surface charge density value. The PET layer is often employed as a positive charge material in the flexible TENG device fabrication. The lower electron affinity material can quickly transfer the charge from the higher affinity material by contact triboelectrification. The reason for preferring the PET-based material is recyclable, abundantly used in day-to-day life, very low electron affinity, a wide range of options, and flexibility. Similarly, to enhance the output performance of the TENG, many factors have to be considered, such as surface contact area, mechanical force, contact speed, material work function, and relative humidity. Many reports are available related to material work function and various device architectures. Recently, the researchers are concentrated to modulate the surface charge density and increasing the output performance of the materials by chemical and physical modification. Several methods have been involved in the chemical modification process, such as ion injecting, fluorinated surface, and molecular targeting functionalization. However, limited methods evolved effectively in the physical modification, such as laser surface modification, lithography, molding, and imprinting to enhance the surface contact area of the device. Laser surface patterning (LSP) can be employed to develop various macro, micro, and nano features with high spatial resolution. It has potential advantages such as less processing time and no requirement of masks or toxic chemicals to develop the structures. Likewise, LSP is a simple method that changes the chemical and surface properties of the material.

In this work, initially, we have developed the eco-friendly tin-doped ZnO PENG device. We also investigated the device's physical properties and piezoelectric performance and studied its practicability. Subsequently, the commercial PET material performance has been enhanced with laser 3D pattern and interfacial layer effect. The as-

fabricated TENG device was demonstrated under various mechanical parameters to investigate its energy harvesting ability.

1.5 Objectives:

In this work, we have focused on developing sustainable energy harvesting devices to supplement the battery and improve the viability of electronic devices. For both PENG and TENG, device performance has been improved by doping and laser surface patterning with an interfacial layer effect. In this context, the objectives can be realized by the following categories,

(1) Development of eco-friendly piezoelectric nanogenerator

(2) Development of 3D patterned triboelectric nanogenerator

(3) Enhancement of patterned triboelectric nanogenerator performance.

These categories are further detailed in the following chapters

1.6 Overview of the thesis:

Chapter 1: Introduction:

A brief introduction about energy harvesting and categories. The fundamental and significance of mechanical energy harvesting and its process in light of current advancements are elaborated.

Chapter 2: Overview of the energy harvesting technologies:

Describes the detailed literature survey on piezoelectric materials and its applications. Similarly, various surface modification methods involved in triboelectric performance enhancement.

Chapter 3: Development of Sn doped ZnO-based eco-friendly piezoelectric nanogenerator for energy harvesting applications.

Present Eco-friendly piezoelectric device fabrication and its performance improvement by Sn doping. The device was demonstrated to harvest non-uniform mechanical load condition like musical drums.

Chapter 4: Enhancement of Triboelectric Nanogenerator Output Performance by Laser 3D-Surface Pattern Method for Energy Harvesting Application.

We have introduced an alternative method for triboelectric output enhancement by continuous laser surface modification method. The eco-friendly material was chosen and improved its surface characteristics which increased the TENG performance. The laser power and mechanical parameter were optimized and demonstrated for energy harvesting applications.

Chapter 5: Enhancement of line patterned triboelectric output performance by an interfacial polymer layer for energy harvesting application.

Introduced the interfacial layer for enhancing the line patterned triboelectric nanogenerator output performance. The interfacial layer mechanism has been described and theoretically verified by COMSOL simulation.

Chapter 6: Conclusion and the scope for future work.

Key out comes of the work consolidated and the future scope of this works are coined.

Chapter 2
Literature survey

2.1 History of the piezoelectric materials, devices, and development:

The piezoelectric effect was discovered by the Curie brothers in 1880; since then, there have been tremendous enhancements in the development of piezo devices and found a lot of natural and synthetic piezoelectric materials. The road map of the piezoelectric invention is shown in figure 2.1 [59]. Each stage of piezoelectric development brought new perceptions and research problems with a solution that helps establish to novel applications. Further, the piezo material is classified into six categories such as III-V & II-IV semiconductors, synthesized crystals, naturally occurred crystals, polymers, perovskite, and micro/nanocomposites.

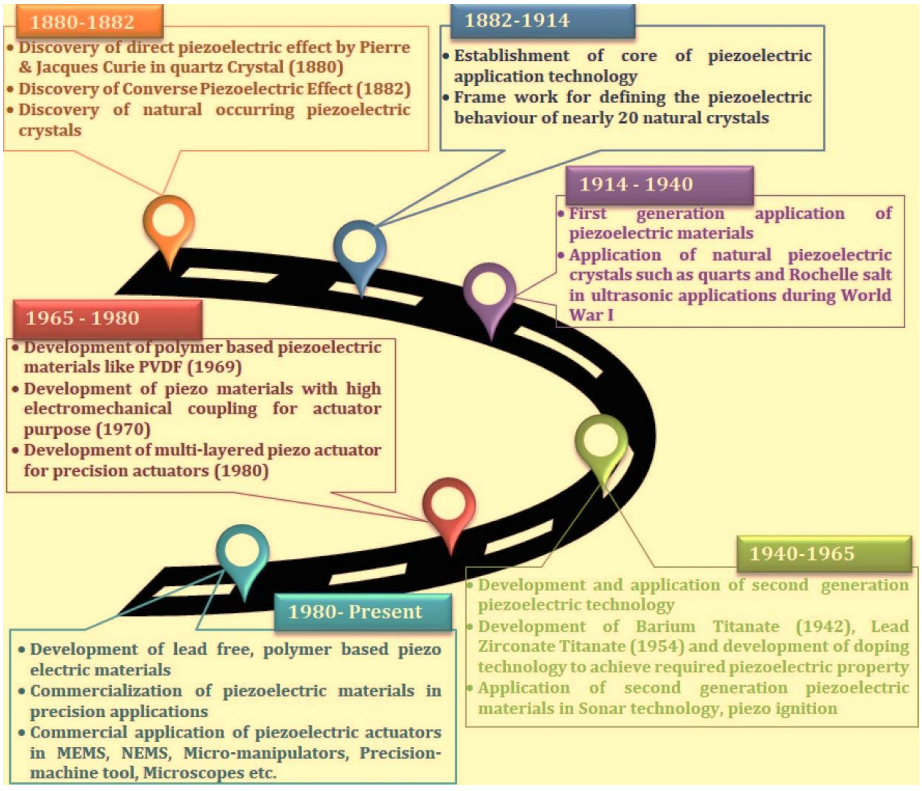

Figure 2.1 road map of the piezoelectric developments [59]

2.2 Classification:

The piezoelectric materials have remarkable anisotropy properties when the elastic and electric fields are linked to each other. The external stress or mechanical load shifts the position of the atom/molecule to form net

dipole moments, which leads to polarization and electric field. Therefore, the materials category are briefly discussed in the following section.

2.2.1 Natural crystal:

Many naturally occurring crystals possess the non-centrosymmetric feature, including Berlinite, Sucrose, Rochelle salt, Macedonite, Tourmaline, and Quartz. Nevertheless, all of those materials perform poorly due to the piezoelectric coefficient except Quartz and Macedonite [60].

2.2.2 Synthesized crystal:

Numerous researchers have attempted to create highly efficient crystals in an effort to replicate nature. Some piezoelectric crystals developed in the laboratory are langasite, gallium orthophosphate, lithium-niobate, and lithium tantalate [25]. Since the motivation of the work concern the synthesized crystal is not eco-friendly.

2.2.3 Perovskites:

A typical formula of ABO_3 is derived for piezo perovskite ceramics, where A and B are metal cations and O is an anion. In the past decades, this category has produced the most well-known piezoelectric materials. In particular, the PZT or lead-based Perovskite materials have a high piezoelectric coefficient and electromechanical coupling coefficient. However, those materials are subjected to RoHS guidelines by European Union due to their toxicity, pollute the environment and un eco-friendly fabrication techniques [25]. To overcome this issue, the researchers developed alternative perovskite ceramics such as Barium Titanate and Potassium Niobate. Hence, the EU recommends that these ceramics be an appropriate choice to substitute lead-based ceramics with analogous functional properties [60-62].

2.2.4 Polymers:

Limited synthetic polymers are listed in the piezoelectric materials such as polyvinylidene fluoride (PVDF), trifluoroethylene, chlorofluoroethylene, and their copolymers PVDF:TrFE and polypropylene. This family group of polymers is more flexible and has high durability at higher applied forces, though they have a low

piezoelectric coefficient [25]. Additionally, they considered poly-dimethyl siloxane to be a crucial component of composite piezoelectric materials in addition to flexibility (PDMS).

2.2.5 Composites:

Piezoelectric composites fall under a distinct class of materials due to exceptional flexibility and adaptability. In addition, it has strong coupling coefficients, minimal acoustic impedance, acceptable biocompatibility, great mechanical flexibility, and broad bandwidth in conjunction with a low mechanical characteristic. The first piezoceramic-polymer composite was reported in the year of 1972 by T Kitayama, where PZT powder blended with PVDF and constructed the device with piezoelectric and pyroelectric properties. The composite shows enhanced performance compared to pristine PVDF.

2.2.6 III-V and II-IV semiconductors:

III-V and II-IV semiconductors group materials can generate the piezo potential owing to the non-centrosymmetric structure and polarization of ions when the external force is applied. Generally, all the piezoelectric semiconductors have the Wurtzite structure, which is one of the main properties of piezoelectricity. i.e., Gallium Nitride, Indium Nitride, Aluminium Nitride, and Zinc Oxide (ZnO) [62]. Since 2006, the substantial research report has increased on ZnO piezoelectric devices due to its inherent material characteristics like biocompatibility, vast materials structures, and piezoelectric coefficient. Detailed information about ZnO and its recent trends in PEH is discussed in the next section.

2.2 An overview of the ZnO:

The extensive usage of semiconductors in electronics devices and sensors and improved production methods, the research trend in semiconductor materials has grown in this century.

Particularly, ZnO is an intrinsic semiconductor with distinct physical, chemical, and structural properties, which gives considerable attention to the scientific community [63]. ZnO falls under the II-VI semiconductor material family with a broad band of 3.3 eV and large exciton binding energy of 60 meV. ZnO has unique features such as a non-centrosymmetric structure with a wurtzite structure, high modulus

of elasticity, and high piezoelectric tensor [65]. In addition, it can incorporate other semiconductor materials without losing their parent property, large-scale manufacturing ability, low cost, and high bio-compatibility [64]. Moreover, it has comprehensive application options such as UV sensors, gas sensors, glucose sensors, and energy harvesting devices like drug delivery systems, glowing lower power LEDs, etc [62].

Since device structure is crucial to piezoelectricity, ZnO has various nanostructures options, including nanoplates, nanowalls, nanotubes, nanoflowers, and nanowires. However, due to crystal structure with asymmetric charges, nanorods exhibit substantial reports are available in the PENG device and sensors. Therefore, the information on the impact of variously oriented ZnO nanowires on the creation of PENG devices is provided in the next section.

2.2.1 Lateral Nanowires:

Various micro/nano device has been developed with an array of ZnO nanowires or a single nanowire for numerous applications (Figure 2.2). A single ZnO nanowire flexible device was fabricated with a silver paste electrode, shown in Figure 2.2 (a) [66]. When the device bend or twists, the uniaxial tensile strain causes the piezoelectric potential along the ZnO nanowire, which drives the electron to the external circuit. A pulse signal has generated continuously while the device is bending and releasing process. The device delivers an open circuit electric potential of 20-50 mV and a short circuit current of 400-750 pA, which is very low and hinders its application (Figure 2.2 (b)) [67]. Hence, several lateral ZnO nanowires were directly integrated into a single device in order to enhance the output of ZnO-based PENG. Almost 700 nanowire rows were developed on a flexible substrate, and each row contained around 20,000 nanowires which showed high flexibility of the device (Figure 2.2(c)) [68]. When a linear motor stretches the device with the strain of 2.13%, it generates an average of 1.2 V and 26 nA. As a result of the various straining rates in the releasing and stretching operations, the PENG output peaks' significantly varying magnitudes are detected.

Nevertheless, the generated output is insufficient to power the electronic devices. The performance can be enriched by increasing the intensity of the nanowires. Zhu et al. developed a high-output PENG device with lateral nanowires (NWs) by a sweeping printing method shown in Figure 2.2(d) [69].

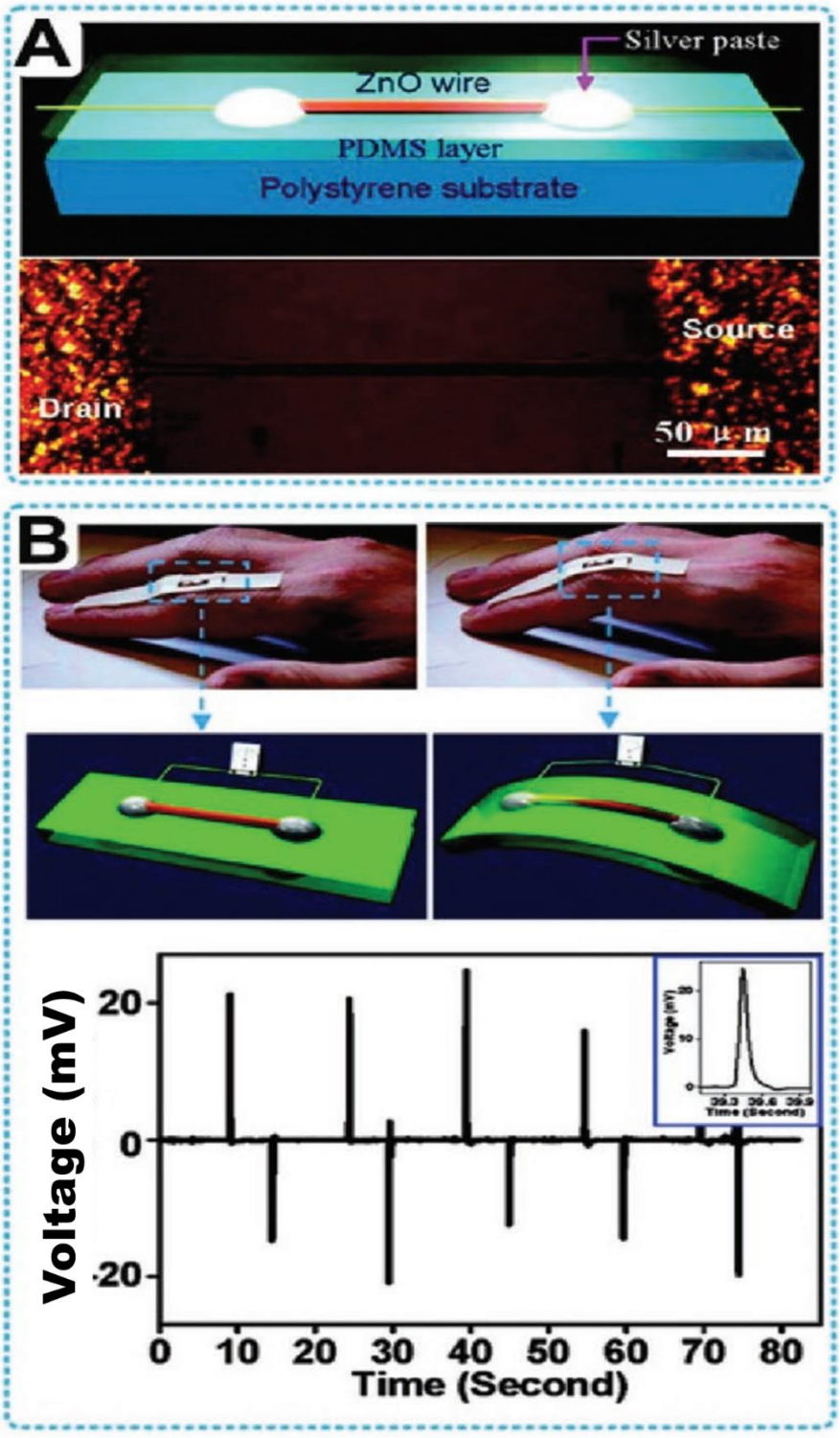

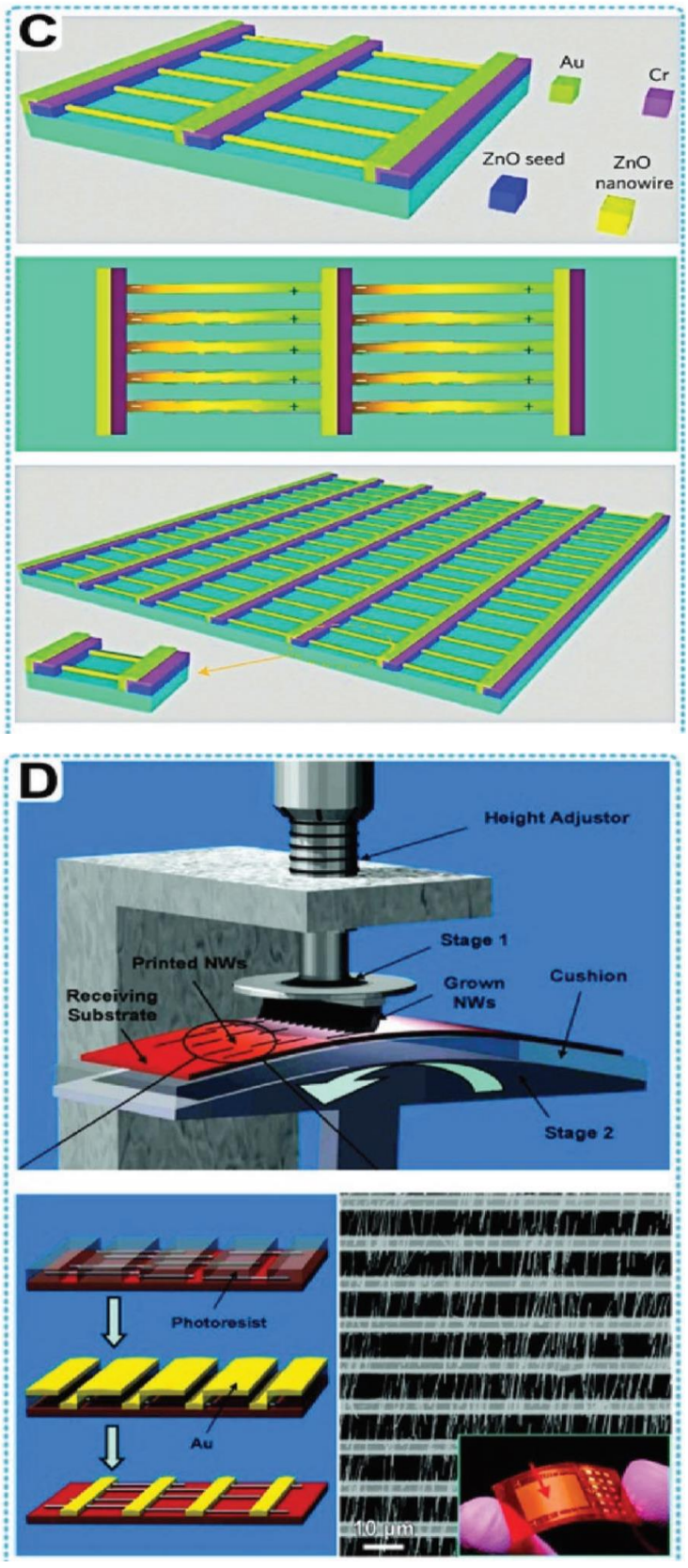

Figure 2.2 ZnO-based lateral nanowires (a&b) single nanowire PENG device [66,67], (c) flexible nanowire array [68], (d) sweeping printed flexible nanowire PENG device [69].

For the sweeping printing method, initially, the vertical ZnO nanowires were fabricated on silicon substrate by physical vapor deposition. Later, it was transferred on the Kapton substrate by sweeping shear force, and the average density was $1.1*10^6$ cm^2. Around 600 rows of Au electrodes were deposited with a gap of 10 µm by photolithography for the ZnO NWs device. PDMS was finally employed to pack the complete device in order to further insulate the device from an intrusive environment of humidity and corrosive chemicals and to increase mechanical durability. This device attained up to 2.03 V and 11 mW/cm^2 of power density which was used for powering the commercial LEDs [70]. Similarly, the conical coated ZnO NWs were developed and generated macroscopic electric potential. The generated power was adequate to power the LCD. However, these methods are limited to industrialization due to their complex process and expensive. To overcome this problem, the researcher has made a substantial effort to introduce an alternative approach with a simple and cost-effective process.

2.2.2 Vertical nanowires:

The vertically grown ZnO nanowire arrays with stable polar orientation can be used to harvest the mechanical energy and convert it into electrical potential. The solution-based wet-chemical process is one of the most reliable methods for developing vertical ZnO nanowires (Figure 2.3(a)) [71]. It can be also used to fabricate structures even at low temperature of 80˚C on different substrates. The pre-sputtering seed layer can effectively control the nanowire's uniformity and alignment. This method offers a high volume, low cost, and precise manufacturing of PENGs. In this context, a significant number of flexible PENGs were created, facilitating the development of portable electronics that can run independently. Choi et al. developed a completely flexible vertically aligned ZnO NWs in 2010 for PENG application [72]. The mechanism of this particular nanostructure is also similar to the lateral ZnO NWs. At the ZnO nanowires and metal electrode interface, the piezoelectric potential-induced electron flow was regulated by the Schottky barrier. However, these device electrodes can cause problems with mechanical durability when building a flexible device, which reduces endurance and

consistency. Therefore, the Carbon nanotube conductive electrode was used and increased the stability and flexibility compared to others (Figure 2.3(b)). Hu et al. fabricated PMMA coated ZnO nanowire array PENG device in 2011 shown in Figure 2.3(c) [68]. The maximum output of 20 V and 8 µA were generated. Electron flows were induced in the external load caused by a repeated mechanical deformation given to the device by combining the electrostatic induction with the piezoelectric effect. Lee et al. fabricated a highly flexible PENG device with Al foil (18 µm) which performed as a substrate and electrode [73]. The device was used to harvest small movements from the human face and generated an output voltage of 200 mV and a current of 2 nA. It has an excellent ability to work with the biomechanical sensor.

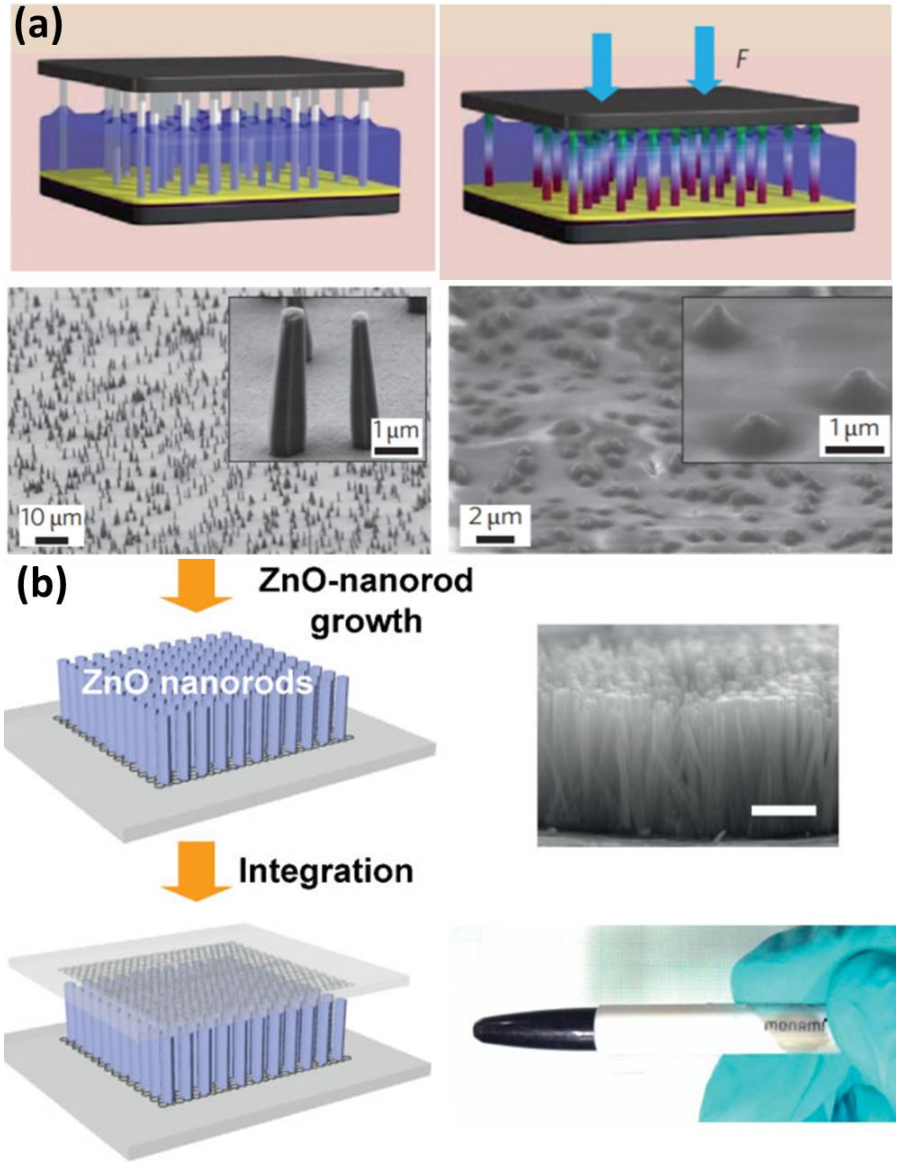

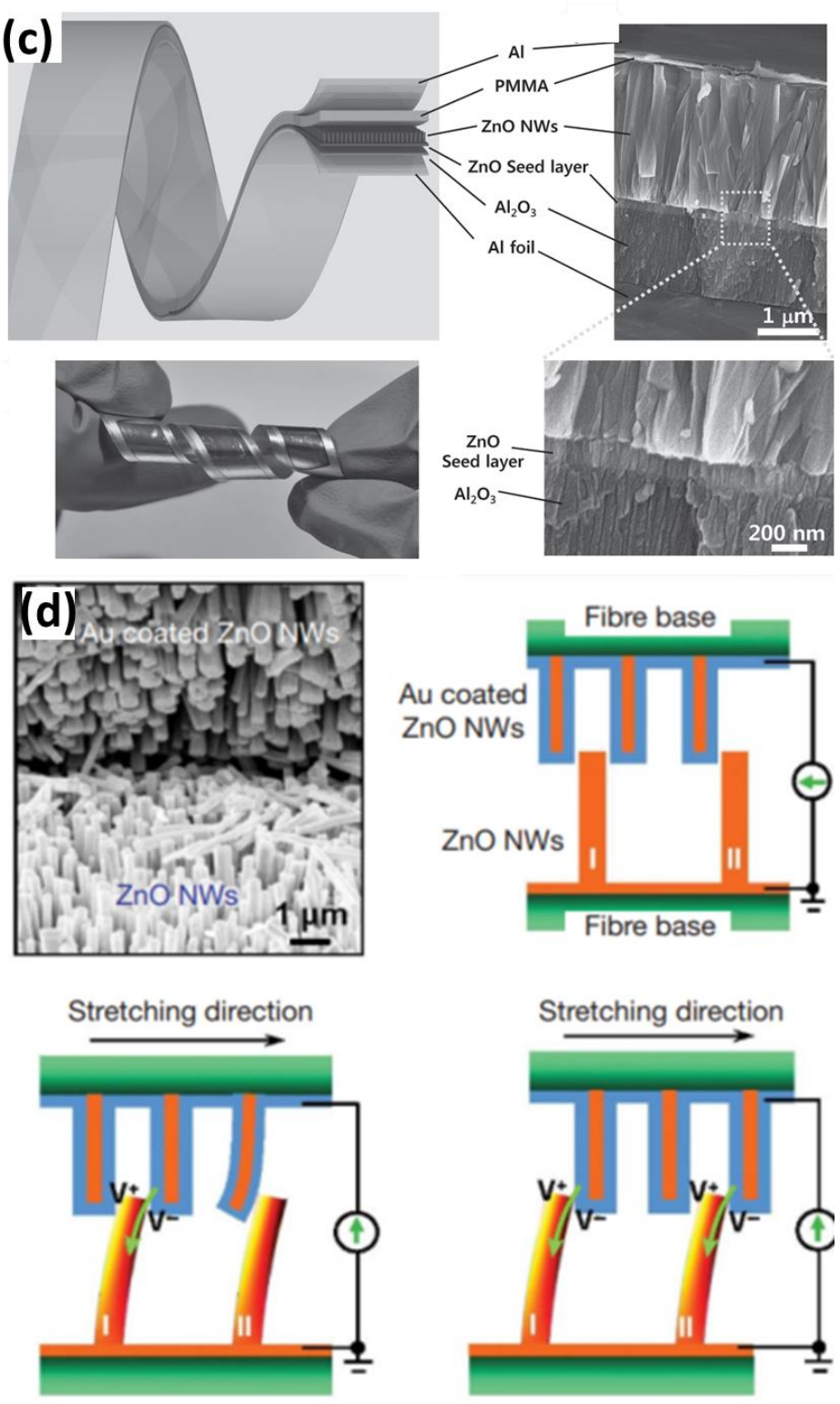

Figure 2.3 various vertical ZnO nanowires (a)hydrothermal grown NWs (b) NWs on graphene substrate (c) super flexible NWs on aluminium substrate (d) vertically grown NWs on textile fibre

Figure 2.3(d) illustrates the ZnO NWs coated fiber PENG device for harvesting low-frequency vibration. The mechanical energy was converted into electrical potential when the nanowires stroked on the entangled fibers. Lee et al. also developed PVDF coated ZnO nanowires for low-frequency mechanical forces. The device has harvested the energy from human elbow movements and generates 0.1 V and 16 μW cm^{-3}. Similarly, Lee et al. and Li et al. developed fiber-based ZnO PENG devices with high flexibility [74-75]. The output voltage and average current density of this device were 3.2 V and 0.15 A cm^{-2}, respectively. This PENG may be used to build highly fragile cardiac sensors.

The piezoelectric coefficient (d_{zz}) of n-type ZnO is greater than that of eco-friendly piezo semiconductors. Due to the free charge carrier in n-type ZnO Semiconductor, the screening effect takes place to decrease the performance. In the semiconductor industry, defect engineering is key to increasing the device's functionality. Therefore, the ZnO device is also used in this approach to improve performance and increase applicability. Therefore, the researchers have significantly reduced free charge carriers by doping, annealing, and hetero junction methods. Doping is the controlled addition of impurities to the intrinsic semiconductor to alter its structural, optical, and electrical characteristics.

2.2.3 Various dopants for ZnO:

Doping is the introduction of foreign material in the intrinsic semiconductor to modulate its inherent properties such as electrical, optical and structural properties. The foreign atoms can supress the free charge carrier concentration in the ZnO piezoelectric material. There are several materials are doped in the ZnO lattice like rare earth elements, transition metal, and lanthanides.

The thermal solubility of the 3d-transition metal is 10 mol% higher than ZnO, which influences the spins quantity and charge carriers of the intrinsic ZnO properties [76]. Also, the piezoelectric coefficient of ZnO is 9.9 pC/N for a bulk and 12.4 pC/N for an oriented film, two orders lower than other materials [77,78]. Thus, numerous studies have

attempted to examine the doping effects of the ZnO piezoelectric characteristics. Pan et al. used the co-sputtering technique to dope Vanadium into ZnO. It was noticed the piezoelectric coefficient enhanced 10 times greater than pristine [79,80].

Similarly, Gupta et al. used a solution-based approach for doping vanadium into ZnO. The device was developed with a 2D ZnO nanosheet which attained a high current density of 1 $\mu A/cm^2$ with a 0.5 kgf load [81]. However, the piezoelectric coefficient is low, though it has ferroelectric characteristics. Ong et al. studied the influence of Copper doped ZnO behavior [82]. It observed that the d_{zz} improved to 80 pm/V, nearly 4 times higher than pristine ZnO. However, none of the transition metal doping techniques produced the desired output increases. In addition, the other transition dopants also give a similar phenomenon. As a result, the simultaneous studies of various dopants, such as alkali metals, post-transition metals, and nonmetals, on the piezoelectric property were explored. Several reports are doping with III- IV group elements (B, Al, Ga, In, Pb, Sn) which attain significant output performance than others [83-86]. Among these dopants, Sn is more compatible with the Zn due to close ionic radii (Sn^{4+} - 0.69 Å & Zn^{2+} - 0.74 Å). This enables Sn to fit into the lattice with minimal lattice distortion easily and enhances the electron carrier concentration [87-89]. Many studies have been reported on the physical and electrical characterizations of Sn-doped ZnO materials [90-92]. However, it has not been explored much in the piezoelectric performance enhancement.

2.3 literature survey on surface-modified TENG:

Though many factors influence the performance enhancement, such as work function, contact area, mechanical force, and speed, several techniques were reported with material work function and device architecture. However, there isn't much attention paid to boosting the material's surface charge density. Typically, chemical and physical modification are the potential methods for enhancing the surface charge density of triboelectric materials. Numerous methods have been involved in the chemical modification process, such as ion injecting [93,94], fluorinated surface [95], and molecular targeting

functionalization. However, limited methods evolved effectively in the physical modification, such as laser surface modification [96-100], lithography [101,102], moulding [103,104], and imprinting [105] for enhancing the surface contact area and charge density of the device.

This section reviews various methods involved in surface modification of the TENG.

Photolithography:

In 2012, Feng et al. modified the surface of the PDMS with three different patterns (pyramid, line, and cube) using a photolithography method to enhance the surface contact area shown in Figure 2.4. Among them, the pyramid pattern attains higher performance than the plain surface and other patterns.

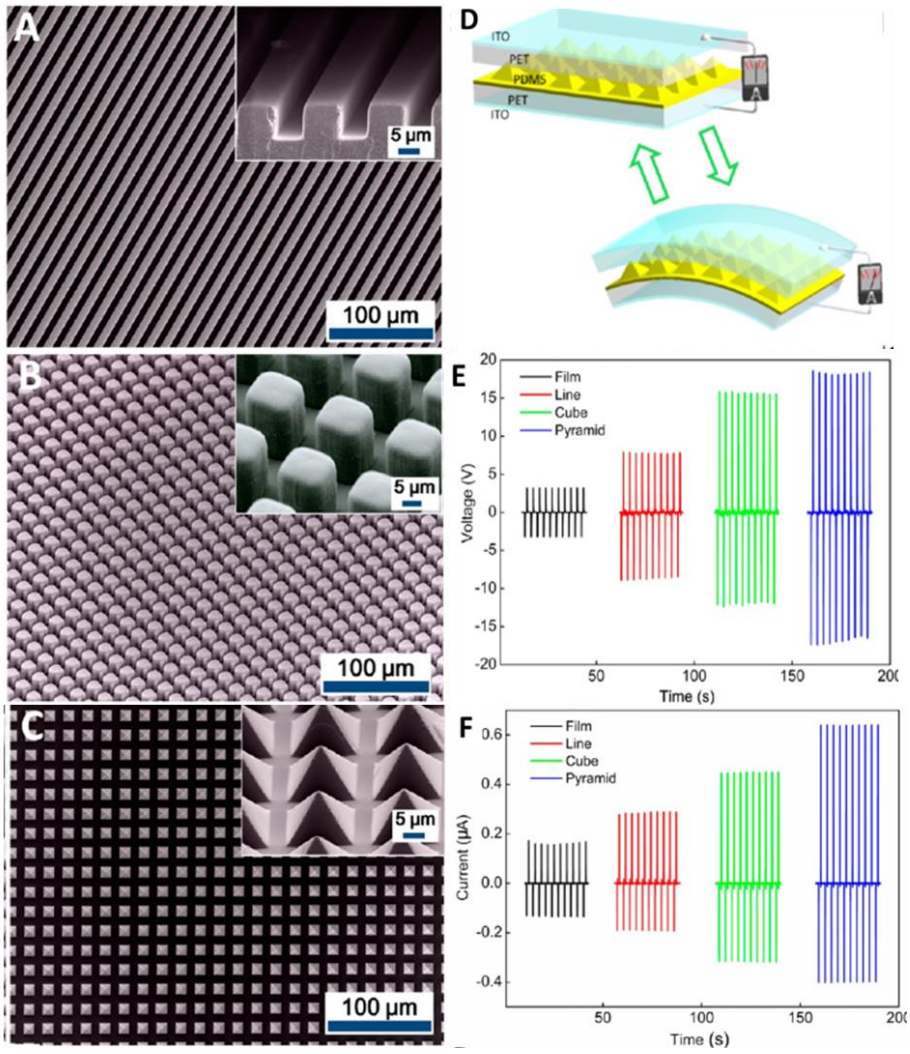

Figure 2.4 Photolithography modified PDMS surface with three different architectures

This structure has increased the capacitance and triboelectrification that enhanced the final output of the TENG. The generated output voltage and current of 18 V and 0.7 μA are four times higher than previous reports. Also, it has been demonstrated as a self-powered high-sensitive pressure sensor.

Self-assembly block copolymer:

Chang kyu et al. reported robust surface-modified method to fabricate nanoscale tune up the surface by block copolymer process in 2014, which enhances the surface characteristics of TENG. Three different nanostructures have been developed on a silica substrate for one part of the tribo layer, as shown in Figure 2.5.

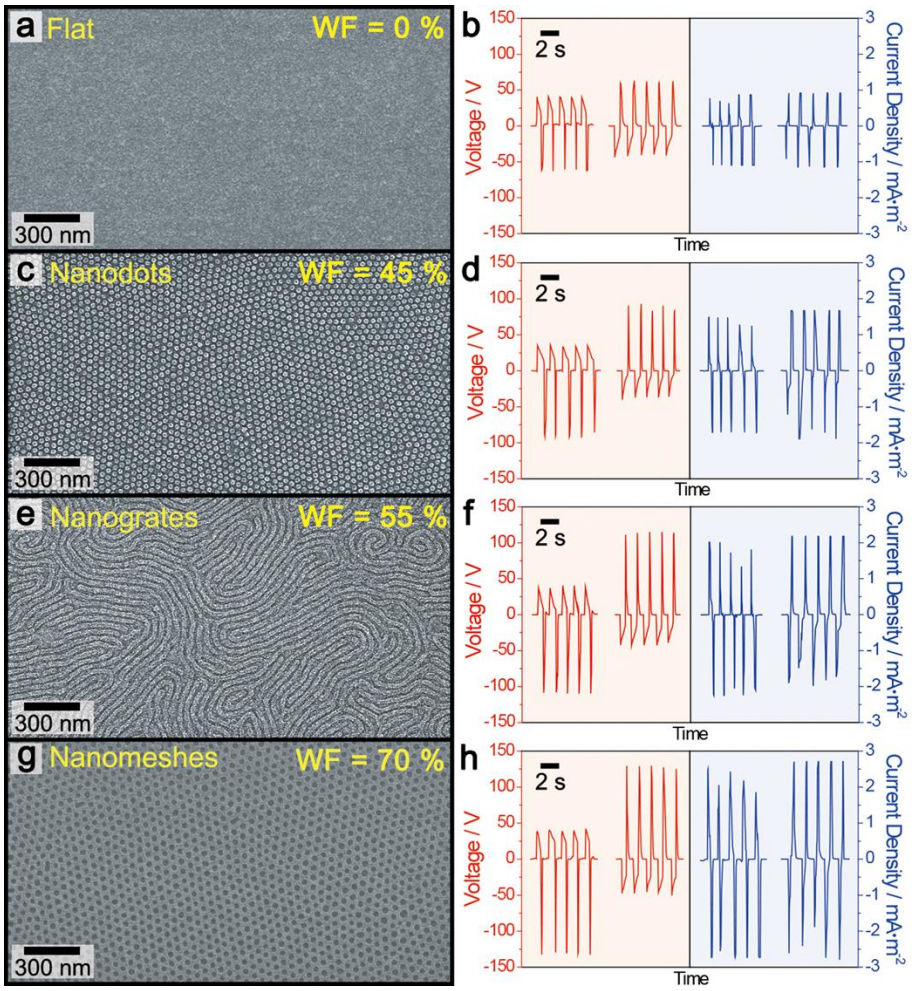

Figure 2.5 Block copolymer patterned nanostructures and their TENG performance

The performance enhancement of the TENG depends on the geometrical widening factor (WF) value. Hence the WF calculated concerning the flat surface morphology, approximately (nanodots, nanogrates, and nanomeshes) 45%, 55%, and 70%. As a result of this surface modification process, self-assembled BCP nanostructures with various WFs were crucial in boosting the friction effect and contact charging area in the triboelectric power generation. Comparatively, the nanomesh design attains 6.3 times higher performance than nonpattern TENG. The device generated an output voltage of 130 V and a current of 2.8 mA.

Mold replication method:

In 2016, Lokesh et al. demonstrated patterned TENG for a self-powered finger motion sensor. The pyramid pattern was built by the mold replication method, which is a low-cost-based sensor fabrication process and enhanced the TENG performance (Figure 2.6 (a-d)). Eventually, the human finger motion generated a peak voltage of 70 V and a current density of 2.7 $\mu A/cm^2$ with a 5 MΩ load resistance.

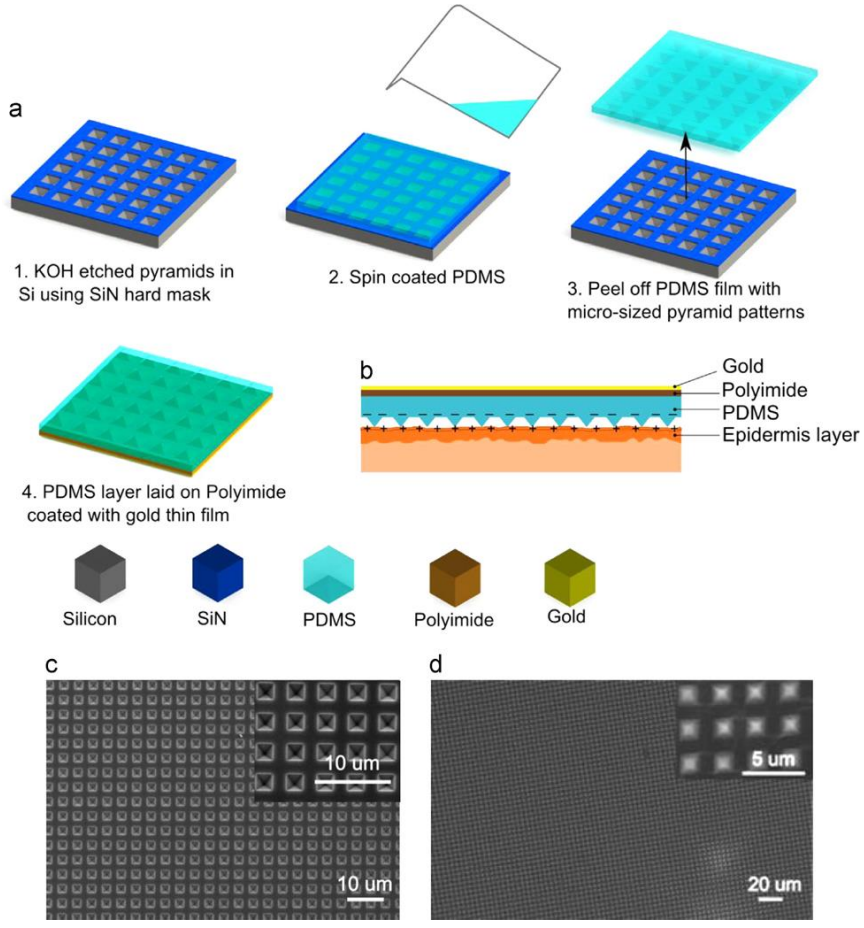

Figure 2.6 Mold replication patterning process

Roll-roll patterning:

In 2016, Lokesh et al. developed a large-scale TENG and self-powered pressure sensor using roll-to-roll UV embossing. Five different surface patterns have been investigated for the influence of morphology on TENG performance (Figure 2.7). Among them, large scale S3 device attains higher performance than others due to enhanced surface contact area and surface characteristics. Peak-to-peak voltage and current produced by LS-TENG were 344.63 1.37 V and 18.12 0.13 A, respectively. With the use of palm tapping, LS-TENG was shown to produce a power of 62.5 mW m^2. In addition, it shows the detection sensitivity of 1.33 V kPa^{-1}.

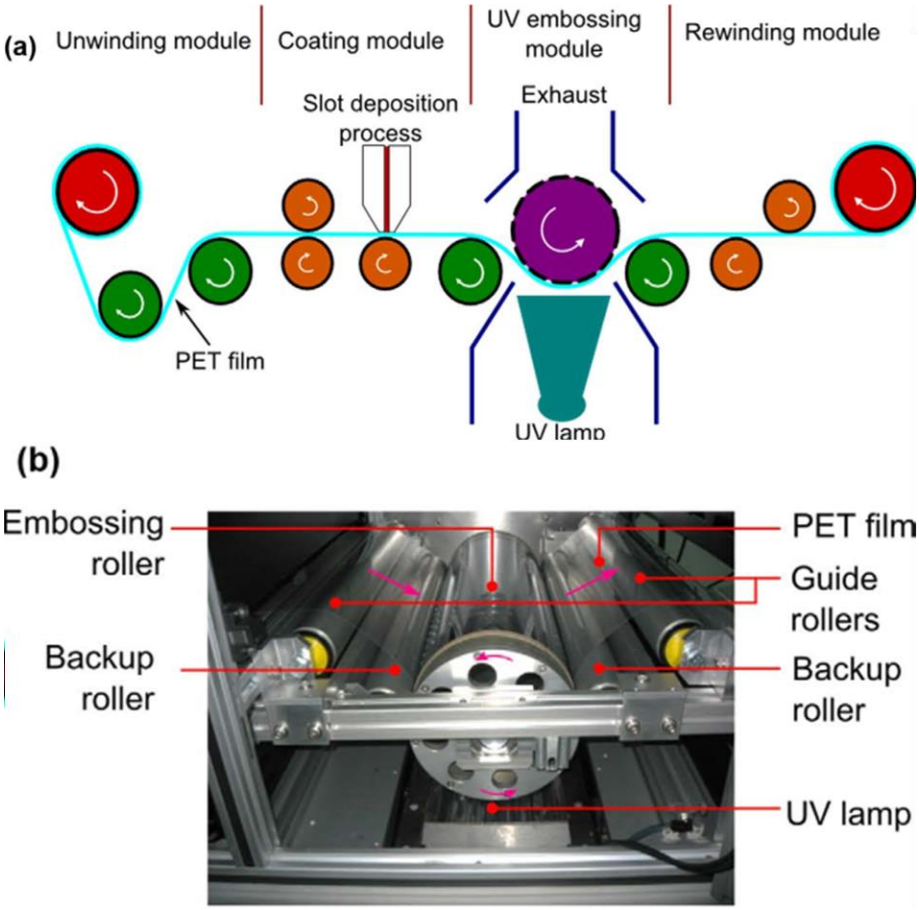

Figure 2.7 3D surface morphology of the various patterns and their voltage generation with the same force level.

Thermal imprinting lithography:

Bhaskar et al. proposed a low-cost, simple fabrication method of thermal imprinting lithography (TIL) for surface modification to enhance

triboelectric performance. The PTFE material was used for the surface patterning, and different morphology was generated with respect to varying imprinting forces (Figure 2.8). Additionally, the maximum level of surface roughness created by the micro-grooved architecture (MGA) PTFE polymer increased the effective contact area and surface charge density between the PTFE and Al electrodes of TENG. As a result, TENG's electrical output performance was improved. However, the optimized MGA-TENG generates the maximum output voltage, current, and charge density of ~320 V, 15 μA, and 44 μC m^{-2}, respectively.

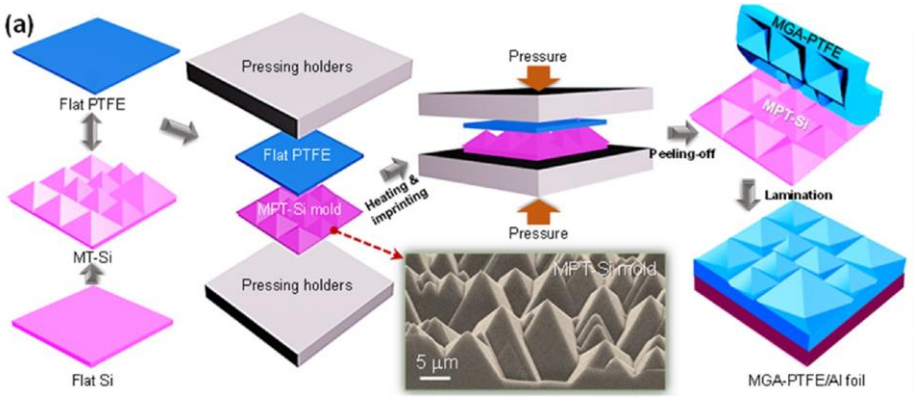

Figure 2.8 Schematic of MGA TIL process, device assembly, and surface morphology.

Sandpaper template patterning:

Xu-Wu et al. proposed a novel methodology to improve the surface characteristics of the TENG layer by sandpaper templating. Different sandpaper grit sizes achieved various surface morphology, as shown in Figure 2.9.

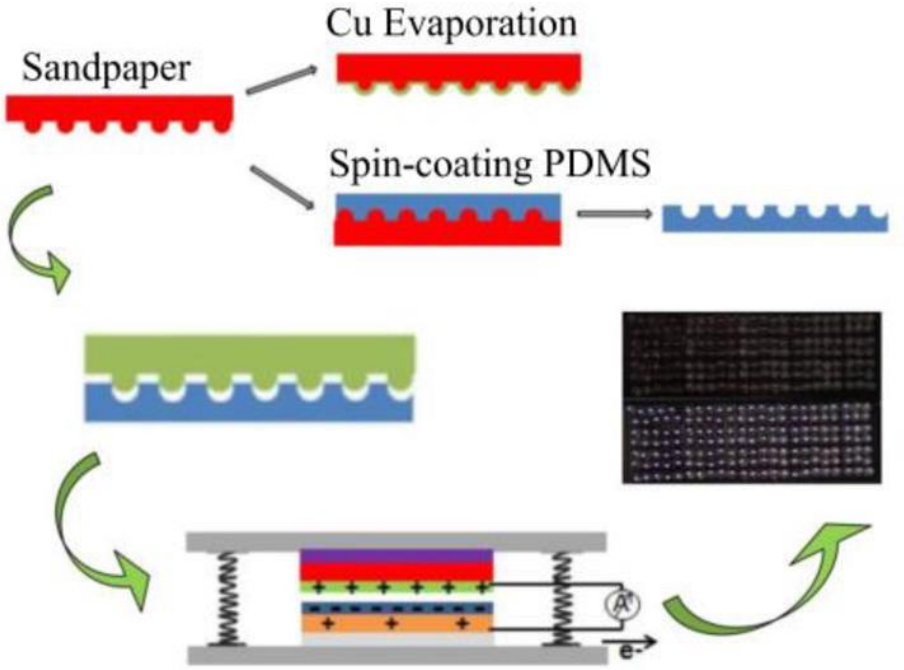

Figure 2.9 SEM images of copper and PTFE patterned surface with different grit sizes

Several combinations of morphologies were organized and investigated their TENG performance. Compared to plain and single-side surface patterns, the two-sided pattern attains maximum output voltage, current density, and transferred charge quantity of 200 V, 3.89 mA/m^2, and 76 nC due to sufficient frictional contact and improved charge density.

Laser surface patterning:

The above processes have their limitations, such as size control, poor scalability, low throughput yields, and the requirement of an expensive high vacuum system during the fabrication process. Though the surface replication process has shown substantial triboelectric enhancement [104,105], the development and pouring of liquid phase material at micro/nanoscale mold is complex and expensive compared to other techniques. Hence as an alternative texturing process is needed to reduce the complications in fabrication procedures and increase the production rate.

Compared to other processes, laser texturing provides an enhanced surface contact area of the substrate [106], which is the key factor for the enhancement of triboelectrification. Also, this process can develop a consistent (as desired) pattern. Laser surface patterning (LSP) can be

employed to develop various macro, micro, and nano features with high spatial resolution. It has potential advantages such as less processing time and no requirement of masks or toxic chemicals to develop the structures [107,108]. LSP is a simple method that changes the chemical and surface properties of the material. In the LSP process, the optical energy irradiated on the top surface leads to the heating of the material. Consequent irradiation would melt or evaporate the material and eventually causes patterning of the surface. The non-contact feature of the LSP process helps avoid contamination and oxidation failures in the TENG device. There are few studies on using a laser to modify the substrate to fabricate the TENG device. Ji Huang et al. have developed different hierarchic structures by femtosecond (fs) laser direct writing method (Figure 2.10) and enhanced the output performance by 21 times compared to pristine TENG [109]. R. Wang et al. have developed laser textured, low-cost biodegradable TENG devices for self-powered nano-systems [110]. Kim et al. have used an fs laser texturing on the polydimethylsiloxane layer and improved the output power by two folds [111]. Therefore, laser surface patterning is a suitable candidate for enhancing the performance of TENG devices.

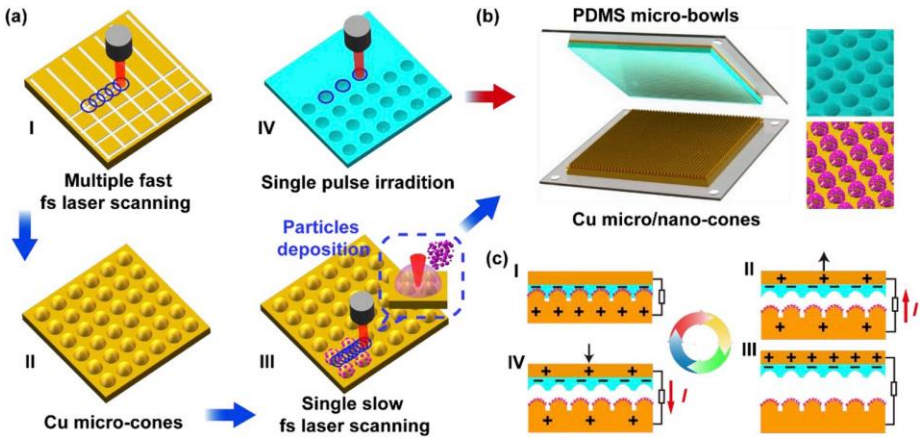

Figure 2.10 SEM images of various laser patterned structures and 3D surface topography.

2.4 Summary

Most of the PENG and TENG device materials and their substrates are not recyclable and biocompatible to the ambient. Additionally, the existence of few recyclable and biocompatible PENG and TENG

materials shows lower power density compared to the counterpart materials, which are due to different physical and chemical attributes. In general, various approaches have been employed to enhance the PENG and TENG material performance. In particular, for improving PENG materials properties, doping, annealing, and interfacial modification techniques have been used. Similarly, to enhance the output performance of the TENG, many factors have to be considered, such as surface contact area, mechanical force, contact speed, material work function, and relative humidity. Many reports are available related to material work function and various device architectures. Recently, the researchers are concentrated to modulate the surface charge density and increasing the output performance of the materials by chemical and physical modification. Several methods have been involved in the chemical modification process, such as ion injecting, fluorinated surface, and molecular targeting functionalization. However, limited methods evolved effectively in the physical modification, such as laser surface modification, lithography, molding, and imprinting to enhance the surface contact area of the device.

This thesis work was directed with the flowchart shown in Figure 2.11. After thorough literature survey, the motivation and objective of the thesis formed and carried out with the same. Initially, we have developed the eco-friendly tin-doped ZnO PENG device. We also investigated the device's physical properties and piezoelectric performance and studied its practicability. Subsequently, the commercial PET material performance has been enhanced with laser 3D pattern and interfacial layer effect. The as-fabricated TENG device was demonstrated under various mechanical parameters to investigate its energy harvesting ability.

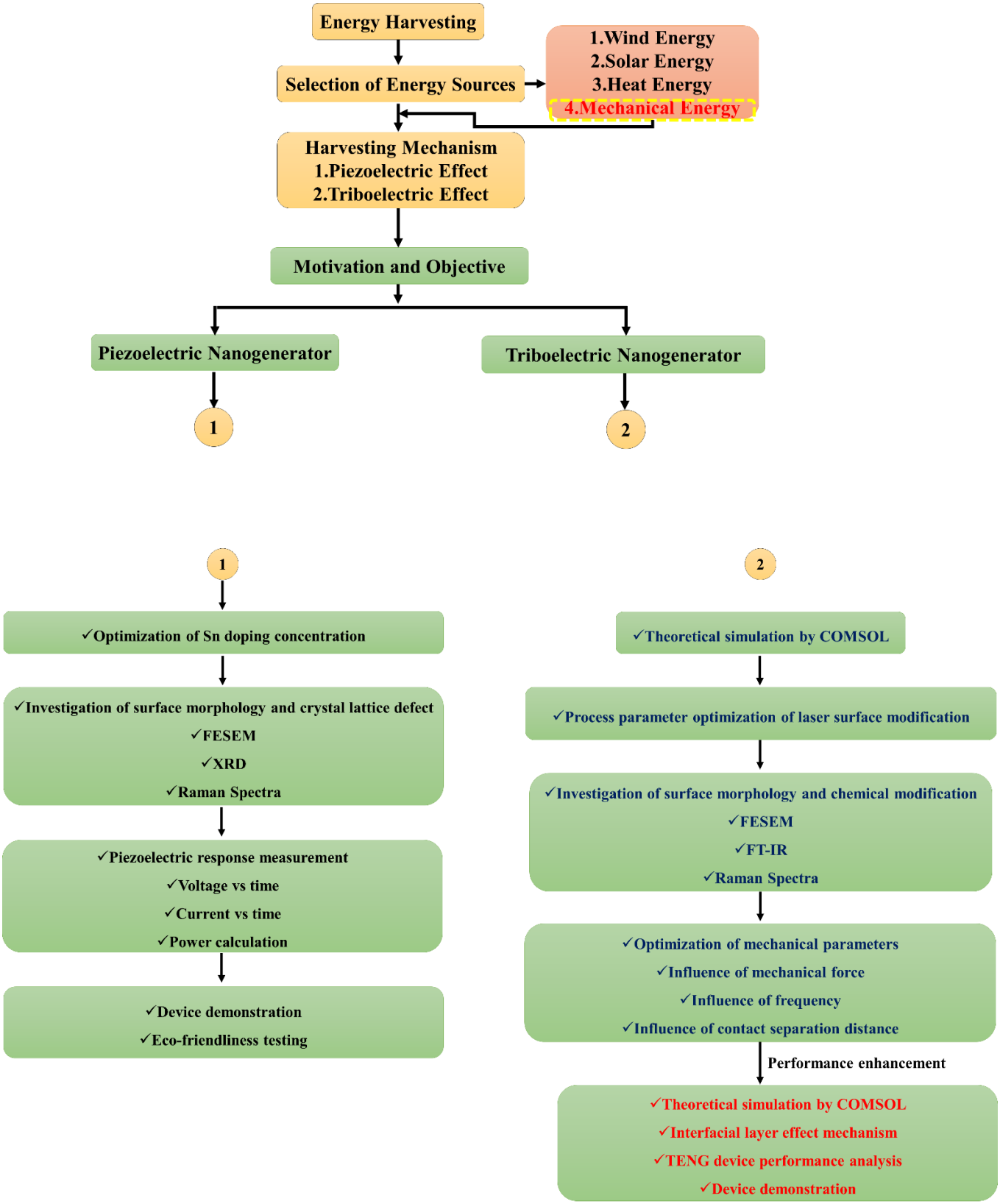

Figure 2.11 Flow chart of the thesis

Chapter 3

Development of Sn doped ZnO-based eco-friendly piezoelectric nanogenerator for energy harvesting applications

3.1 Introduction

Most of the PENG devices have been developed on a rigid substrate such as ITO, GaN, sapphire glass, silicon, metal sheets, and plastic fibers [19,20]. It is observed that these substrates are rigid, not even biodegradable, through which the mechanical energy cannot be harvested from the intricate position of the substrate. Moreover, such substrates are increasing environmental pollution. Therefore, green, raw, and recyclable substrates could be an appropriate alternative for fabricating electronic devices.

This chapter focuses on a novel approach adopted to investigate the piezoelectric response of Sn doped ZnO thin film on the paper substrate, where the effect of different doping concentrations was studied. The thin film was developed on the paper substrate via the drop-casting method, where different doping concentrations of Sn such as 2.5 %, 5 %, 7.5 %, and 10% were optimized. The morphology and crystallinity of doped ZnO thin film were characterized by field emission scanning electron microscope (FE-SEM), X-ray diffraction, and Raman spectra, respectively. Further, the piezoelectric performance of the synthesized PENG device was evaluated with the application of load via a linear motor. Therefore, such devices can be used in drums and musical instruments where the non-uniform impulsive load is usually applied.

3.2 Experimental

3.2.1 Synthesis of Sn doped ZnO

Materials

Zinc nitrate hexahydrate [Zn $(NO_3)_2 \cdot 6H_2O$, 98%, Sigma Aldrich], and Hexamethylenetetramine (HMTA) [$C_6H_{12}N_4$, 99%, Sigma Aldrich] were used to grow the ZnO nanostructure. Tin Chloride II [$SnCl_2.2H_2O$, 98%, Sigma Aldrich] was used for doping. Polyvinyl alcohol (PVA) [$(C_2H_4O)n$ Tokyo Chemical Industries] was used as a binder for the composite thin film.

Synthesis of ZnO powder

The Hydrothermal (or solvothermal) method is a useful technique for developing 1D nanostructures such as nanowires, nanoneedles, flowers, and nanorods. Here, a wet chemical reaction occurs upon dissolving precursors in the water/organic solvents at temperatures between 50°C to 250°C. This method is efficient for the synthesis of ZnO nanostructures to attain more crystalline defects, which lead to more oxygen vacancies, and thereby inherent defect improves the optical and electrical properties of ZnO nanostructures. Co-precipitation using the hydrothermal method is known to have a uniform dispersion [112,113]. Furthermore, the hydrothermal method takes place at low temperatures, which avoids phase transformation compared to other techniques. The 50 mM Zinc nitrate hexahydrate salt was taken as the precursor of the ZnO solution. It was dissolved in 60 ml of deionized (DI) water and stirred vigorously for 30 min to attain a transparent and homogenous solution.

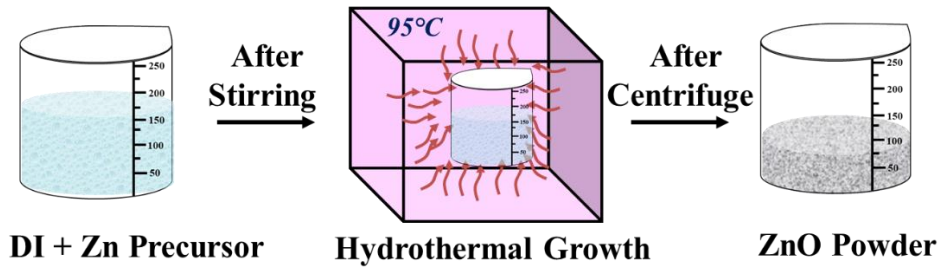

Figure 3.1 Schematic diagram of ZnO synthesis and film deposition

During stirring, the HMTA was added to maintain pH seven by increasing the OH^- ions and precipitation of Zn^{2+} ions [114,115]. In case of doping, $SnCl_2$ flakes was introduced along with Zn precursor salt itself at different Sn concentration (2.5%, 5%, 7.5% and 10%) [83, 116]. Then HMTA was added during stirring, which turned the doped solution into a milky color. After stirring, the solution was kept in a hot air oven for 6 hr at 95^o C. The as-formed precipitate was cleaned several times by centrifugation with DI water. The collected precipitation was dried at 90^o C for a few hours. Figure 3.1 shows the schematic diagram of the material synthesis and device fabrication process.

3.2.2 Fabrication of paper-based PENG:

The photographic paper sheet of dimension 2.5 cm × 2.5 cm × 0.0254 cm was used as the substrate for fabricating piezoelectric device. The carbon conductive ink was deposited as the bottom and top electrode of the device using the brush coating method [117]. Each electrode was coated four times to ensure film quality and uniformity. After coating, the electrode was dried at room temperature. Meanwhile, 5 gm of PVA salt was dissolved in 100 ml of DI water and stirred well for 2 hr at 95 ^{o}C. This has yielded a transparent viscous solution without thermal decomposition of the polymer [118]. The as-synthesized ZnO/ZnO+Sn powder (mg) was mixed in viscous PVA solution (ml) at 10:1 ratio [119,120]. The mixture was drop cast to form the film and cured at 90^{o}C for an hour. The connections were taken from the top and bottom electrodes using 0.1 mm copper wire with silver paste. Then the device was covered with anti-static tape to prevent the electrostatic effect. The developed PENG device schematic is shown in Figure 3.2.

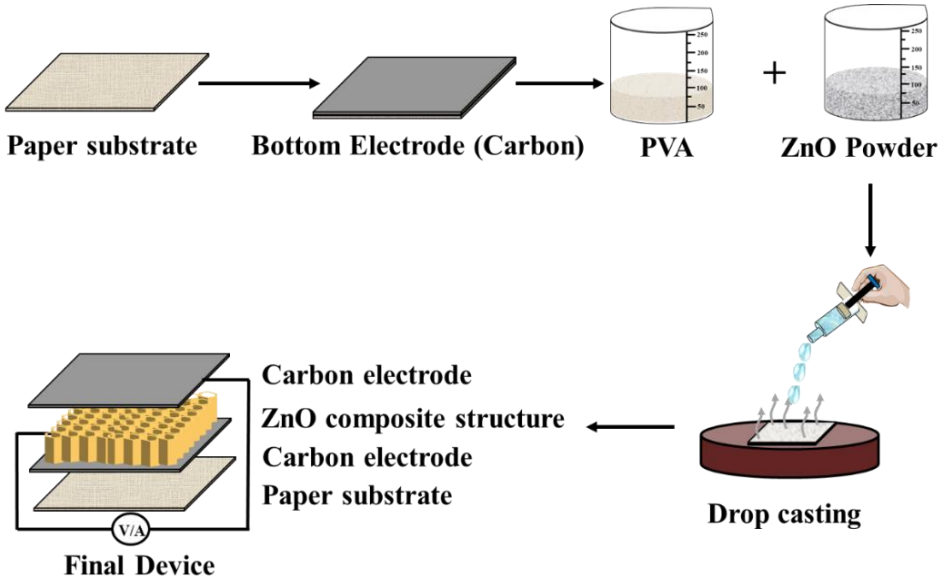

Figure 3.2 Schematic of Sn doped ZnO piezoelectric device

3.2.3 Characterization

The surface morphology and Energy Dispersive X-Ray spectroscopy (EDS) of doped and pristine powders were examined using a field emission scanning electron microscope (FESEM, Carl Zeiss Sigma series supra-55). The crystal structure and phase pattern were evaluated by powder XRD analysis with two thetas from 30^{o} to 70^{o} (Rigaku Smart Lab system). Raman spectra was used to study the Lattice defects and vibrational modes of doped and pristine samples between 300 to 800 cm^{-1} wavenumbers with an excitation wavelength of 514 nm (LabRAM HR Evolution; Horiba, Japan). The piezo output performance and I-V characteristics were measured using the Keithley 2612B source meter.

3.3 Result and discussion

The Sn doping concentration was optimized based on piezoelectric performance. We have observed improved piezoelectric response for the Sn doping concentration occurs until 2.5 %, and the performance degradation takes place for the Sn doping > 2.5 %. Therefore, we have not discussed the effect of higher doping concentrations of PENG devices in this study.

3.3.1 X-ray diffraction and Raman spectroscopy

Figure 3.3 (a) shows the XRD graphs of pristine and Sn-doped ZnO crystalline structures. The ZnO crystallinity and different crystal phases were confirmed with diffraction according to the JCPDS data file (no.36-1451). We have observed dominant peaks of ZnO with various planes, ensuring the crystalline structure. However, any predominant secondary phase of Sn was not detectable from XRD graphs. Moreover, we have observed significant peaks' intensity reductions for 2.5% Sn doped ZnO nanostructures. This might be due to smaller ionic radii of Sn^{4+}(0.069 nm) ions than Zn^{2+}(0.074 nm), where the Sn^{4+} dopant ions trigger Zn^{2+} parent ions in the ZnO plane by the substitutional effect [89,121]. In the case of 5% Sn doped ZnO, the c-axis peak intensity reduced and shifted towards a higher angle, which could be attributed to more occupancy of Sn^{4+} ions in the ZnO lattice [89,90,122] (Inset of Figure 3.3 (a)). In addition, the shape of nanorods has evolved and reduced crystallinity. These results confirmed that the higher concentration of Sn led to deterioration in the crystallinity and peak intensity of as-developed nanostructures.

Figure 3.3 (b) shows the Raman analysis of Sn doped, pristine ZnO crystallinity, and lattice defects. The C6v4-P63mc space group described the hexagonal wurtzite structure of pristine ZnO crystallites and lattice defects. The irreducible representations ($\Gamma = 2A_1 + 2E_1 + 2B_1 + 2E_2$) lead to classifying the different modes of hexagonal structure, such as twelve phonon modes, nine optical phonons, and three acoustic modes. A_1 and E_1 are denoted as Infrared and Raman active modes that are divided into the transverse and longitudinal optic modes. E_2 mode consists of low and high-frequency phonons in Raman active mode, whereas B_1 is inactive Raman mode [123-125]. The predominant sharp peak of pristine ZnO hexagonal wurtzite phase and good crystallinity was confirmed at a wavenumber of 438 $cm^{-1,}$ which belongs to E_2 high phonon mode and is accompanied by oxygen sublattice [126-128].

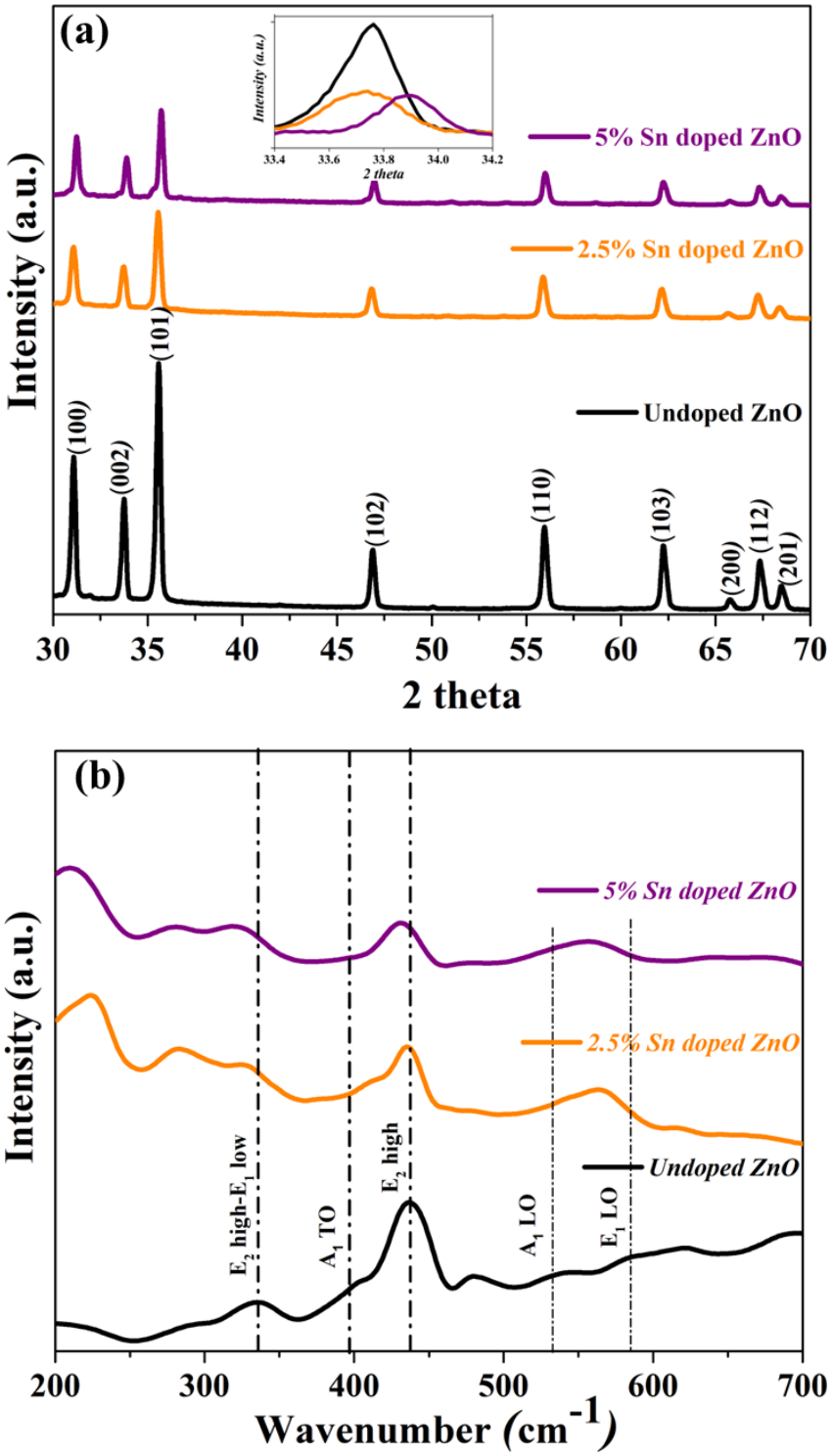

Figure 3.3 (a) X-ray diffraction pattern of doped and pristine ZnO powders (b) Raman shift of doped and pristine samples

The broad peak of 337 cm^{-1} wavenumbers was assigned to second-order Raman phonons (E_2 high-E_2 low). The weak peak of 397 cm^{-1} was consigned to A_1 transverse phonon mode. The peak intensity deteriorated upon doping Sn, which might be due to the formation of

Sn-ion. In general, the high intensity of Raman active E_2 mode is usually attributed to the better optical and crystalline properties of the material (undoped ZnO). Herein, the low intensity of E_2 mode observed in Sn-doped ZnO indicates the reduced crystallinity of ZnO upon the formation of Sn-ion [129,130]. A significant peak was exhibited at 570 cm^{-1} that confirming the Sn doping. The broad peak of 534 cm^{-1} and 585 cm^{-1} are attributed to A_1LO and E_1 LO. The broad peak confirms Sn occupies into ZnO lattice, while the Raman peak shift and broadening effect are relevant to particle size [125,131,132]. Above 2.5% Sn concentration degrades Raman spectrum peak intensity, which is due to crystalline defects of doped ZnO nanostructure. In the case of XRD, the excess Sn^{4+} occupies in ZnO Lattice structure via interstitial defect, suppressing the crystallinity.

3.3.2 Surface morphology

Figure 3.4 shows the FESEM images and EDS graphs of Sn doped and pristine ZnO nanostructures. The dominating elements of Zn and Sn were confirmed through EDS characterization. It was observed (figure 3.4(a)) that the synthesized ZnO nanoparticles have attained a hexagonal nanorod shape. But the Sn doped ZnO has a variation in hexagonal nanorod. This may be due to the effect of Sn ions in ZnO observed in figure 3.4(b, c). The diameter of the nanorods has increased with the increase in dopant concentration. The increase in diameter of the ZnO nanorods can be ascribed to the intrusion of Sn^{4+} ions in the interstitial spaces of the ZnO crystal structure. Furthermore, the increase in the interspaces with the increment in doping as reported in the study from the literature [133 and references therein]. Using ImageJ software, the diameter of nanorods was measured for pristine ZnO, 2.5%, and 5%Sn doped ZnO of 185 nm, 230 nm, and 250 nm, respectively. EDS graph revealed the presence of Zn and O elements in pristine ZnO (Figure 3.4(d)) and typical Sn peak observed in the doped sample (Figure 3.4 (e,f)).

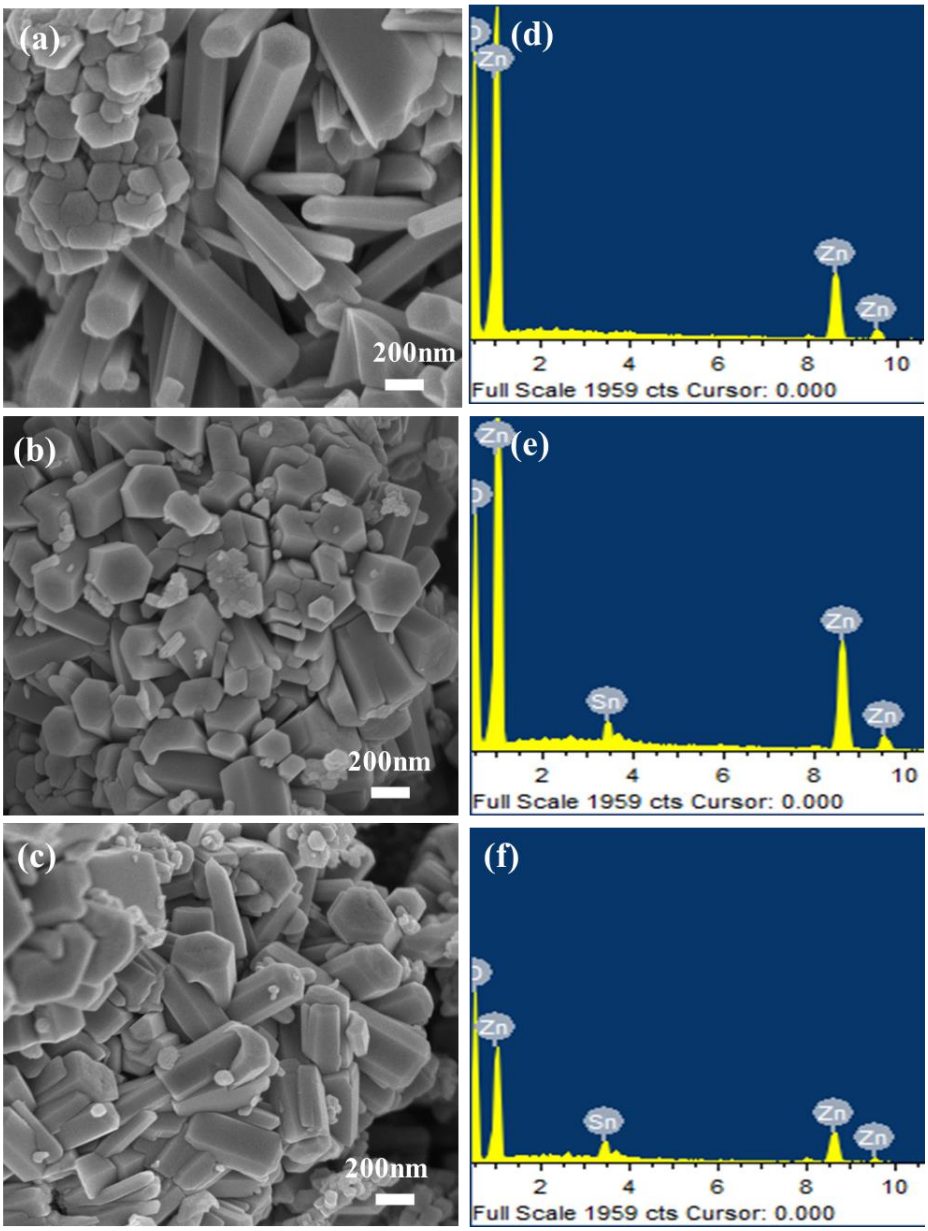

Figure 3.4(a) FE-SEM image of pristine and (b-c) Sn doped ZnO powder nanostructure and (d, e, f) shown the elemental analysis graph(EDS)

3.3.3 Electrical characterization of PENGs

Piezoelectric Output response:

To evaluate the piezoelectric performance, the device was tested using a linear motor drive actuator with compressive mechanical stress of 30 N and a frequency of 5 Hz. The compressive stress distorts the ZnO lattice symmetry and leads to dipole formation. Due to the non-net zero dipole moment, the potential gets developed across the device. The non-equilibrium in the charge center enables the electron to drive through the

surface top electrode to the bottom electrode [134] and generates the positive potential peak in measurement. On removal of the external stress from the device, the dipole moment gets vanishes. Then the electron flows back to the initial position and generates the negative potential peak [135].

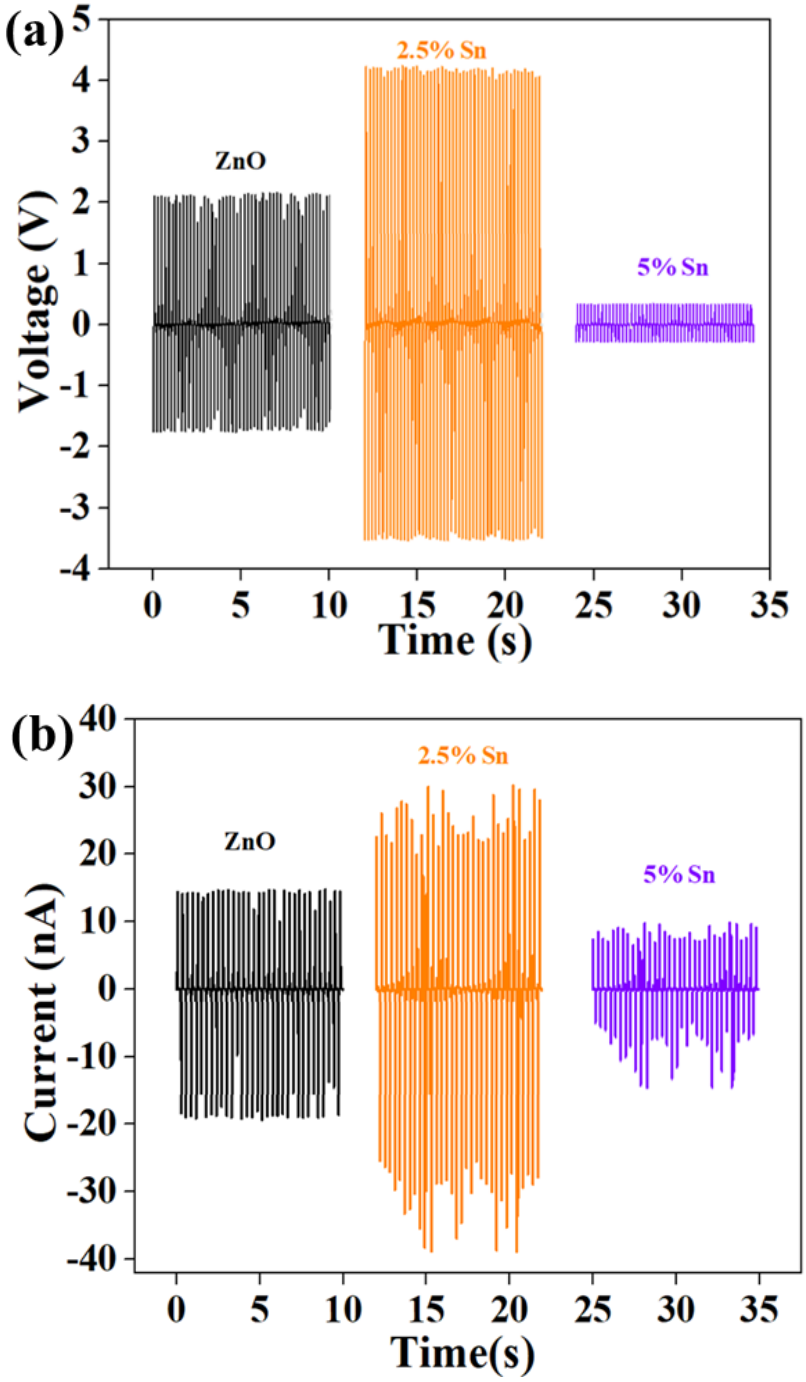

Figure 3.5 (a) and (b) voltage and short circuit current measurement of pristine and different percentages of Sn doping concentration.

Figure 3.5(a) and (b) show the output voltage and current of pristine and Sn doped PENG devices. It was observed that the pristine PENG device generates the peak-to-peak voltage and current of 3.86 V and 33.84 nA. It is essential to optimize the doping concentration to determine the highest performance. Thus, the Sn doping concentration was varied with a 2.5% interval. The 2.5% Sn doped PENG device has obtained higher output of 8.41 V and 67.92 nA, which is due to the Sn^{4+} ions producing two free charge carriers in the Zn^{2+} site via substitutional effect [136]. In our scenario, adding a binder to the material raises the device impedance even more. As a result of these factors, the device has a high voltage and low current value. Previous research has found a substantial relationship between dopant ionic radii and piezoelectric characteristics. Further, increasing the Sn concentration above 2.5%, the performance gradually degrades, which is due to the excess hole and defect concentration during the growth process and leads to the suppression of the piezoelectric performance. Hence, this effect lowers the piezoelectric potential for higher values of Sn doping (> 2.5%). Moreover, a greater number of Sn ions are unable to occupy their respective lattice position in the Zn lattice leading to the interstitial effect, which can also affect the piezoelectric potential [89,90,136]. This effect was hampering the generation of piezoelectric potential and current at 5% of Sn.

Further investigation on the effect of charge carrier, V-I characteristics of Sn doped ZnO, and pristine ZnO samples were examined, which were plotted in absolute scale of current. The planar electrode of the device was developed with a gap of 500 μm schematic diagram of the V-I samples shown in Figure 3.6 inset image. It observed that the dark current decreased in 2.5% Sn doped ZnO sample due to excess free charge carrier. Further increasing Sn concentration (5%), more free charge carriers accumulated in the sample screening the piezo potential [137]. Hence resistivity influences the screening of piezoelectric output performance.

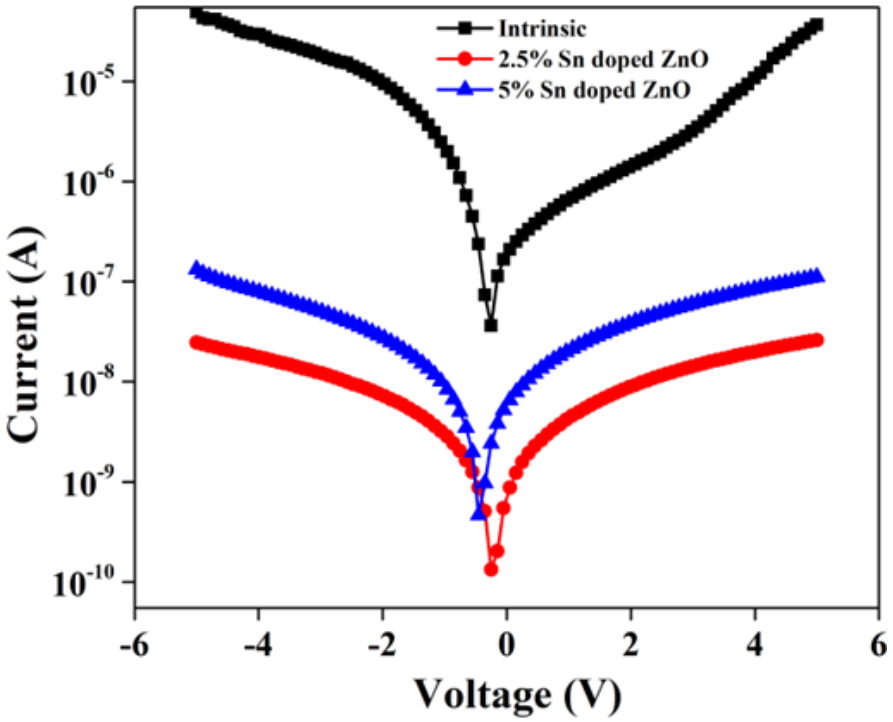

Figure 3.6 I-V characteristics of the pristine and 2.5% and 5% Sn doped ZnO PENG device

Device demonstration:

Further, the piezoelectric performance of the ZnO-based nanogenerators was demonstrated in musical drums application using the hand stamping method (figure 3.7).

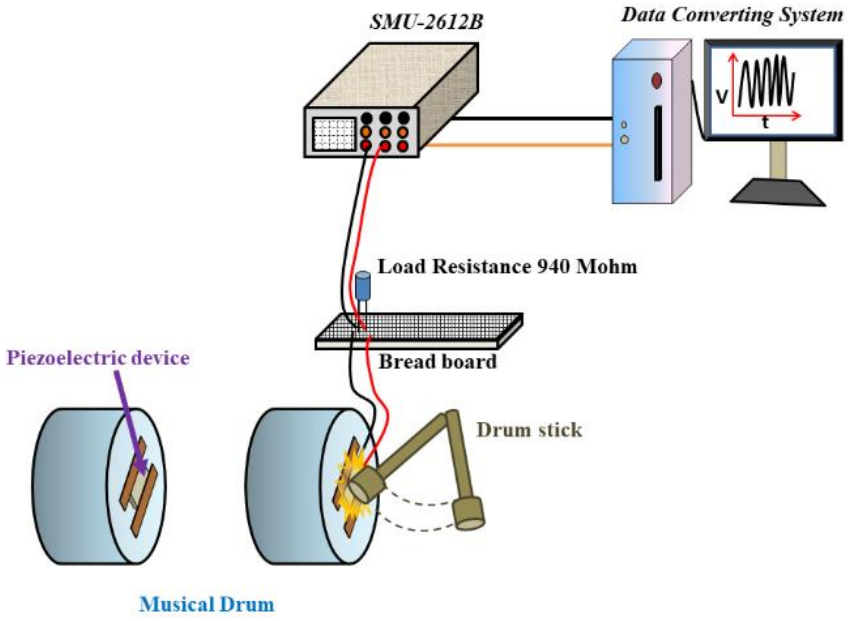

Figure 3.7 Shows the schematic diagram of the proposed application (musical drums)

The musical drums need to be hit with specific patterns at different loads to deliver the right music. Here, uneven hand stamping has been made over the device, having a load in the range of 4 N to 22 N. 940 MΩ load resistance was used across the circuit to measure the open-circuit voltage. The uneven hand-stamping induces compressive stress on the device [139,140].

The major positive and negative potential peak is shown in figure 3.8(a). Based on the above mechanism, the pristine ZnO device characterized the piezoelectric performance and plotted graph shown in figure 3.8(b) and (c). The 4 N force applied by hand stamping has attained the least output voltage and current of 0.12 V and 1.2 nA. But the higher force (22 N) achieved a maximum output voltage, and a current of 2.15 V and 17 nA is shown in Figures 3.8(b) and (c). The reason for applying a non-uniform force on all the devices was based on drum stick musical playing. Based on the load variation, positive and negative peaks are displayed. The 2.5% Sn doped device has highly enhanced the output voltage, and current of 4.15 V and 36 nA for maximum force (22 N), the minimum force (4 N) has obtained the least voltage, and the current of 0.18 V and 1.12 nA is shown in fig. 6(b) and (c). The 5% Sn doped ZnO device performance has obtained a lower output voltage and current of 0.26 V and 12 nA at 22 N, shown in Figures 3.8(b) and (c).

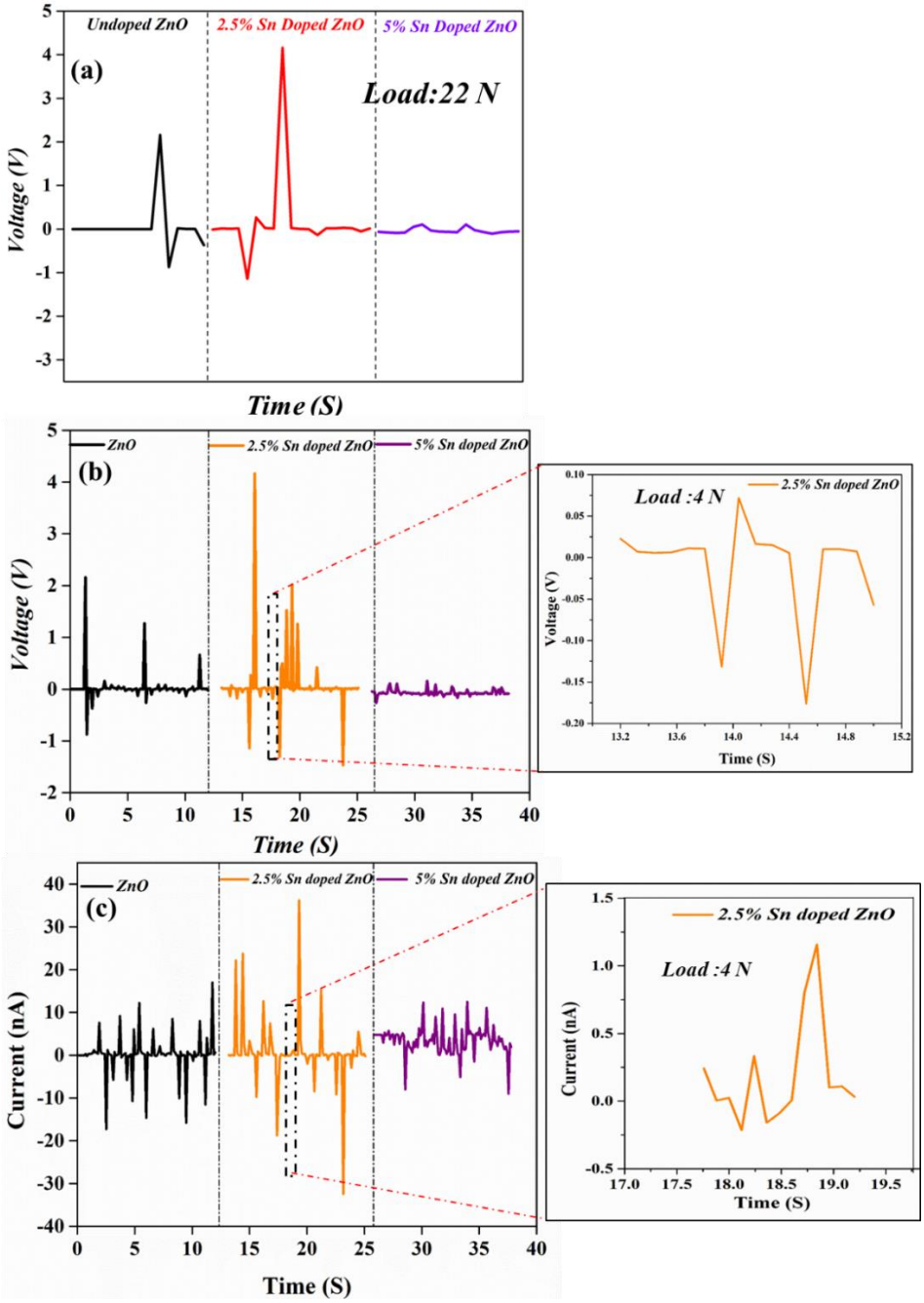

Figure 3.8 (a) Positive and negative peak voltage at 22 N (b, c) open circuit voltage and short circuit current measurement of pristine ZnO and Sn doped ZnO PENG (d) IV characteristics of doped and Pristine ZnO

Piezoelectric Power

The paper-based piezoelectric nanogenerator was widely used as a sensor or self-powering system in MEMS applications. The proposed application is suitable for working with different hand stamping

conditions for harvesting piezoelectric power by paper PENG device, in the same way, all devices performed for power generation.

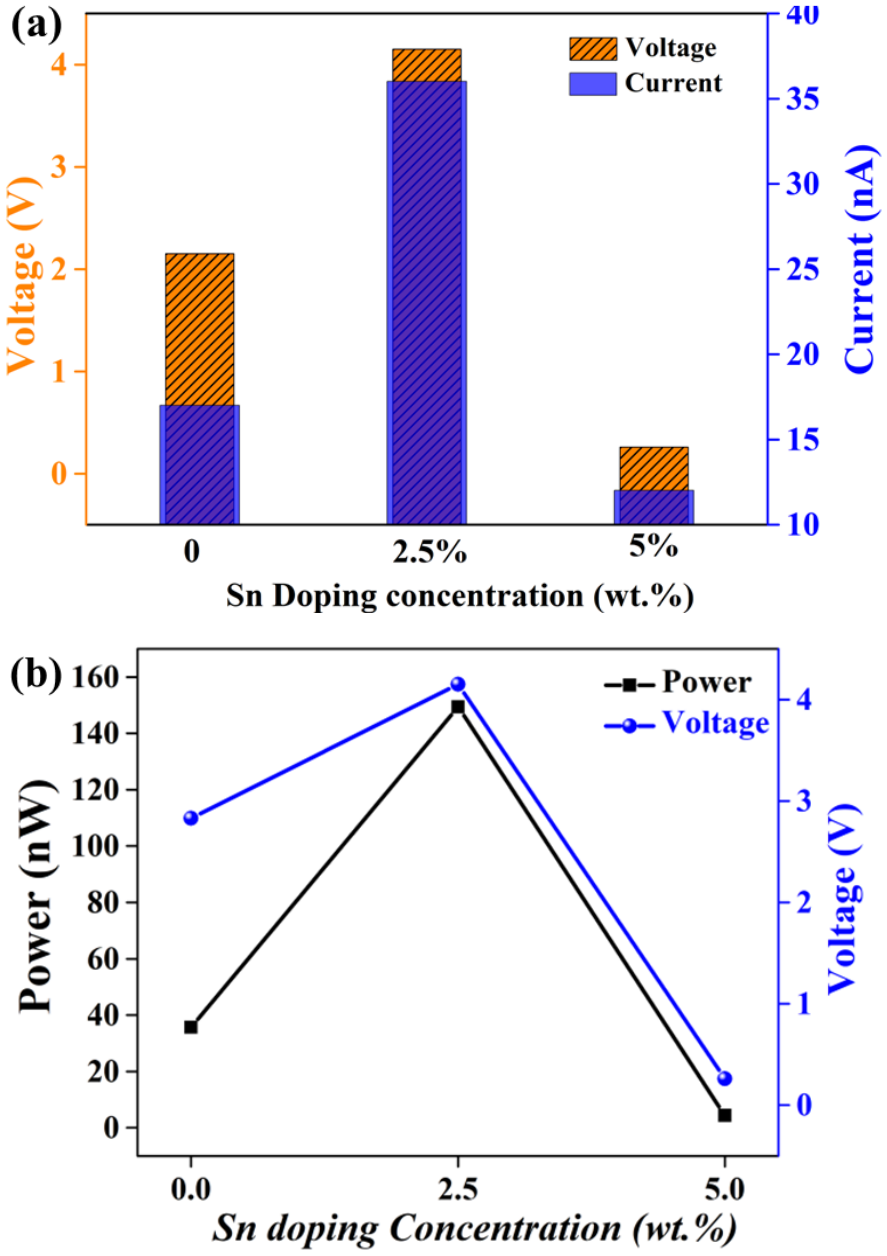

Figure 3.9 (a) shows the derived graph of current and voltage (b) power generation by the different doping concentration

Maximum force leads to higher lattice distortion by strain phenomenon that generates more power. Figure 3.9(a) shows the maximum output voltage and current for different Sn doping concentration (0%, 2.5% and 5%) for maximum force (22 N). The 2.5% Sn-doped ZnO device has attained maximum voltage (4.15 V) and current (36 nA) as compared to other Sn-doped ZnO devices. In particular, the higher output voltage

observed for the 2.5% Sn doped ZnO device is due to the reduced electrical conductivity or increase in resistivity. In other words, the higher resistivity leads to a higher potential drop. The reduction in the electrical conductivity can be associated with the increased strain in the ZnO crystal structure and further reduce the electron mobility [138]. In addition, the calculated power was plotted and shown in figure 3.9(b). The pristine PENG device generates 47 nW at 2.83 V with instantaneous force. After 2.5% Sn doping, the PENG device generates 149 nW at 4.15 V because two charge carriers occupy the lattice site that reducing the resistance of the device. Due to more positive charge carrier accumulation in 5% Sn doped device, the power generation was degraded to 3.12 nW at 0.26 V. So, the 2.5% Sn doped ZnO of paper PENG is more suitable for eco-friendly vibration energy harvester as well as the sensor.

Investigations on the biodegradability:

To investigate the eco-friendliness of the 2.5% Sn doped ZnO sample was immersed in natural soil for 14 days at room temperature with the open condition. The digital image was taken on days 1, 3, 7, 10, and 14 (figure 3.10). It is clearly visible the fungus started growing on the samples after the second day, which was caused by carbon electrode. Similarly, fungi completely covered the sample on the 10^{th} day. It was observed that the sample started degrading on the 14^{th} day, and the boundaries were completely decomposed when we took the sample from the soil. Hence, it affirms that the fabricated Sn doped ZnO PENG is eco-friendly to nature.

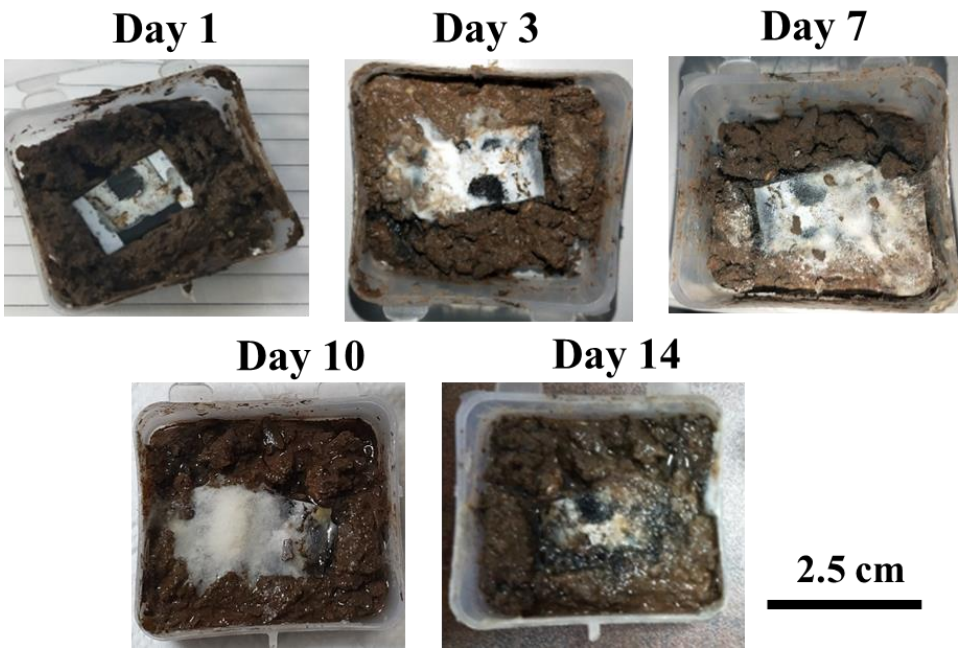

Figure 3.10 digital image of 2.5% Sn doped ZnO device immersed in natural soil

3.4 Summary

In summary, the Sn/ZnO/PVA PENG device was effectively developed using composite method.

- The doping concentration has been varied from 0-10% with 2.5% interval, in order to achieve the maximum output performance of the PENG device.
- The FESEM technique also confirms the increase in the diameter of the nanorods (185 to 250 nm) with the increase in Sn dopant concentration. Furthermore, EDS analysis confirms the presence of Zn, Sn, and O elements for uniform dispersion in Sn-doped ZnO.
- There is no secondary phase formation observed from the Sn doped ZnO by XRD. The broad peak at 534 cm^{-1} confirms the existence of Sn into the ZnO lattice.
- The pristine ZnO PENG performance device was enhanced two folds by 2.5% Sn doping with 30 N force. The piezo potential and current increased from 3.86 V to 8.41 V and 33.84 nA to 67.92 nA, respectively with the maximum power of 149 nW.

- The 5% Sn doped device performances were highly degraded due to excess positive charge carrier screening the piezo potential and current 0.26 V and 12 nA.
- We have proposed that the energy can be generated from musical drums in which the load is non-homogeneous in developing the music.
- The eco-friendliness of the Sn-doped ZnO PENG was studied by soil biodegradation test.

However, the output performance of the doped and pristine PENG device is not sufficient to power the microwatt rating electronic device, though it is flexible and eco-friendly to nature. An alternative approach is available for mechanical energy harvesting called triboelectric nanogenerator, which can power the micro and microwatt rating electronics devices. It is investigated detailed in the following chapters.

Chapter 4

Enhancement of Triboelectric Nanogenerator Output Performance by Laser 3D-Surface Pattern Method for Energy Harvesting Application

4.1 Introduction

In this work, physical modification approach is considered for enhancing the recyclable triboelectric material properties. Hence, PA6 (Nylon-6) and PET (Polyethylene Terephthalate) were used as a triboelectric positive layer and negative layer for developing the TENG device. The continuous fibre laser was used to pattern the TENG substrate. Different patterns were formed on PET substrates using LSP. The laser patterned and pristine PET surface morphology was analysed by field emission scanning electron microscope. In addition, the changes in chemical modification of laser irradiated PET surface were investigated by Raman spectrometer. The voltage, current and charge of the TENG device were measured in contact and separation mode.

4.2 Governing equations:

Prior to the experimental investigations, we examined the TENG performance by theoretical simulation. The fundamental maxwell equations derived as follows:

$$\text{Gauss law } \nabla . D = \frac{\rho}{\varepsilon_0} \left(\frac{C}{m^3}\right) \text{ ..... } 4.1$$

$$D = \varepsilon E + P \text{ (in isotropic dielectric medium)}$$

$$\text{Gauss law } \nabla . B = 0 \text{ ..... } 4.2$$

$$\text{Faradays' law } \nabla \times E = -\frac{\partial B}{\partial t} \text{ ..... } 4.3$$

$$\text{Ampere's law } \nabla \times H = J + \frac{\partial D}{\partial t} \text{ .....} 4.4$$

Table 4.1 expressions of maxwell equations

Symbols		
E= Electric Field	ρ= Charge density	i = electric current
B= Magnetic Field	ε_0= Permittivity	J= Current density
D= Electric displacement	μ_0 = Permeability	c= speed of light
H= Magnetic filed strength	M= Magnetization	P= Polarization

where the displacement current, $\partial \boldsymbol{D}/\partial t$, was first introduced by Maxwell in 1861 to satisfy the continuity equation for electric charges. The electric displacement $\boldsymbol{D}$ is given by $\boldsymbol{D} = \varepsilon_0 \boldsymbol{E} + \boldsymbol{P}$, and for an isotropic dielectric medium, $\boldsymbol{P} = (\varepsilon-\varepsilon_0)*\boldsymbol{E}$, thus $\boldsymbol{D} = \varepsilon \boldsymbol{E}$.

4.2.1 V-Q-x relationship equation:

The general power generation theoretical equation for TENG is derived with the following parameters such as the voltage (V) between the two electrodes, the transferred charge (Q), and the separation distance (x) between the two triboelectric layers, which can be named the V–Q–x relationship. Two different categories of the triboelectric pairs are parted based on the material arrangements, such as dielectric-to-dielectric and conductor-to-dielectric types.

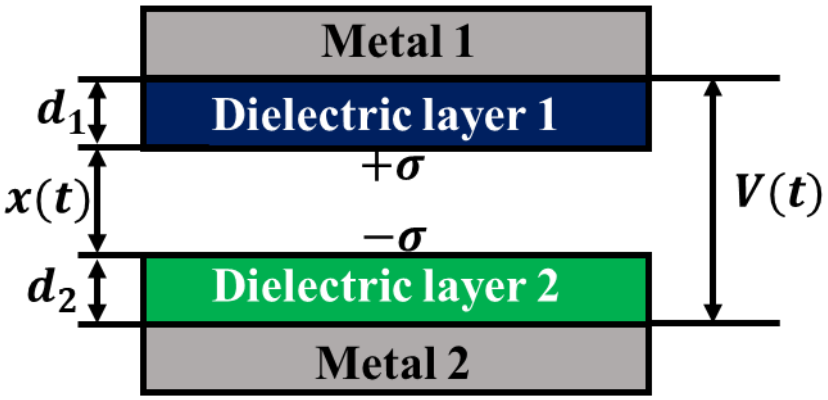

Figure 4.1 Schematic diagram of the fundamental dielectric to dielectric contact separation TENG mode

In this work, dielectric to dielectric contact and separation mode TENG has been built and shown in Figure 4.1. Both dielectric materials have dissimilar polarities in nature in which one layer is highly positive and

another one negative. When the external force is applied to the TENG device, the two different dielectric materials come into contact to form chemical bonds. The formation of chemical bonds helps to migrate the charge between two surfaces to equalize the electrochemical potential. Then the electron will flow from the top electrode to the dielectric surface to fill surface states with negligible decay. The electric field builds up during the separation or increasing distance (x) between each triboelectric surface and induces the potential difference (V). This potential difference drives the electron from top to bottom electrode, which results in a negative current with the external circuit. Once the device reaches the initial position, the surface charge distribution reverts to the equilibrium state. Subsequently, the device surfaces close to each other induce the reverse electrostatic field to bring back the electron from the bottom to the top electrode and attain the positive current.

From the Gaussian theorem, the strength of the electric field at each region is given as,

$$\text{Dielectric 1: } E_1 = -\frac{Q}{A\varepsilon_0\varepsilon_1} \quad \text{4.5}$$

$$\text{Dielectric 1 } E_2 = -\frac{Q}{A\varepsilon_0\varepsilon_2} \quad \text{4.6}$$

$$\text{The air gap } E_2 = -\frac{Q+\sigma x(t)}{A\varepsilon_0} \quad \text{4.7}$$

The voltage between the two electrodes can be given by

$$V = E_1 d_1 + E_2 d_2 + E_{air} x \quad \text{4.8}$$

At OC condition, there is no charge transfer, which means that Q is 0. Therefore, the open-circuit voltage V_{OC} is given by

$$V = \frac{Q}{A\varepsilon_0}\left(\frac{d_1}{\varepsilon_1} + \frac{d_2}{\varepsilon_2} + x(t)\right) + \frac{\sigma x(t)}{\varepsilon_0} \quad \text{4.9}$$

$$V_{OC} = \frac{\sigma x(t)}{\varepsilon_0} \quad \text{4.10}$$

At SC condition, V is 0. Therefore, the transferred charges are

$$Q_{SC} = \frac{S\sigma X(t)}{d_0 + x(t)} \ldots\ldots\ldots\ldots\ldots\ldots\ldots\ldots\ldots\ldots 4.11$$

$$I_{SC} = \frac{S\sigma d_0 V(t)}{(d_0 + x(t))^2} \ldots\ldots\ldots\ldots\ldots\ldots\ldots\ldots\ldots\ldots 4.12$$

Where $\boldsymbol{V_{oc}}$: open-circuit voltage, $\boldsymbol{\sigma}$: surface charge density, $\boldsymbol{x(t)}$: relative distance between two triboelectric layers, $\boldsymbol{\varepsilon_0}$: dielectric constant of air, $\boldsymbol{I_{sc}}$: short circuit current, **A**: area of the triboelectric layer, $\boldsymbol{v(t)}$: relative velocity of triboelectric layers, $\boldsymbol{d_0}$: Here d_1 and d_2 are the thickness of triboelectric layers 1 and 2, ε_1 and ε_2 are relative dielectric constants of triboelectric layers 1 and 2.

4.2.2 Theoretical simulation of the influence of surface modification on TENG:

Based on the Maxwell equation, the contact separation mode TENG was modeled and simulated in the COMSOL Multiphysics tool. 2-dimensional geometry was designed with the bottom and the top electrode of conductive materials stacked on the backside of the PA6 and PET dielectric surface (Figure 4.2), respectively. The TENG performance was analyzed by electrostatic physics with a stationary study. In addition, the surface charge density, floating potential, and ground boundary conditions are fixed for open-circuit voltage and short circuit current. The surface charge density values of PA6 and PET of 2.83 and -1.09 μC/m^2 has been chosen from the literature [141].

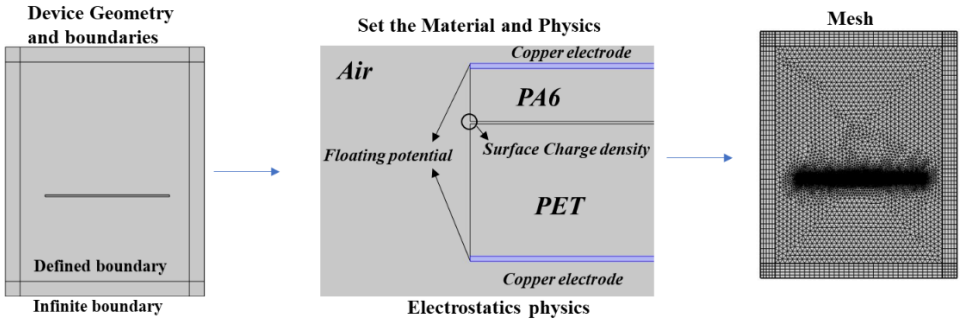

Figure 4.2 COMSOL simulation's 2D geometry and boundary conditions

Based on the V-Q-x relation equation, the generated electric potential and transferred charge between two electrodes has plotted in figure 2(a-c). When both dielectric layers contact, no output has generated. Figure 4.3(b) illustrates the electric potential of 55 V at 15 mm. But it was observed that the electric potential increases when the separation distance accomplishes the triboelectric theory. However, the transferred charge is almost identical after being separated from the bottom layer.

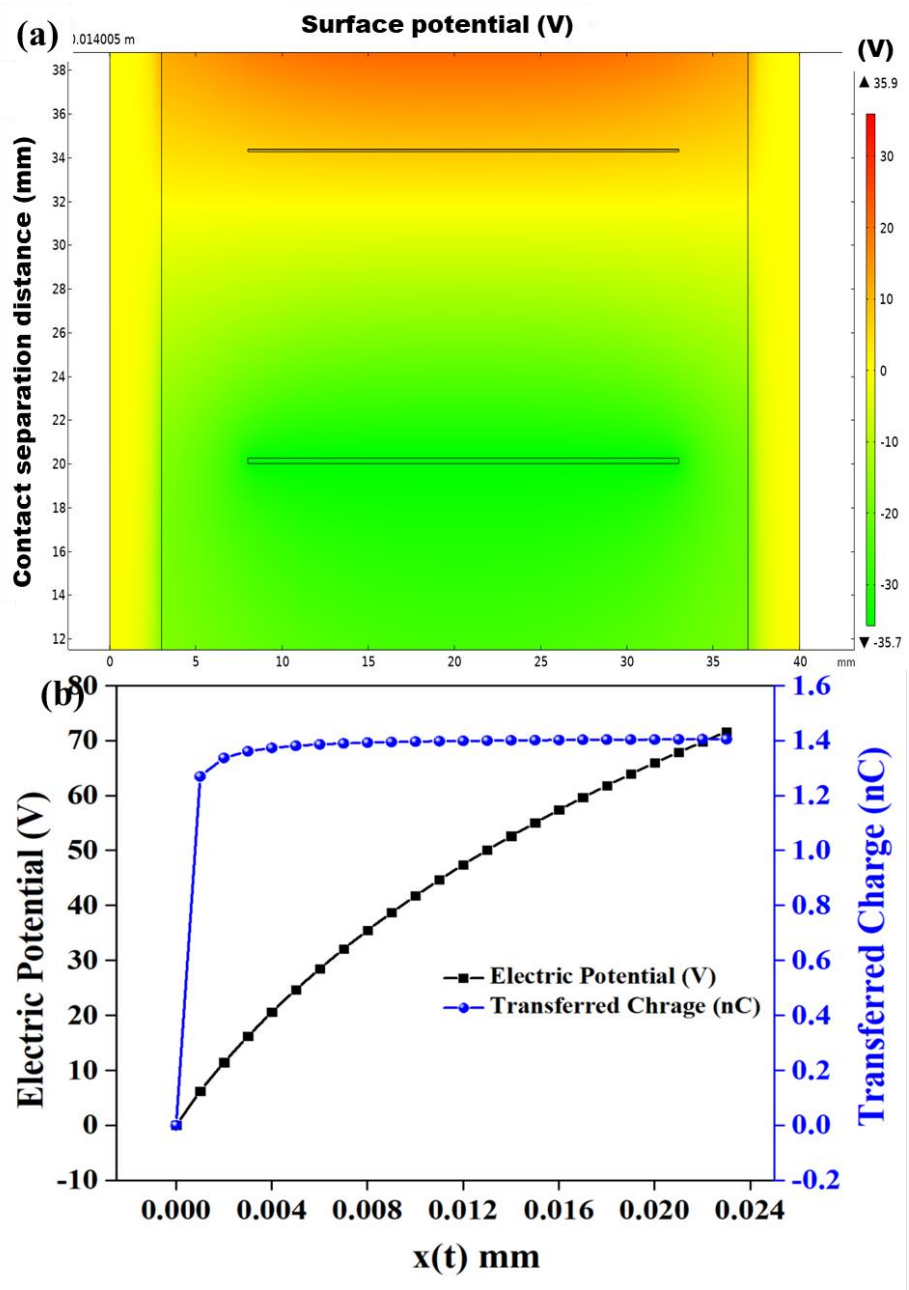

Figure 4.3 (a) TENG at both layers separated (b) electric potential and transferred charges versus separation distance

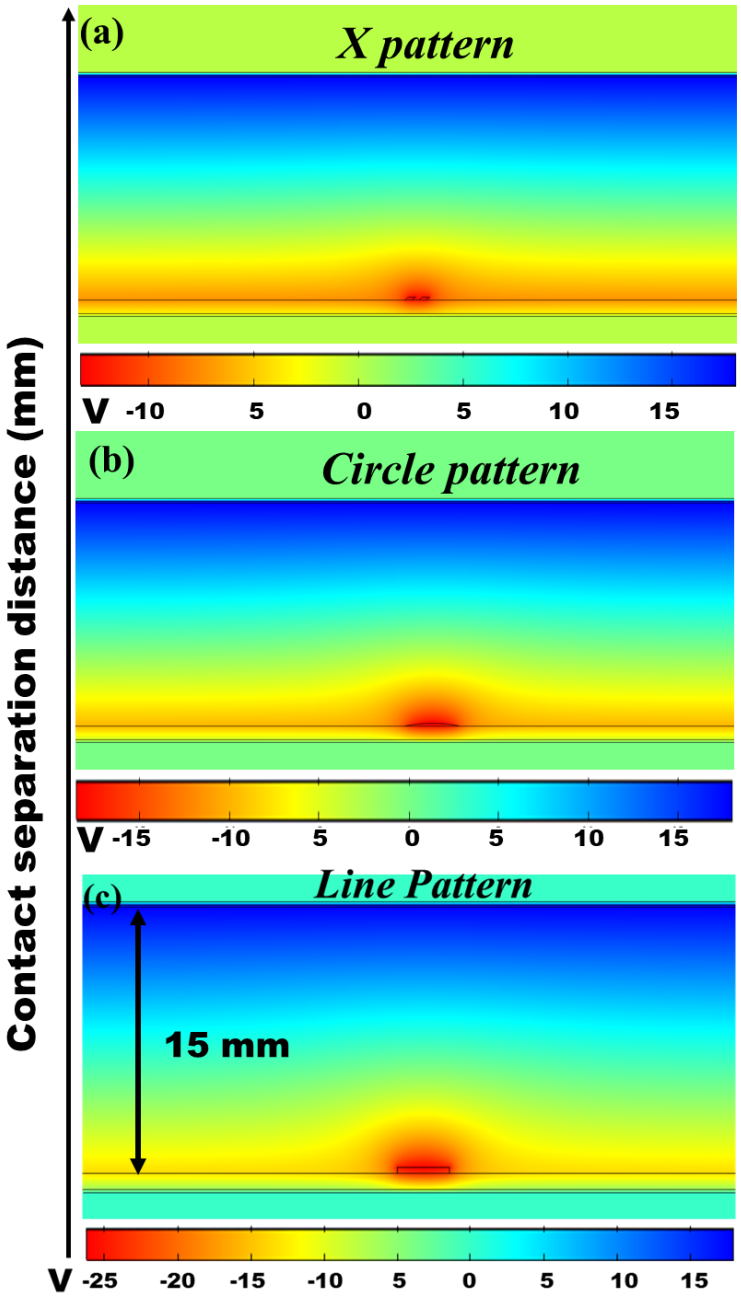

Figure 4.4 (a-c) electric potential of different patterns with the single cross-section

Further improving TENG performance, the physical surface modification method has been introduced in the model. For the preliminary evolution, the simulation was done using a single cross-section with X, circle, and line patterns to examine the characteristics of distinct pattern influences. The decreased surface contact area causes a considerable loss in output performance for the X and circle patterns. When compared to pristine TENG, the line pattern TENG output voltage

(-26.5 to 17.9 V) has substantially improved. As a result, the increased surface area of the surface-modified TENG device demonstrates that it has improved surface charge transfer. The frictional surface contact area of the plain and varied pattern surfaces may be calculated using either a mathematical formula or AutoCAD. The pristine and patterned surface area is measured in the AutoCAD platform to ensure accuracy.

Hence, all the pattern parameters (length, height, and diameter) for the AutoCAD modelling were obtained from the FESEM images. The calculated frictional surface area is highlighted with the red colour box in the snipped AutoCAD image which shown in Figure 4.5. It observed that the plain substrate has an 1830 mm^2 surface area, and the patterned surface (X-1849.93 mm^2, Circle-1867.38 mm^2, Line-1888.68 mm^2) has obtained a higher surface area compared to pristine.

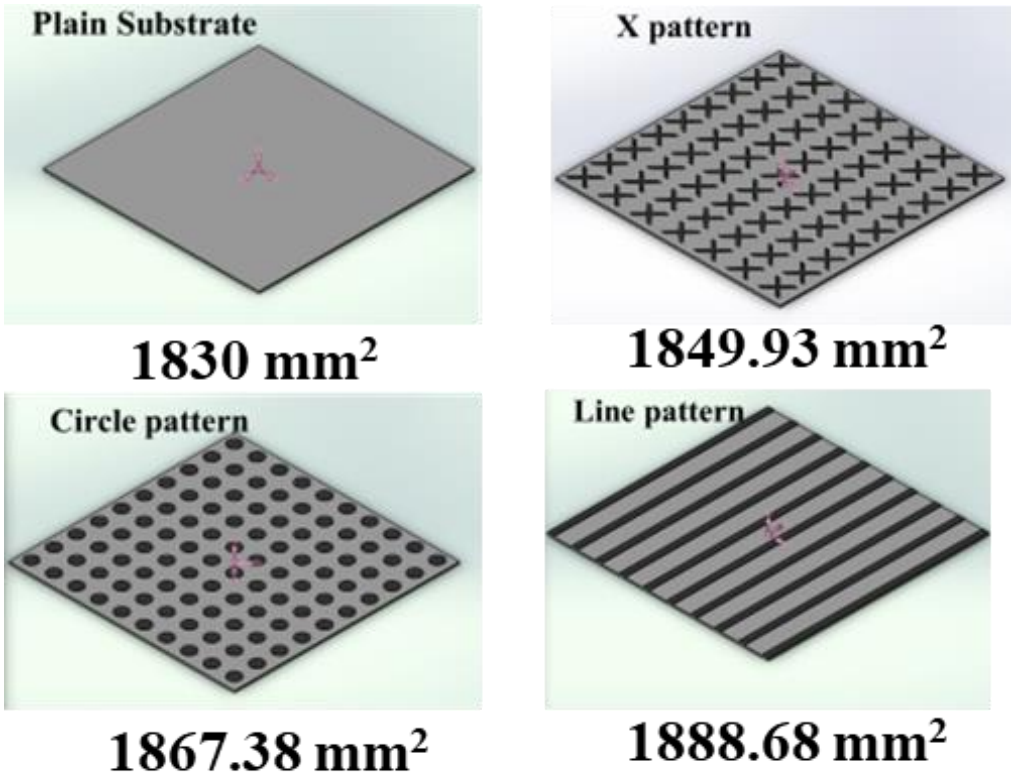

Figure 4.5 frictional surface contact area measurement for different patterns by AutoCAD tool

Further evaluation, the complete line pattern structure (10×1 array) was modeled in COMSOL tool (Figure 4.6) and investigated the triboelectric

response. Similar to the previous study, there is no generation when two layers are in contact. When the top layer moves upward, the electrostatic induction takes place and generates higher electric potential and transferred charge compared to the plain, which is due to enhanced surface contact area by the surface modification method. In addition, it noticed that increasing separation distance $\boldsymbol{x(t)}$ gradually increases the electrical potential.

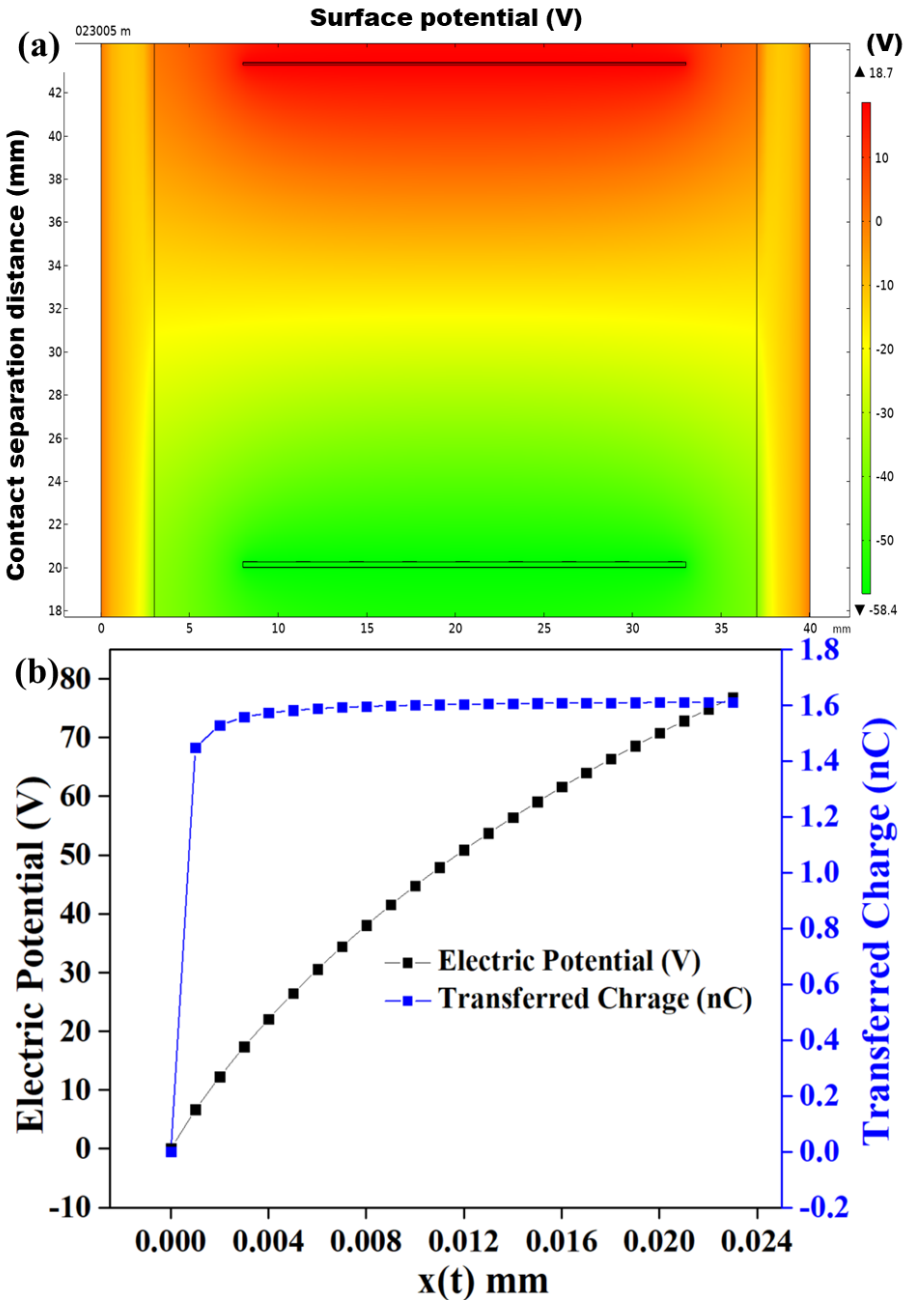

Figure 4.6 (a)-(b) electric potential and transferred charge of line patterned TENG

4.3 Experimental Section

4.3.1 Laser process and influences of laser parameters:

In this work, a Ytterbium (Yb) doped fiber laser of wavelength 1064 nm was used in continuous wave (CW) mode for laser surface patterning (LSP) on the PET substrate. A galvo scanner head controls this CW laser beam with two 3-axis mirrors that deliver a high-speed beam with a smaller spot size over a large field of view. Depending upon the pattern profile, the laser focal area will vary. For example, if the single line pattern has a length of 30 mm and width of 0.8 mm, the resulting focal area (30 mm length and 0.8 mm width) was 24 mm^2.

Laser power is a crucial parameter in physical modification and improving TENG performance. So, it must be optimized. Also, the laser machine can tune the power from 5 to 50 W with a 5 W interval and fixed passes. For primary optimization, the line pattern was textured on the PET surface and measured TENG performance for parameter optimization. The laser power was optimized depending on TENG output (Figure 4.7). It was noticed that up to 15 W, no surface modifications were seen on the PET surface. Because PET is a transparent sheet, it takes more energy to heat its surface. The color and shape of the surface began to change on the 20 W laser, although it simply produces discontinued patterns. A consistent line pattern formed at 25 W due to the photophysical mechanism. On the other hand, the device has not yielded the TENG output owing to the tiny thickness of the line pattern. The maximum TENG output has been obtained at 30 W laser power. Further increasing the laser power takes place poor mechanical strength and reduces the surface polarization. Therefore, the 30 W laser power is the optimized parameter and is followed for further experiments in this chapter.

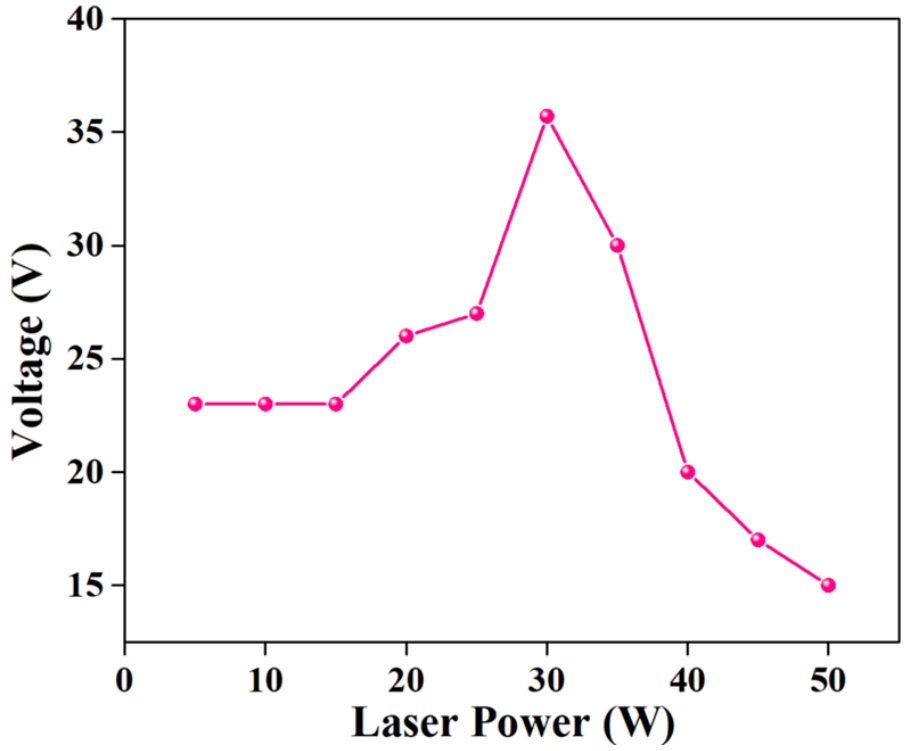

Figure 4.7 The line pattern TENG electric potential concerning varying laser power

4.3.2 Details of Laser surface patterning (LSP):

LSP process was employed on 3 × 3 cm^2 polyethylene terephthalate (PET, Bayer Material Science) for developing different structures such as circles, lines, and X patterns. The circle and X patterns were textured in 10×10 and 9×7 arrays. The pattern scale details are shown in Table 4.2, and the schematic diagram of the laser focal area is shown in Figure 4.8. The different patterns were modelled in the solid works platform and imported into the laser system. The system will convert the model into G codes and guide the laser beam for texturing the PET substrate. The schematic of the LSP process is shown in Figure 4.9 (a), and the laser parameters are shown in Table 4.2. Figure 4.9 (b) illustrate the digital colour image of LSP PET substrate with and without back electrode. The focused laser beam has melted the surface and formed the desired pattern (Figure 4.8(b)). The time required for the laser processing of each sample is around 6 min.

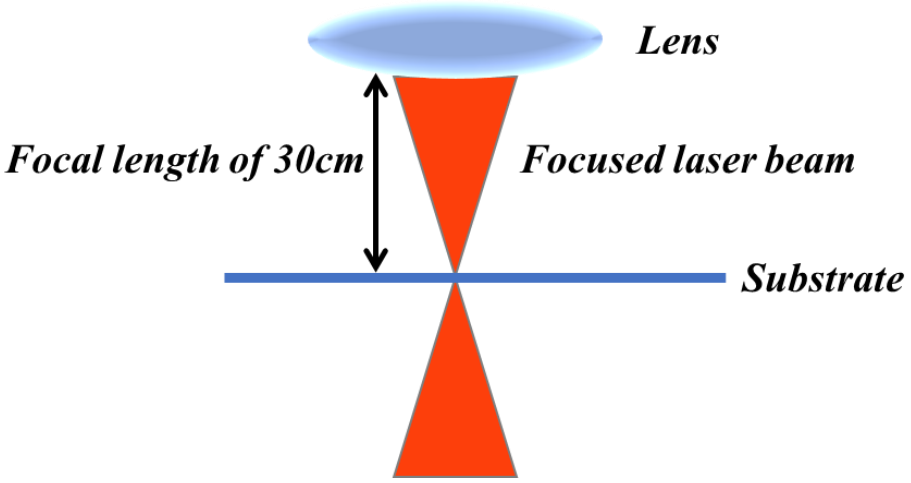

Figure 4.8 schematic diagram of laser focal area for laser texturing

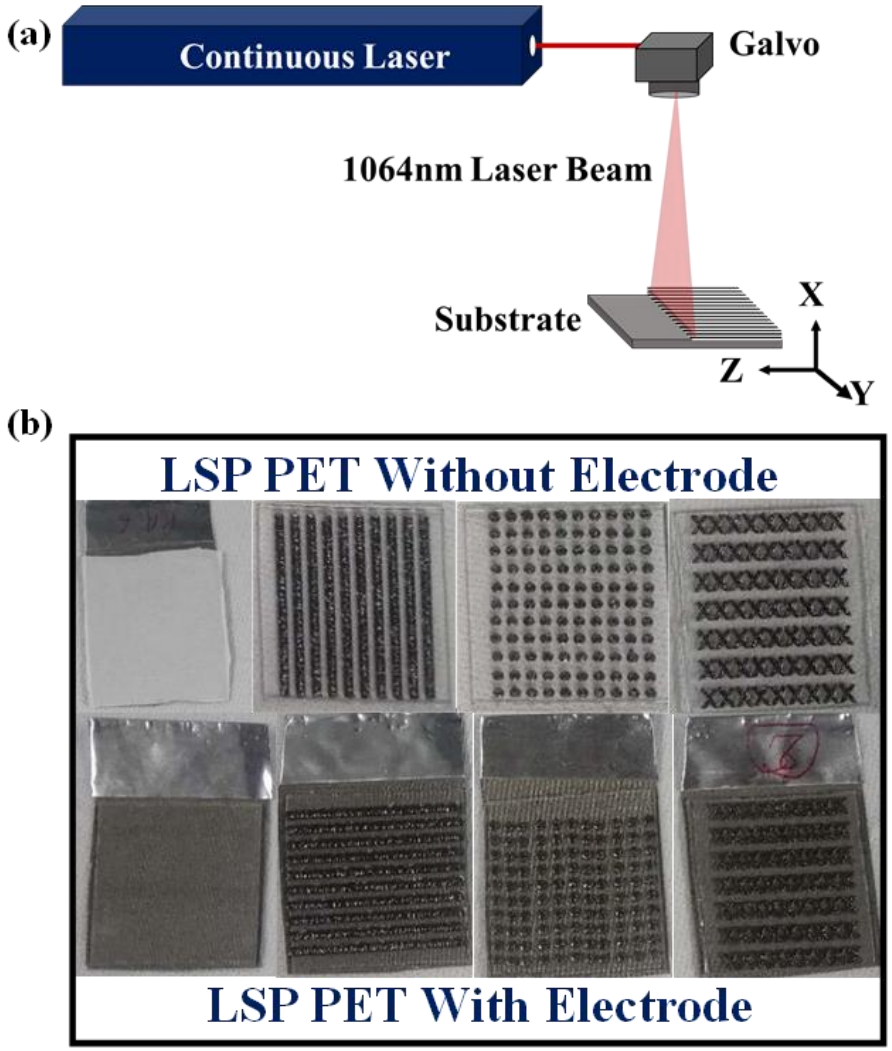

Figure 4.9 (a) Schematic diagram of the laser patterning process by continuous wave laser (b) LSP PET with and without electrode

Table 4.2. Laser parameters for LSP on PET substrate

Laser parameters		Pattern	Size of the pattern (mm)
Power	30 W	Pristine	30*30(L*W)
Laser scanning speed	1.5 mm/s	X	3.315*0.09 (Diagonal length *t)
No of laser passes	1	Circle	1.6*0.09 (dia. *t)
Laser focal length	30 cm	Line	30*0.8*0.09 (L*W*t)

4.3.3 TENG device construction and characterization:

The substrates were cleaned consecutively with isopropanol and de-ionized (DI) water for 5 minutes. Afterward, the adhesive conductive textile tape (CTT) and antistatic tape (AST) were pasted on the backside of the PET surface. On the other hand, the parallel PET surface was pasted with PA6 (Nylon6) and CTT, as shown in Figure 4.10. Finally, the TENG device was fabricated using PET negative triboelectric layer, highly positive PA6 triboelectric layers and CTT conductive electrode [142-144]. The as-prepared tribo-layers have been arranged parallelly with respect to vertical contact and separation mechanism.

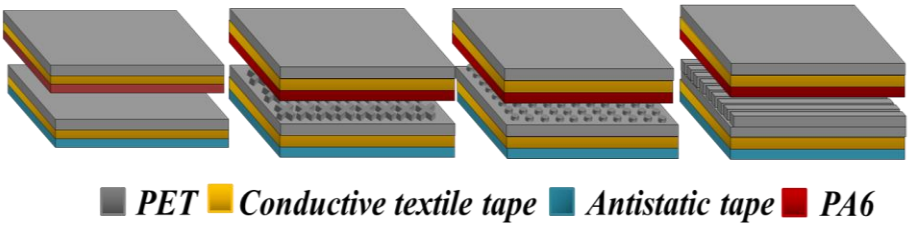

Figure 4.10 schematics of device construction

The surface morphology and protrusion size of the substrate were measured by field emission scanning electron microscope (FE-SEM, Carl Zeiss sigma Supra-55). The pristine and patterned PET surface was investigated by Raman spectra between 1500 to 1800 cm−1 wavenumbers, with an excitation wavelength of 514 nm (LabRAM HR Evolution; Horiba, Japan). A dynamic fatigue failure system (Popwil Model YPS-1) was used to investigate the TENGs by frequency, contact separation distance, and mechanical force of two tribo-layers of different

materials. The current generated from the TENG devices was measured by Femto/Pico ammeter (B2981A).

4.4 Result and Discussion

Surface morphological analysis:

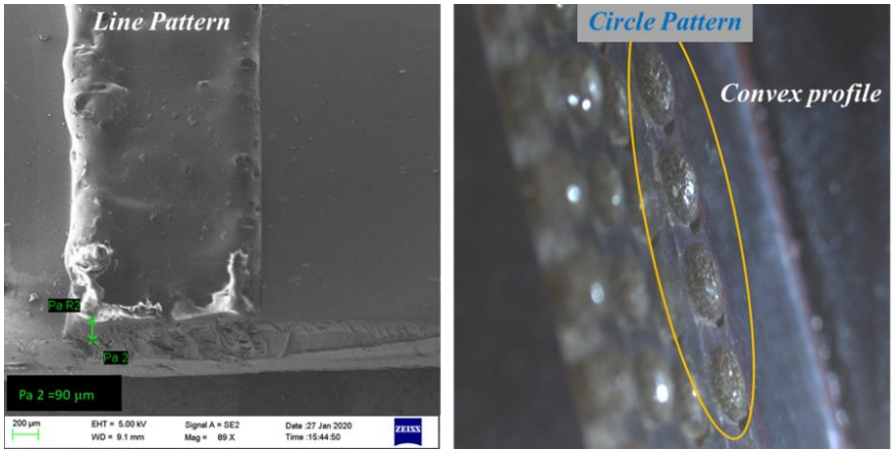

Figure 4.11 the convex(protrusion) profile of line and circle pattern

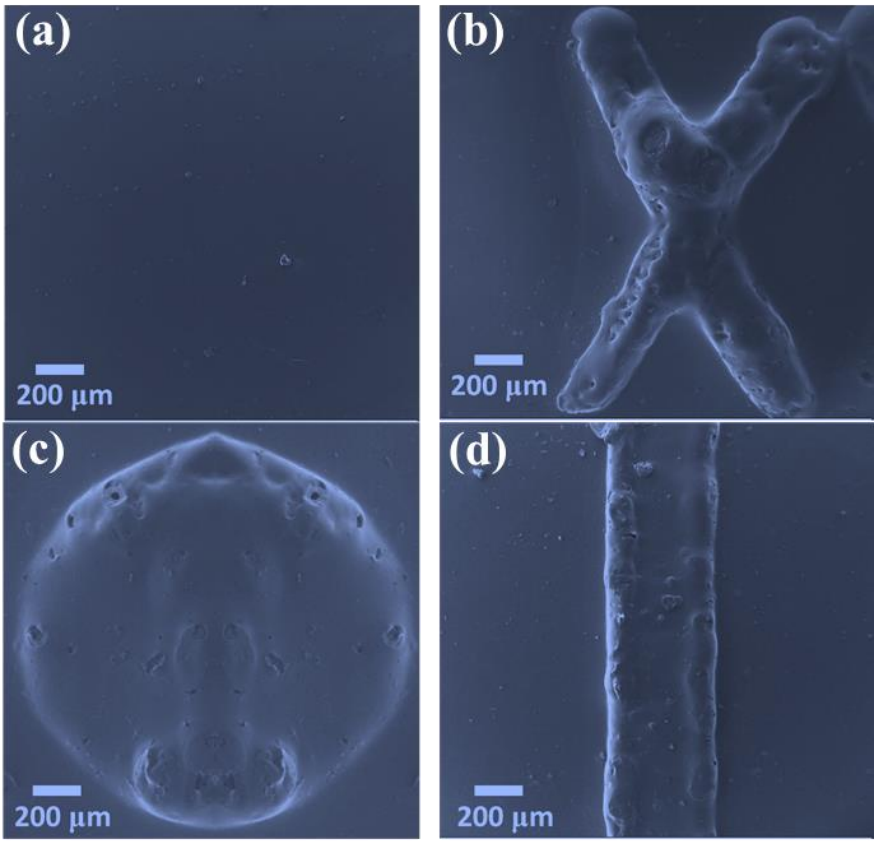

Figure 4.12 (a) FESEM images of Pristine PET substrate (b) X pattern (c) Circle pattern and (d) line pattern

The morphology and pattern dimensions of the PET substrates have been investigated using FE-SEM. Figure 4.12 (a) shows the pristine PET having a smooth surface without any irregularities. The laser irradiation triggers a photophysical mechanism on the surface and leads to the melting and breaking of chemical bonds [107,108]. When the laser irradiation is cut off, rapid solidification of the molten material occurs and leads to the formation of a protrusion pattern shown in Figure 4.11. Figure 4.11(b-d) shows the well-defined and consistent micro pattern developed on the PET substrate.

4.4.1 Investigation of LSP influence in chemical modification:

To evaluate the chemical modification, the pristine and patterned PET surface was investigated by Raman spectroscopic analysis as shown in Figure 4.13(a). The patterned and pristine PET chemical bond changes were assigned to ring mode 8a (in Wilson's notation) at 1615 cm-1. The stretching vibration of C=O bonds and carboxylic acid group formation were confirmed and attributed to 1726 cm-1 [145]. In particular, the patterned PET substrate peaks degradation and shifting towards higher wavenumber confirms the rearrangement of the polymer chain and photochemical degradation. The surplus carboxyl groups condensed with hydroxyl group reduces the peak intensity. Also, this peak degradation attributes to the formation of amorphous carbon upon laser irradiation. This amorphous carbon weakening carboxyl group that leads to degrades the TENG performance. After the laser treatment, the carboxyl group surface energy is higher in line patterned compared to pristine and other patterns, resulting as an increased TENG performance [146,147].

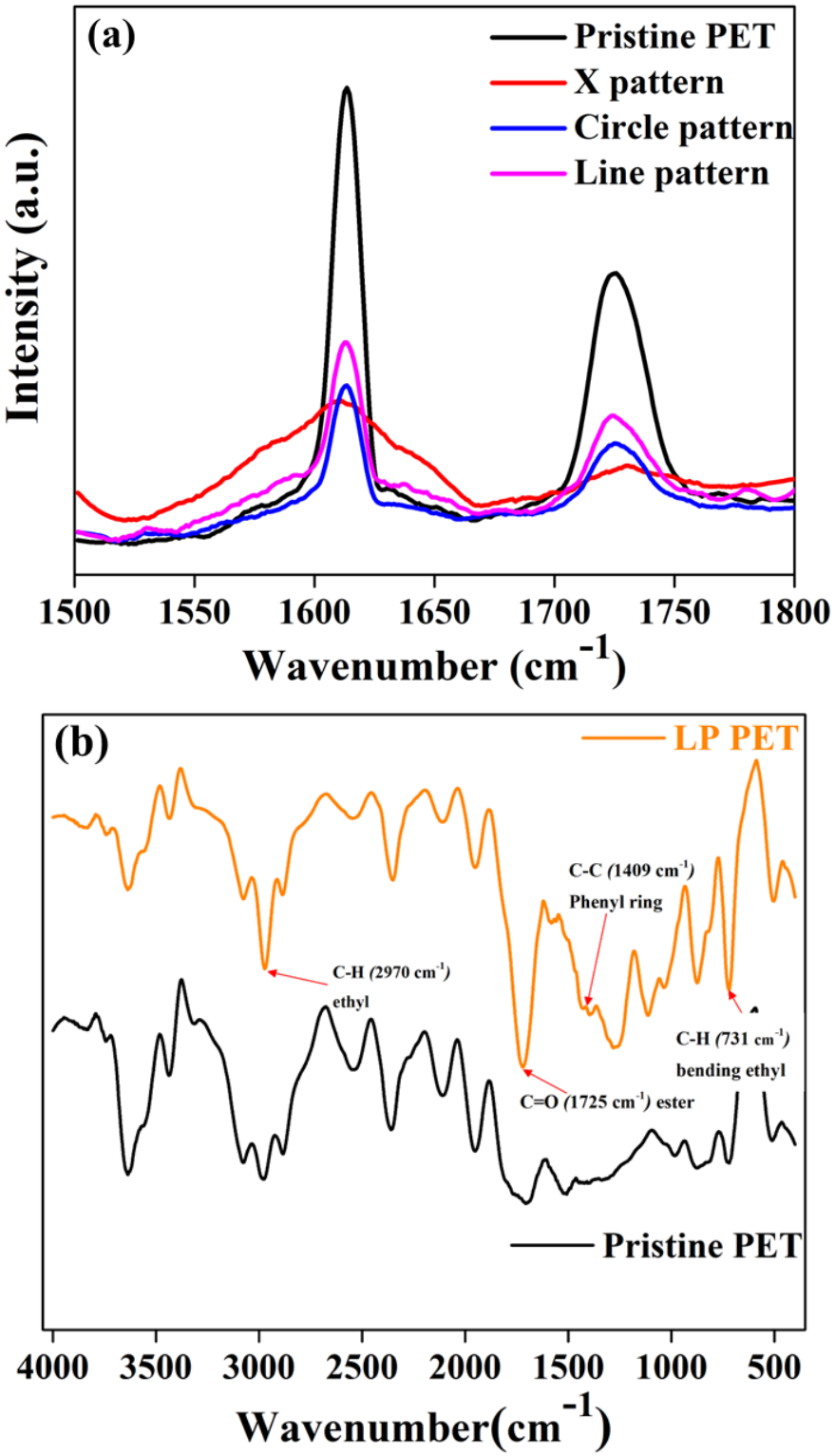

Figure 4.13 (a) Raman spectroscopy analysis of Pristine and laser patterned PET surface (b) FTIR transmittance spectrum of pristine PET and laser patterned PET substrate

The intermolecular interaction in the chemically modified LP PET and bare PET were analysed by FTIR and shown in Figure 4.13(b). There

are four functional groups in the bare PET film: two esters, an aromatic ring, and an ethyl group. The terephthalate group is formed by combining the aromatic and two esters groups, and it contains different bonds such as C–C, C–H, C–O, C=O, and aromatic rings (Table 4.3). It was observed that laser-induced photophysical modification sharpened the ethyl and ester group peaks in the LP PET sample. Furthermore, at 1725 cm^{-1}, the significant stretching vibration of C=O was detected. Also, the strong and mild bending ethyl groups both showed up at 2970 and 731 cm^{-1}, respectively. The transmittance intensity of the ethyl group increased due to a reduction in the concentration and oxygen may be expelled from the band which oxidizes the surface that improves the wettability and surface polarity [148]. Another reason for increases in intensity might be the thermal breakdown of PET chains and photo crosslinking between neighbouring chains [141].

Table 4.3: Bands associated with LP PET from FTIR and Raman

Wave number(cm-1)			**Band configuration**
Raman	LP PET	1726 cm^{-1}	carboxylic acid group and C=O
	PEO	1479, 1281 cm^{-1}	CH_2 group
FTIR	LP PET	2970 cm^{-1}	C–H ethyl
		1725 cm^{-1}	C=O ester
		1409 cm^{-1}	C–C Phenyl ring
		731 cm^{-1}	C–H bending ethyl

4.4.2 Triboelectric characterization:

The electrical output performance was analysed for different patterned and pristine TENG by the contact separation mechanism. Figure 4.14(a) and (b) illustrate the open circuit (OC) voltage and short circuit (SC) current of the TENG devices.

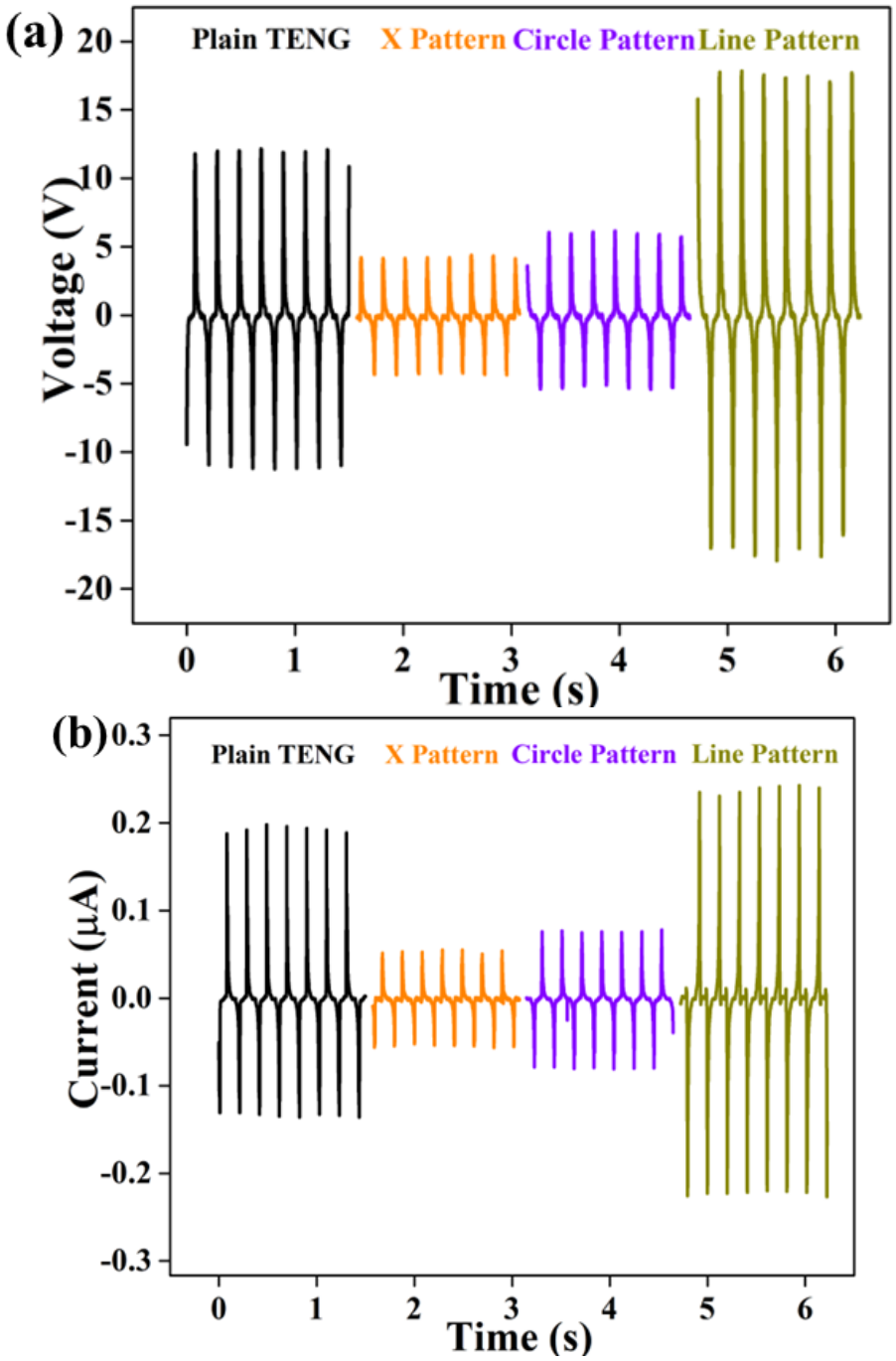

Figure 4.14(a) and (b) OC Voltage and SC current measurement of various patterned and pristine TENG devices; the contact separation distance, frequency and load were fixed at 4 mm, 5 Hz and 50 N

Initially, the TENG device was examined with the constant external load of 50 N, the distance between the dielectrics of 4 mm and the frequency of 5 Hz. It exhibits the peak-to-peak OC voltage and SC current of 23 V and 0.33 μA respectively. The patterned TENG device exhibited

considerable enhancement in the output performance due to the higher surface contact area between them. Notably, the line patterned TENG device has attained a higher peak to peak voltage and current values of 35.7 V and 0.46 μA as shown in Figure 4.14(a and b). The circle and X patterned TENG device output performance was degraded as compared to the pristine TENG due to the effect of the high aspect ratio of micro patterns [149,150]. When the contact surface is too large the electrostatic induction and contact electrification weakened and degrades output performance [150]. The X and circle pattern edges and top surfaces have protruded with non-homogeneous structures which reduces the contact between pristine PA6 and patterned PET. The top surface non-homogeneous protrusion was clearly visible in the FESEM images. The performance pristine and patterned TENG devices are tabulated in Table 5.1.

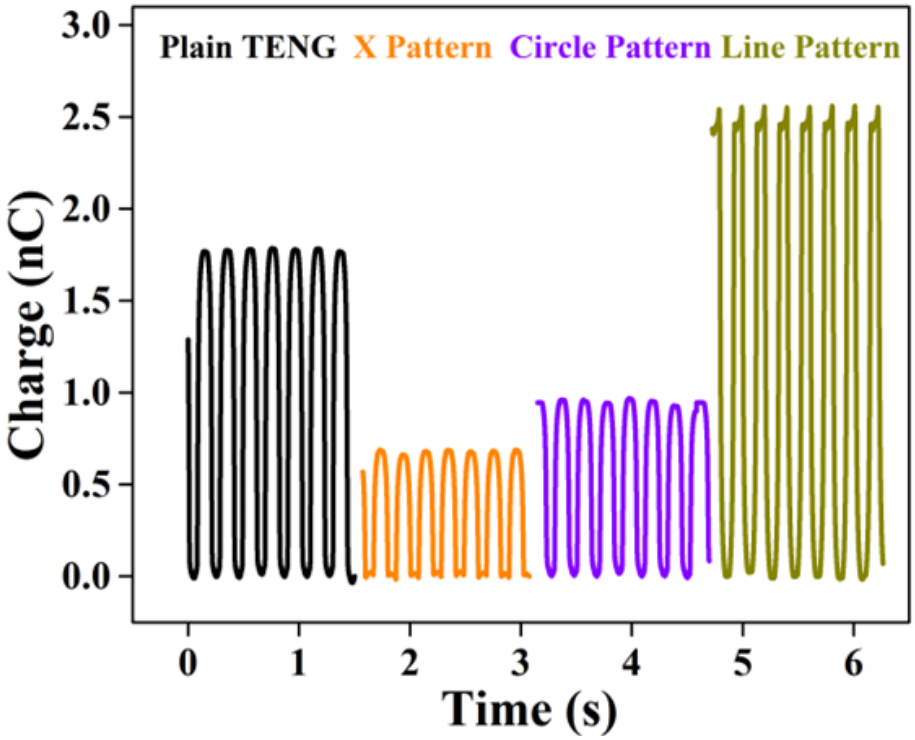

Figure 4.15 short circuit transferred charges of pristine and patterned TENG device

Furthermore, the transferred charges were measured from TENG devices while two triboelectric layers separated from each other as shown in Figure 4.15. The pristine TENG device has transferred a charge of 1.6 nC. However, the charge transfer in the X and circle

patterned TENG device significantly reduced to 0.6 and 0.9 nC respectively which could be attributed to the low surface contact area interaction. In case of the line pattered TENG device, more charges (2.5 nC) have transferred compared to other patterns. The surface area of pristine and patterned PET calculation is shown in Figure 4.5. This enhancement of charge transfer is due to the higher interaction of surface contact area in between line patterned PET and plain PA6 surfaces. The electric potential and transferred charge results from the experiment are consistent with the theoretical simulated line-patterned TENG's. Hence, the line patterned TENG device was selected for further investigation.

4.4.3 Influence of mechanical parameter in line pattern TENG:

It is essential to investigate the device performance in the real-time condition such as varying mechanical load, frequency, the distance between two dielectric layers, and load resistance. Figure 4.16(a) illustrate the SC current analysis of line pattern TENG by varying separation distance from 1 mm to 12 mm with a fixed load of 50 N and a frequency of 5 Hz. The electrical output performance has increased substantially with an increase in the separation distance and then saturates slowly. The closer distance (2 mm) has generated a lower SC current (0.4 μA) due to the low electric field and low charge built up. The noteworthy enhancement in SC current (1.1 μA) at a higher separation distance (12 mm) was attained. This is due to an increment in the induced contact electrification that contributes to increased charge flow in the external circuit. In addition, the higher separation distance increases the relative contact velocity of the two triboelectric layers, which helps in faster electron transfer between them [151,152].

Figure 4.16(b) illustrates the SC current of the line pattern TENG device at frequencies from 1-5 Hz. At 1 Hz frequency, the device exhibits less than 0.1 μA of current, but a significant improvement has been attained in the current values of 0.23 μA at 5 Hz. It was noticed that beyond this frequency, no changes in current values were observed. This is due to higher deformation at 5 Hz frequency and results in a higher flow rate

of charges [153,150,154]. Also, this frequency assisted in increasing the number of tapping within less time span and eventually increased the charge transfer rate in a shorter time.

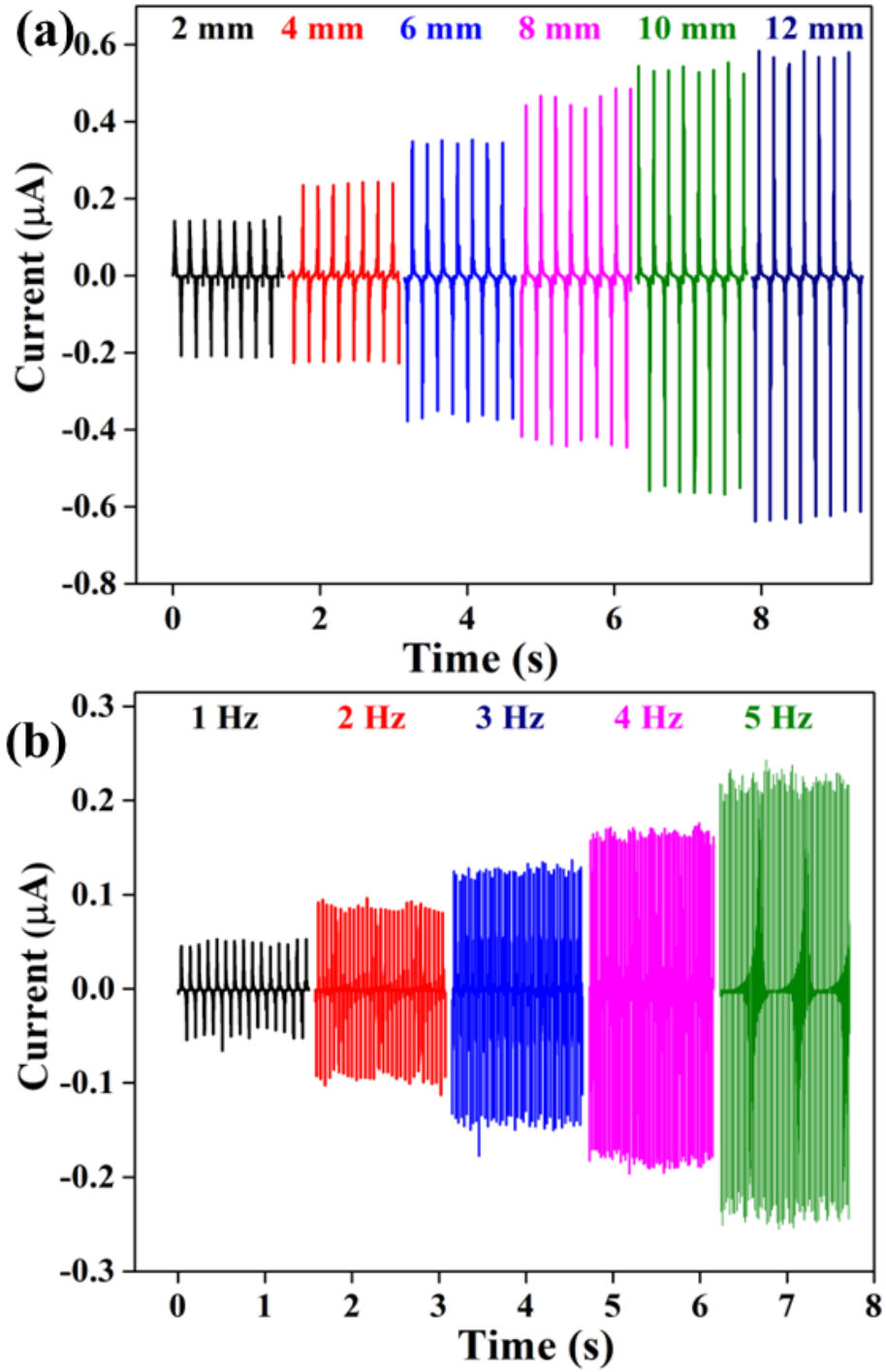

Figure 4.16 (a) the SC current analysis based on contact and separation distance was investigated under the load of 50 N and the frequency of 5 Hz. (b) the various frequency-based analysis for line patterned TENG with a fixed load of 50 N and contact separation distance of 4 mm

The external force is an essential factor influencing the induced charge densities and is primarily concerned with the contact area. Therefore, the line patterned TENG device was demonstrated with various mechanical forces between 10-100 N with an interval of 25 N, as illustrated in Figure 4.17.

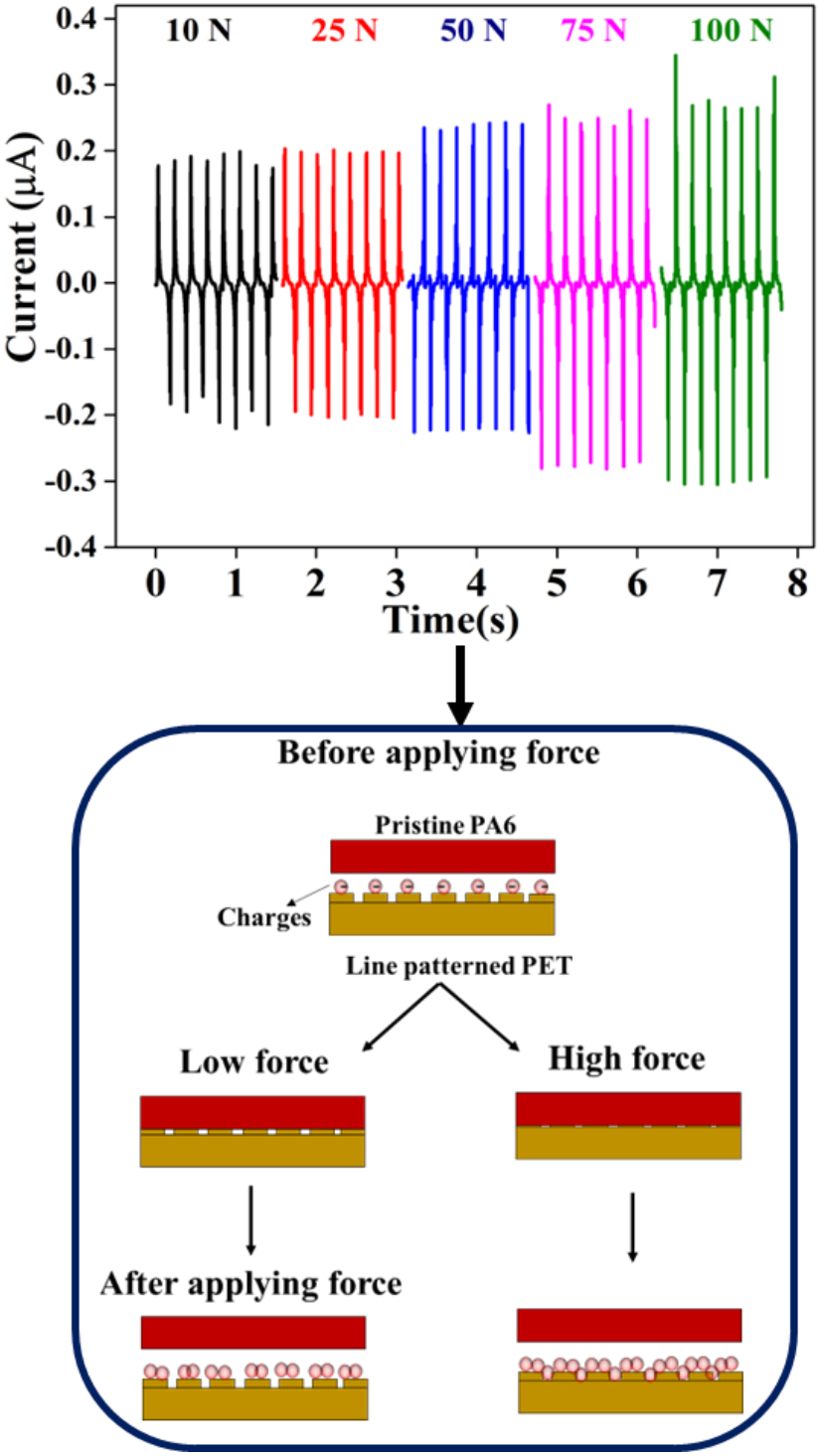

Figure 4.17 different external load-based analysis was kept the movement frequency of 5 Hz and separation distance of 4 mm

The lower SC current (0.36 μA) was attained at 10 N. At 100 N force, a noticeable improvement in the SC current of 0.56 μA was achieved. The protrusion structure has deformed during the higher contact force to fill more gaps between the line patterned PET surface and pristine PA6 surface and eventually increases the surface contact area [150,155,156]. It is due to the elastic nature of triboelectric layers that fill more spaces and induces more charges (schematically illustrated in Figure 4.17) [154-157]. Hence higher contact force enhances electrostatic induction and triboelectrification.

4.4.4 Endurance of the line patterned TENG:

The line patterned TENG device was developed for harvesting mechanical energy with rigorous load and frequency conditions.

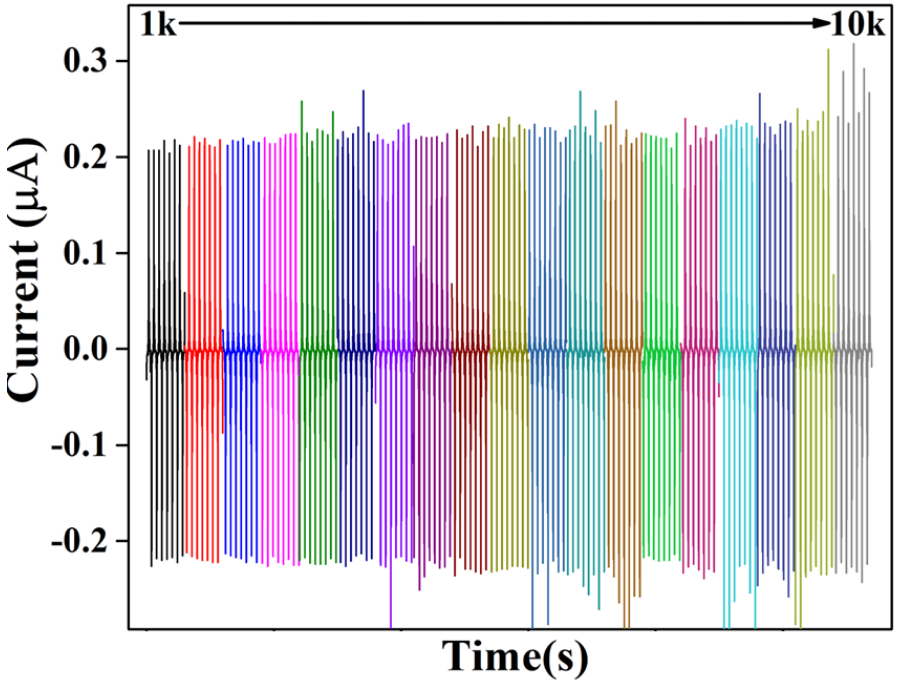

Figure 4.18 mechanical endurance analysis of line patterned TENG device functioning with 10000 cycles

Therefore, it is essential to investigate the stability and reliability of the TENG device. The final device was demonstrated for a 10000-life cycle at a constant load of 50 N, frequency of 5 Hz, and separation distance of 4 mm. Figure 4.18 shows the mechanical endurance of line patterned TENG device up to 10000 cycles. In the graph, the last five cycles of every 500 cycles starting from the 996th cycle have been plotted (996-

1000, 1496-1500…). There is no significant attenuation in SC current throughout the 10000 cycles, which confirms the better mechanical endurance of the patterned TENG device.

However, few sharp positive peak rises in the output response were observed. These abrupt charging can be attributed to the localized strain. Under time-dependent stress, localized deformation can take place due to a property of material known as creep [158, 159]. These changes are temporary, i.e., the material might deform elastically, and no permanent change is observed in the material properties. After 10 k cycles, we re-run the experiments and found that the device (after a brief pause to reset the machine properties) output returned to normalcy.

Similarly, this device was systematically investigated to govern the load resistance to attain maximum power output. Also, the influence of external load resistance was investigated with SC current drop and maximum output power density.

The output power density was estimated from equation 13

$$P = \frac{I^2 R}{A} \quad \text{..... 4.13}$$

Where I stand for current, R is the load resistance and A is the contact surface area.

The load resistance with RMS voltage and SC current relationship is depicted in Figure 4.18(a). The load resistance is proportional to the potential difference and inversely proportional to the SC current. Therefore, when increasing the load resistance, the RMS voltage has notably increased up to 10 MΩ and then gets saturated. However, the SC current was decreased due to less current flow at higher load resistance. Similarly, Figure 4.18(b) shows the SC current and power density across the load resistance of the line patterned TENG device. The load resistance varied from 1 kΩ to 4 GΩ for power density and SC current. The output performance was stable at one kΩ to 10 MΩ and beyond which the SC current has degraded slowly due to higher resistance restricting the current flow. However, the power density has improved substantially at 100 MΩ of 0.8 μW/cm^2.

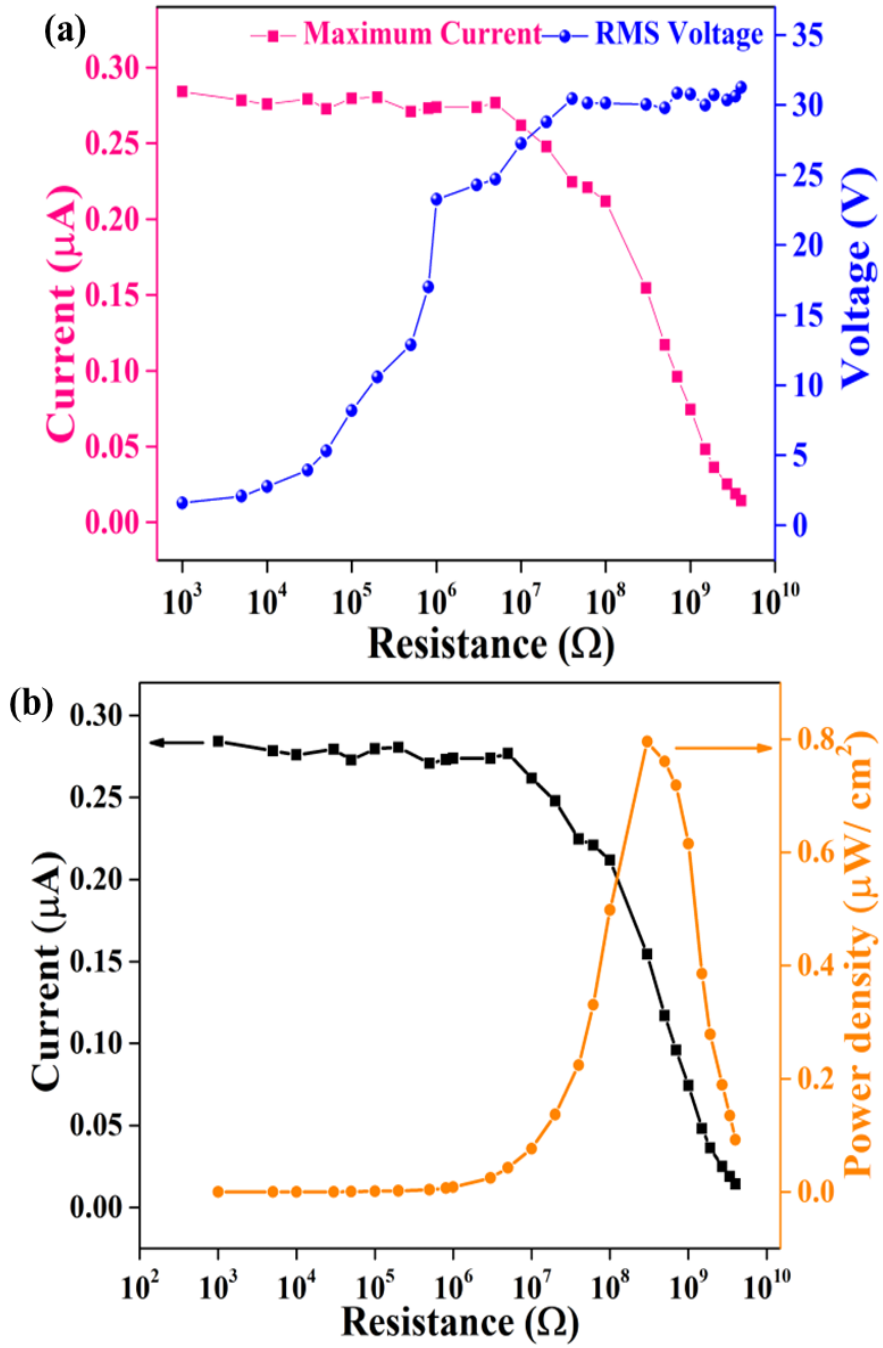

Figure 4.19 (a) Power density measurement with respect to the different load resistance. (d) RMS voltage across the different load resistance (1 KΩ to 4 GΩ)

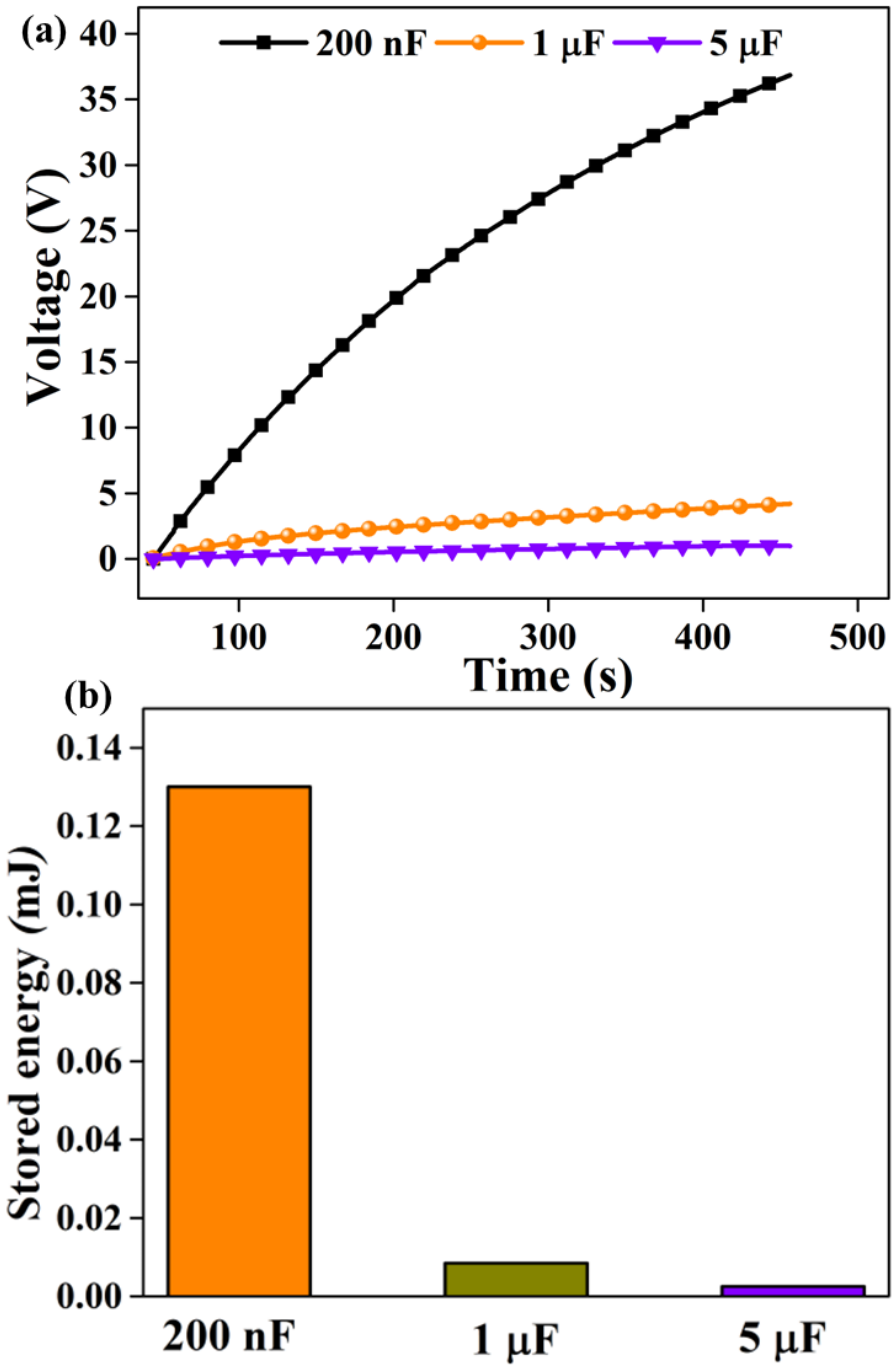

Figure 4.20 (a) The line patterned TENG device-generated voltage stored with different capacitor (b) maximum stored energy with 200 nF, 1 µF and 5 µF capacitor

Furthermore, to investigate the storage capability, the as-generated electrical energy was stored in three (200 nF, 1 µF, 5 µF) different commercial capacitors with a duration of 425 sec (Figure 4.20(a)). It was affirmed that the device could charge a maximum voltage of 36 V with a small capacitance of 200 nF. The maximum energy (0.13 mJ) was

stored in a 200 nF capacitor for a short time span (Figure 4.20(b)), and the stored energy was discharged quickly. The increase in the capacitance range increases the charging and discharging time of the device.

4.4.5 Device demonstration:

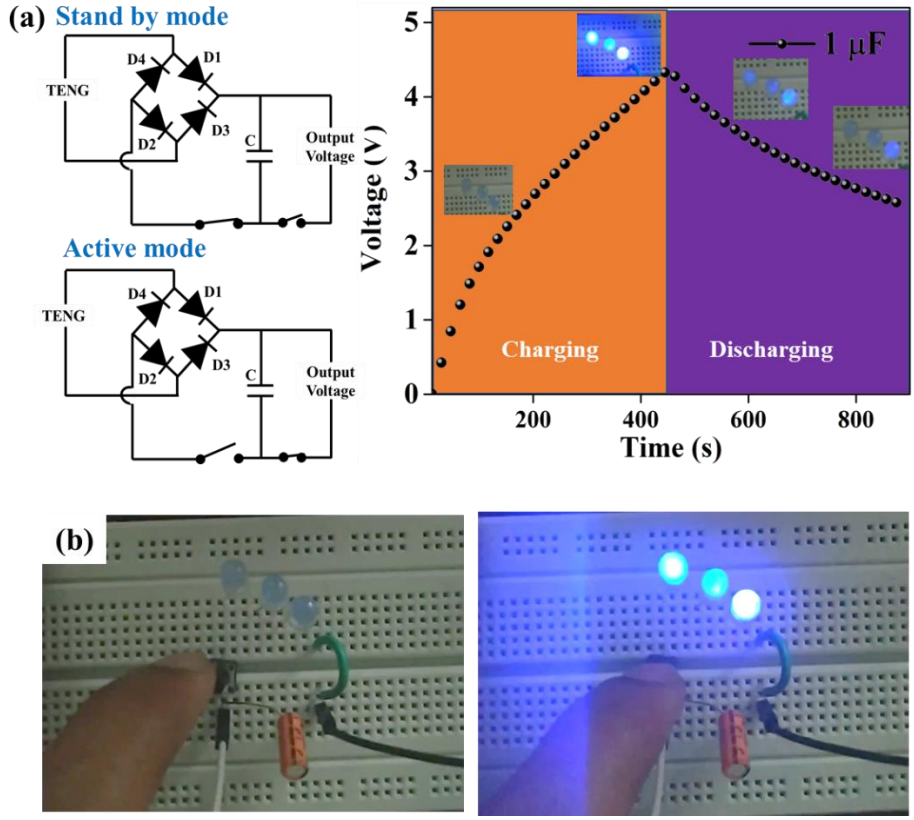

Figure 4.21 (a) Charging circuit and 1 µF capacitor charged 425 sec and then discharged slowly (b) digital images of three blue LEDs lighting up with 1 µF capacitor energy

Figure 4.21(a)&(b) depicts the charging and discharging of generated energy with a 1 µF capacitor and LEDs lighting. The charging circuit (Figure 4.21(a)) was demonstrated with the different commercial capacitors for charging and discharging the power. The 1 µF capacitor took more time to charge at about 4.6 V, and the stored energy was discharged very slowly. Initially, the LEDs (inset picture Figure 4.21(b)) were glowing at a higher intensity. However, the light intensity has dimmed gradually over a period of time due to energy discharging from

the capacitor. Hence, we proposed that this power be used to operate the low-power electronic device.

4.5 Summary

- The theoretical simulation (COMSOL Multiphysics) also confirms that the higher surface contact area contributes to the effective output performance TENG device.
- The continuous-wave laser was proposed to develop the micro patterns on triboelectric layers. The laser texturing has been demonstrated for three different micro patterns such as circle, line, and X pattern, and enhanced the surface contact area of the TENG.
- The electrical characteristics of pristine and patterned TENG devices were investigated thoroughly based on varying mechanical load (10-100 N), separation distance (2-12 mm), frequency (1-5 Hz), and load resistance (1000-4000 MΩ).
- From the optimized parameter (50 N, 4mm, and 5 Hz), the pristine TENG has generated OC voltage and SC current of 23 V and 0.33 μA, respectively. The line patterned TENG device has notably enhanced the peak-to-peak OC voltage and SC current to 36 V and 0.46 μA, respectively, compared to other patterns. The maximum power density (0.8 $\mu W/cm^2$) was attained at 100 MΩ load resistance.
- The energy generated by the TENG can power up to three LEDs at maximum intensity. The line patterned TENG device has shown stable output performance for 10000 cycles without negligible loss. The obtained results could be used for powering the micro/Nano system.

However, the generated TENG output performance is low compared to the existing device, although the fabricated device satisfies the primary motivation and objective. Since the line patterned TENG has a potential application for self-powered sensors such as vector, motion sensors, velocity sensors, and so on. Therefore, there is need to improve the efficiency of the line pattern TENG device.

Chapter 5

Enhancement of line patterned triboelectric output performance by an interfacial polymer layer for energy harvesting application

5.1 Introduction

In order to boost the line patterned TENG output performance, sandwich-type or multi-layer materials were recently reported to enhance the practical applicability of the devices [163,168]. In this work, three TENG device has been demonstrated, such as pristine LP PET with PTFE TENG and two double dielectric layers TENG device (PVA>PET-PTFE and PEO>PET-PTFE). The PEO and PVA layers are used as positive triboelectric layers, and polytetrafluoroethylene (PTFE) is demonstrated as a negative layer. The chemical modification of the materials was analyzed by Raman spectroscopy. The open-circuit voltage, short circuit current, and instantaneous power density have been measured in contact separation mode. In addition, it investigated the influence of mechanical parameters on TENG output.

5.2 Theoretical simulation:

5.2.1. V-Q-x relationship equation:

The V-Q-x relationship of this multilayer TENG was derived from the dielectric-to-dielectric theory. In the multilayer TENG device, electric potential and transferred charge between two conductive electrodes appraised by gaussian theorem.

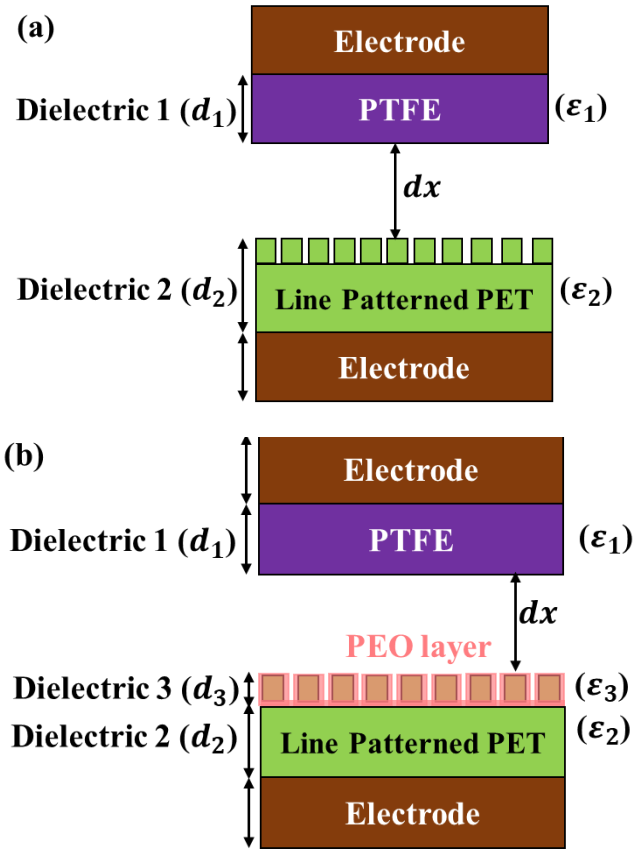

Figure 5.1(a) and (b) schematic diagram of single and double dielectric layer TENG in the contact separation mode

Figure 5.1 (a) and (b) show the vertical contact separation mechanism of a single and double dielectric layer coated TENG devices model. The coupled effect of contact electrification and electrostatic induction is the basic phenomenon of the TENG mechanism [14,160]. The conductive textile tape served as a top and bottom electrode of the device, over which the single and double electric layers were stacked. All the dielectric material has dissimilar surface charge density, which assists to affirm the positive and negative charges of the TENG layer [161]. When the force is imposed on top of the device, both dielectric layers contact each other and transfer the charge between higher to lower electron affinity phases. However, due to the electrical equilibrium state, the electrons are not moving via the external electrode when dielectric layers at the contact phase. When increasing the distance between two layers, the electric field drives the electron from a top surface to the bottom electrode that leads to the negative current. When the device

layer closure to each other for the next cycle, the reverse electrostatic potential has generated between the two surfaces, and that exhibits the positive current. The equation for the triboelectric field strength is derived from the Gaussian theorem [162].

$$\text{Dielectric } E_1 = -\frac{Q}{A\varepsilon_0\varepsilon_1} \quad \text{5.1}$$

$$\text{Dielectric } E_2 = -\frac{Q}{A\varepsilon_0\varepsilon_2} \quad \text{5.2}$$

$$\text{Dielectric } E_3 = -\frac{Q}{A\varepsilon_0\varepsilon_3} \quad \text{5.3}$$

$$\text{Inside the air gap } E_2 = -\frac{Q+\sigma x(t)}{A\varepsilon_0} \quad \text{5.4}$$

The voltage between the two electrodes can be given by

$$V = E_1 d_1 + E_2 d_2 + E_3 d_3 + E_{air} x \quad \text{5.5}$$

At OC condition, there is no charge transfer, which means that Q is 0. Therefore, the open-circuit voltage VOC is given by

$$V = \frac{Q}{A\varepsilon_0}\left(\frac{d_1}{\varepsilon_1} + \frac{d_2}{\varepsilon_2} + x(t)\right) + \frac{\sigma x(t)}{\varepsilon_0} \quad \text{5.6}$$

$$V = \frac{Q}{A\varepsilon_0}\left(\frac{d_1}{\varepsilon_{r1}} + \frac{d_2}{\varepsilon_{r2}} + \frac{d_3}{\varepsilon_{r3}} + X(t)\right) + \frac{\sigma X(t)}{\varepsilon_0} \quad \text{5.7}$$

$$V_{OC} = \frac{\sigma x(t)}{\varepsilon_0}$$

At SC condition, V is 0. Therefore, the transferred charges are (8) and (9)

$$Q_{SC} = \frac{S\sigma X(t)}{d_0 + x(t)} \quad \text{5.8}$$

$$I_{SC} = \frac{S\sigma d_0 V(t)}{(d_0 + x(t))^2} \quad \text{5.9}$$

Where Q is the charge, ε_0 air dielectric constant, $\varepsilon_{r1}, \varepsilon_{r2}$ and ε_{r3} are the dielectric constant of the tribo layers, x is the CS distance between surfaces; d_1, d_2, and d_3 are the thickness and S is the surface contact area.

5.2.2 COMSOL simulation:

To investigate the triboelectric performance of the pristine LP PET surface and interfacial polymer coated-LP PET surface, we have designed the TENG structures and simulated them in the COMSOL Multiphysics software with contact separation mode. Figure 5.2(b) and (c) depict the voltage generation between the two different TENG devices such as PTFE with pristine LP PET device and PTFE with DL_2 device. Among them, PTFE with DL_2 device has generated higher voltage compared to former. The inset image shows the before and after PEO coating of pristine LP PET. It has been observed that no voltage was generated (Figure 5.2(a)) when the mechanical force imposes on the device due to electrical equilibrium conditions. Once the mechanical force release from the device, the electric field build-up and drives the electron from one side to the other side. Hence, the PTFE with DL_2 device attains higher performance than the pristine device.

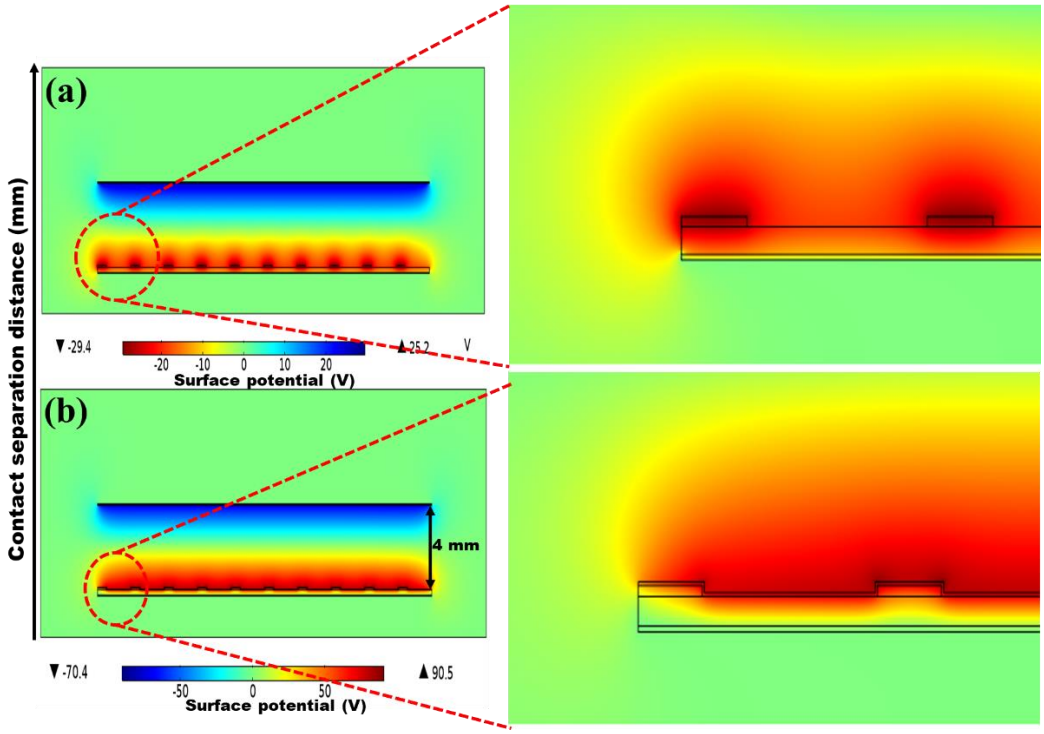

Figure 5.2 (a) both triboelectric at contact condition (b) and (c) COMSOL Multiphysics simulation of pristine and PEO coated LP PET TENG device

5.3 Experimental Section

5.3.1 PEO/PVA layer preparation:

The PEO powders were purchased from Shanghai EKEAR Biological Technology Co. Ltd. The samples were prepared with the molecular weight (Mw) of 600000 $g.mol^{-1}$ and dissolved in deionized (DI) water with a concentration of 9%. The PEO molecular weight ratio has been taken from our previous report, which has better viscosity and higher triboelectric performance than other ratios [151]. The prepared PEO solution was spin-coated on the LP PET surface (3×3 cm^2) at a rotation speed of 500 rpm for 10 sec, which assisted in obtaining a higher thickness layer and subsequently dried in an oven at 55 °C for 3 hr. Similarly, the 5 gm of PVA salt was dissolved in 50 ml of DI water and stirred for 2 hr at 95 °C that yielding without thermal decomposition of the polymer. Subsequently, the PVA layer was spin-coated on the LP PET surface at 1000 rpm and dried in an oven at 50 °C for 1 hr.

5.3.2 Double layer TENG device fabrication:

The Ytterbium-doped fibre laser of wavelength 1064nm was used for the laser surface modification as shown in Figure 4.9(a). The line pattern has been developed by laser power of 30 W which assisted to induces the protrusion on the polymer surface by photophysical mechanism. The patterns were designed in AutoCAD platform then converted it as a G code file that code has assisted the laser head. More details on the laser parameter and sample preparation can be found in our previous work [49]. The LP substrates (30×0.8×0.09 mm (L×W×t)) were cleaned with isopropanol and deionized (DI) water for 5 min. The device construction is divided into two parts, in which the top part is an un-patterned negative charge layer, and the bottom part is a laser LP positive charge layer, respectively. The commercially available PTFE layer was stacked on the conductive textile tape electrode (CTT) and antistatic tape (AST) for the top part of the device. On the other hand, the counterpart was spin-coated (PEO and PVA layer) over the LP PET and then stick on CTT and AST (Figure 5.3(a, b, c)). Eventually, both parts have parallelly arranged for a vertical contact separation

mechanism. Henceforth, the single-layer TENG consists of LP PET (bottom) and PTFE (top). The two double dielectric layer TENG device was demonstrated and represented in this work as a DL_1 (PVA coated LP PET and PTFE) and DL_2 (PEO coated LP PET and PTFE).

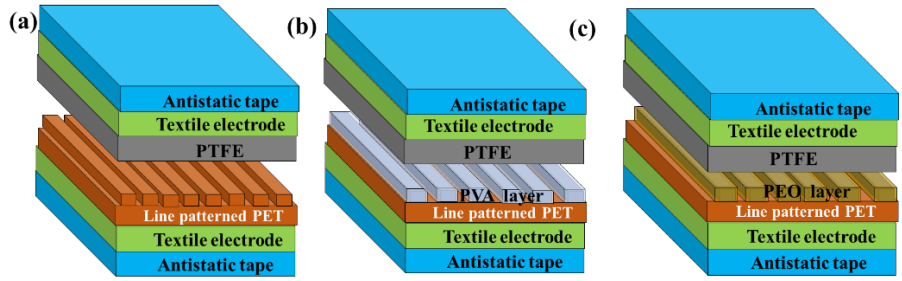

Figure 5.3 (a) Schematic diagram of laser processing (b) Pristine LP-PTFE TENG device (c) PVA coated LP-PTFE TENG (c) PEO coated LP-PTFE TENG device

5.3.3 Details of characterization tools:

The LP PET, DL1, and DL2 surface chemical modification were analyzed by Raman spectroscopy with a 523 nm excitation wavelength. The as-fabricated TENG devices were characterized in the Dynamic fatigue failure system (Popwil Model YPS-1) for investigating the output performance with different mechanical parameters condition such as frequency (1-5 Hz), contact separation (CS) distance (2-12 mm), and mechanical force (10-70 N). The Femto/Pico ammeter (B2981A) has used to measure the current generated from the TENG devices. The series resistance of 110 MΩ was used across the device to measure the open-circuit voltage by the oscilloscope. The backside electrode of DL_1 and DL_2 devices was connected with a positive lead and the electrode of PTFE was the negative lead. The output measurement was carried out after the stabilized output, which was less than 100 cycles. Since, PEO film is sensitive to humidity; the higher humidity affects the TENG performance. Hence, the whole experiments were carried out under the temperature of 25˚C and humidity of 35%.

5.4 Results and Discussion

The chemical modification and band stretching of pristine LP PET, DL_1 and DL_2 coated LP PET were analyzed by Raman spectroscopy

(Figure 5.4). The carboxylic acid group and C=O bonds of LP PET surface was confirmed and ascribed to 1726 cm^{-1} [163], but the peak intensities were reduced in the DL_1 and DL_2 layers due to —CH_2CH_2O— and —$HOCHCH_2$—layers covered on the surface. It was observed that the PEO's CH_2 group is attributed to 1281 and 1479 cm^{-1} with active Raman spectrum [164]. However, at 1281 cm^{-1} peak has raised which might be due to the amorphous part of the polymer chain [165]. The oxygen group can donate the electron which increases the electrification of the device [166]. The TENG device's output is improved as a result of these surface modifications.

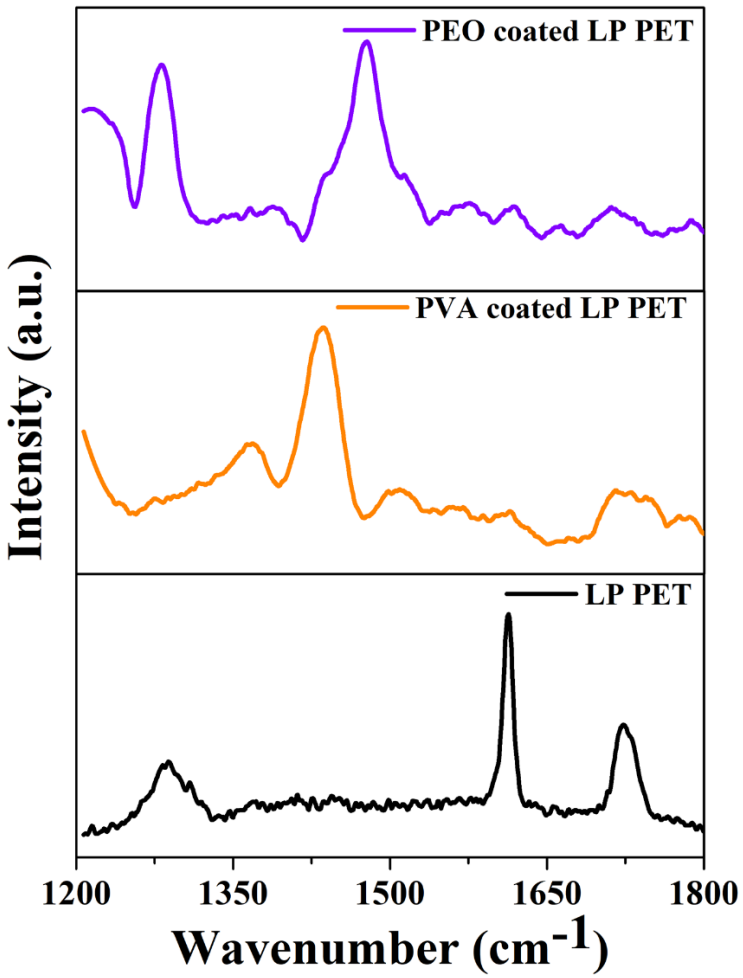

Figure 5.4 Raman shift of before and after PEO/PVA coated LP PET surface

5.4.1 Charge transport mechanism of multilayer TENG:

Initially, this work investigated triboelectric performance with the PTFE and LP PET. The basic TENG mechanism is based on the coupled effect

of contact electrification and electrostatic induction and is shown in Figure 5.5. When the force is imposed on the device, both dielectric layers contact each other, creating oppositely charged surfaces. When the external force is withdrawn from the device, the potential drop is created between them. However, some electron trapped in the shallow site of the LP PET layer drives to the electrode. The surface charge density was reduced due to merging the positive charge with the electrode. On the other hand, the PTFE and PET belong to the tribo-negative materials category [167]. So, the same property material may not provide superior performance due to the screening effect. Thus, to improve the TENG performance, we introduced a multilayer composite structure which boosted the TENG output. The multilayer TENG consists of a charge collection layer (CCL), charge transport layer (CTL), and electrode. Here, the PEO is considered a CCL, and LP PET is CTL. The reason for selecting a CTL is that it will improve the interfacial area and increase the charge density between CCL and CTL [168]. The function of the CCL layer is to collect charges from the opposite frictional layer, and CTL helps to trap the charges in deep and reduce the obstruction of new charges entering the system by transferring them.

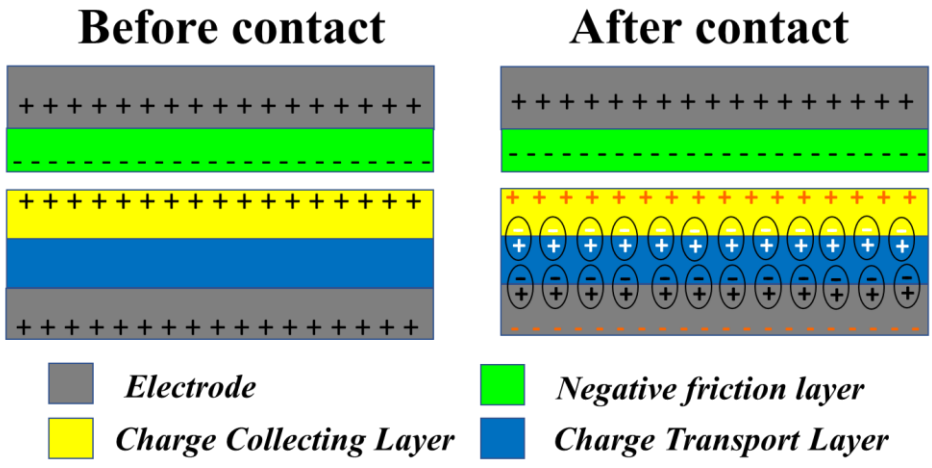

Figure 5.5 schematics of the charge transport mechanism

In the multilayer TENG mechanism, Due to contact electrification, the positive surface charges are generated on the CCL surface and induce negative charges beneath the positive tribo-material. These negative charges attract the positive charges from the top of CTL. Therefore, the

electrons are trapped deep in the sites by CTL and conserved for a longer time. Because the CTL (LP PET) has large charge trap densities compared to CCL(PEO), this causes the surface potential to saturate, increasing the potential difference between electrodes rapidly. Hence, the interfacial layer significantly enriches the surface charge density and accumulation, resulting in improved TENG performance.

5.4.2 Triboelectric output performance measurement:

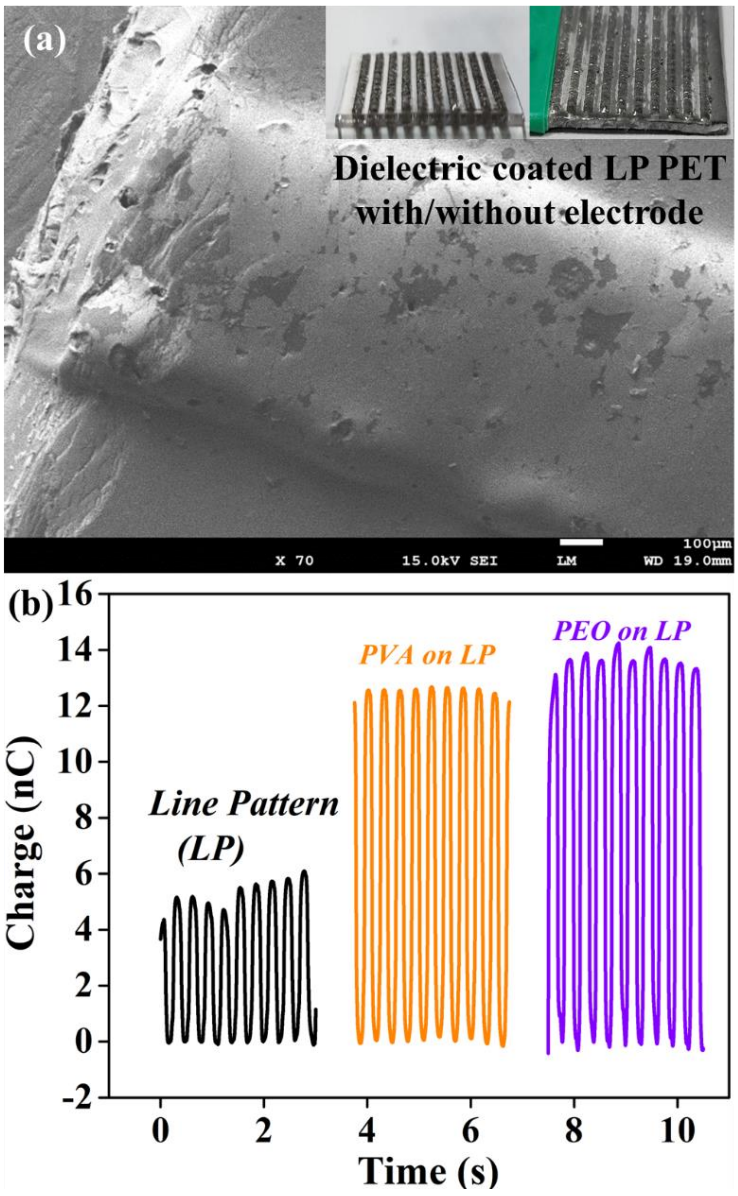

Figure 5.6 (a) Photographic image of the dielectric coated with and without electrode LP PET (b) transferred charges of single and double-layered TENG

The triboelectric output performance was evaluated for the pristine LP TENG and DL_1 and DL_2 TENG by the contact separation mechanism. These devices were initially deployed with a force of 50 N, frequency of 4 Hz, and CS distance of 4 mm for measuring the open circuit (V_{oc}) voltage and short circuit current (I_{sc}).

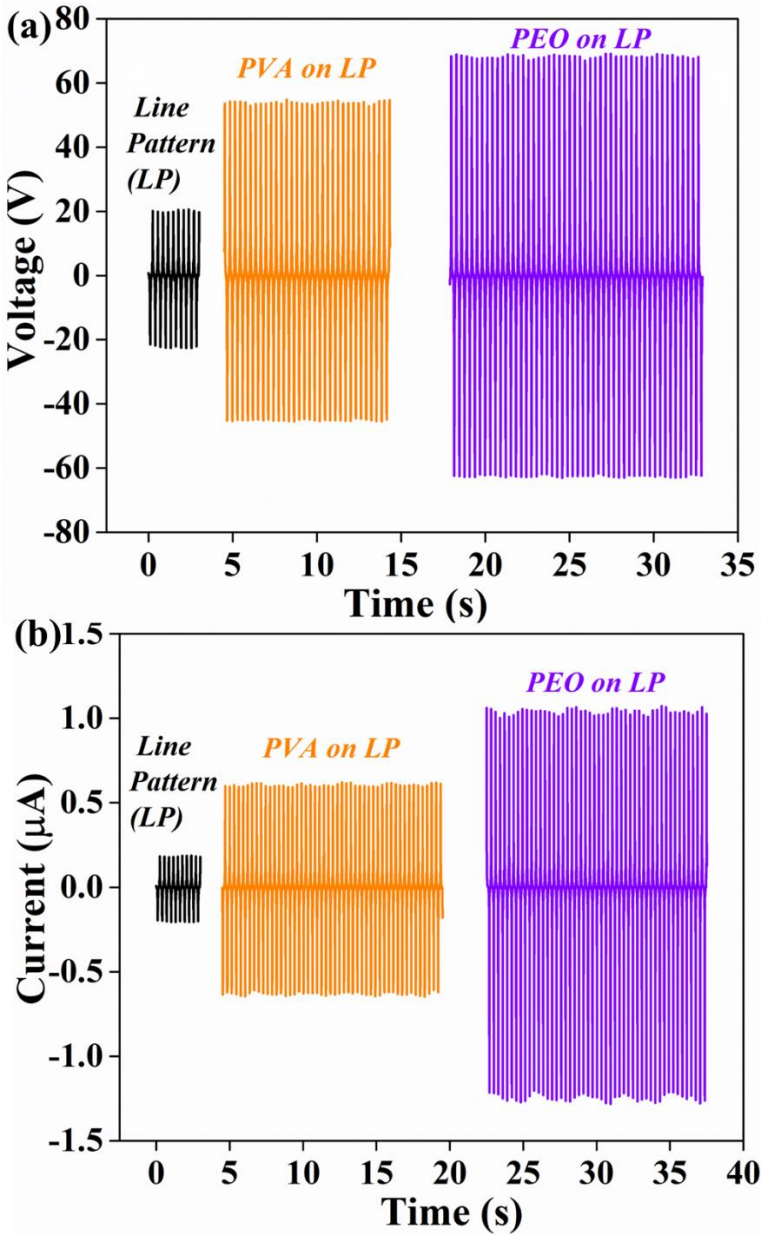

Figure 5.7 (a)&(b) V_{oc} and I_{sc} measurement of DL_1 and DL_2 TENG device with the fixed operational parameters i.e., frequency of 5 Hz, CS distance 4 mm, and force of 50 N

Figure 5.6(a) depicts the FESEM image of DL_2 coated LP PET and inset image shows the digital photos of the dielectric coated PET with/without electrode. The transferred charge was measured for the single, DL_1 and

DL_2 TENG (Figure 5.6(b)), in which the DL_2 TENG device (13.8 nC) has transferred more charges compared to other devices. Such high performance is attributed to the higher surface contact area as well improved interfacial area between the LP PET and PEO which promotes charges accumulation [169] and thus enhanced transferred charges.

Figure 5.7 (a) and (b) depicts the V_{oc} and I_{sc} of single, DL_1 and DL_2 TENG device. The single-layer TENG device has generated peak-to-peak (PP) V_{oc} of 42.65 V and I_{sc} of 0.485 μA at a load resistance of 110 MΩ. The DL_2 device has generated peak to peak V_{oc} of 131.85 V and I_{sc} of 2.327 μA. The DL_2 device has obtained 2-fold performance of single-layer TENG device. The comprehensive results are tabulated in table 5.1. It is due to more charge accumulation and a higher tendency to trap more charges between LP PET and PEO layer, owing to its lower electron affinity and the unique PEO chains, such as –C–, –O–, and –H–, which repelled electrons from its surface by the electrostatic effect [170]. This property substantially aids in improving the triboelectrification process of the device. Also, the larger surface contact area is one of the inevitable factors to enhance its output performance. Compared to our previous work [171], the present study improves the output performance 4-fold higher by the effect of the PEO layer as well higher surface contact area. For further investigations, PEO-coated LP TENG has been used.

5.4.3 Influence of mechanical parameter in DL_2 TENG:

It is essential to examine the DL_2 device performance with various mechanical parameters such as mechanical force, frequency, contact separation distance, and load resistance. Figure 5.8(a) and (b) depict the V_{oc} and I_{sc} of the DL_2 TENG device at different frequencies of 1-5 Hz, fixed force, and CS distance of 50 N and 4 mm with 110 MΩ resistance. Lower V_{oc} (85.69 V) and I_{sc} (0.782 μA) were generated at 1 Hz. However, the device exhibited higher output (161.16 V, 2.466 μA). at a frequency of 5 Hz. The output performance has considerably increased by increasing the frequency. More tapping induced faster electron flow between the surface [154]. Based on the following equation, the output performance under various frequency conditions has been analysed.

$$V_{oc} = \frac{\sigma * x(t)}{\varepsilon_0} \quad \text{..... 5.10}$$

$$I_{sc} = \frac{2\pi S \sigma f x_{max}}{d_0} \quad \text{..... 5.11}$$

Where x is the displacement, ε_0 is the permittivity of vacuum, S is the surface area, d_0 is the thickness of the dielectric layer, σ is surface charge density, and f is the frequency. Since the frequency is proportional to the current which increases with increasing the frequency but Voc is not improving significantly beyond 5 Hz which only dependant on displacement not on frequency [172,173].

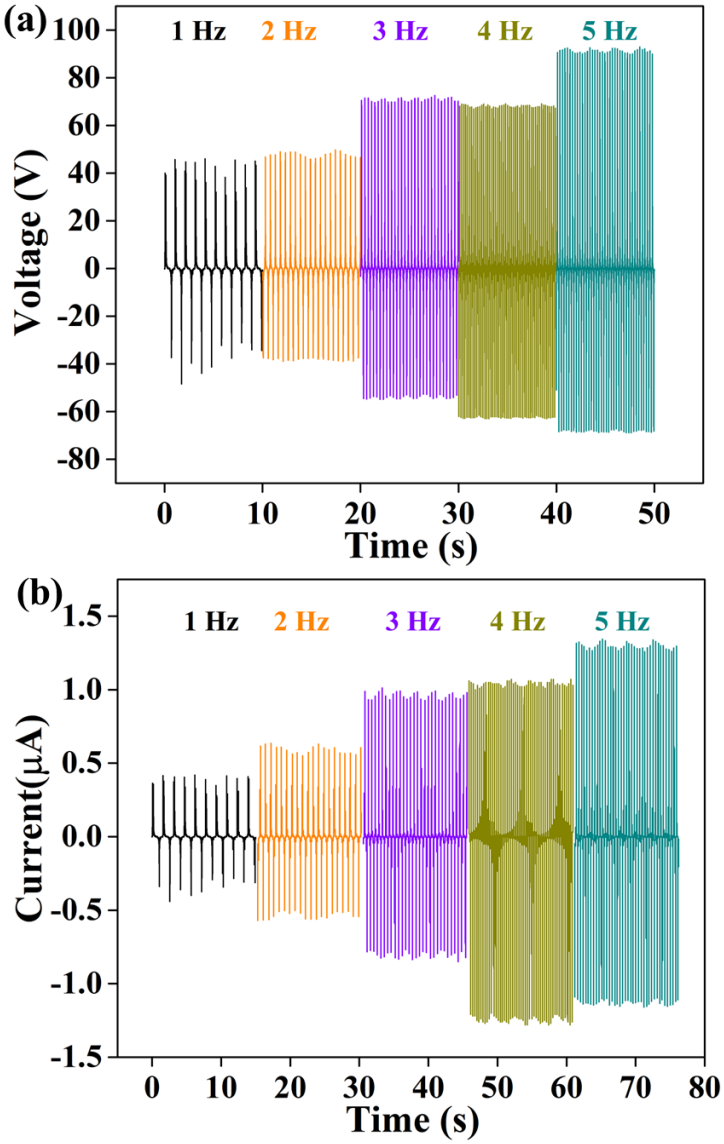

Figure 5.8 (a) and (b) V_{oc} and I_{sc} of DL_1/DL_2 TENG with various frequency (1-5 Hz); CS distance and load were fixed at 4 mm, and 50 N.

The device's functional ability is determined by the contact separation distance. So, the fabricated device was deployed at various CS distances from 2-12 mm with an interval of 2 mm, a frequency of 4 Hz, and a fixed load of 50 N shown in Figure 5.9(a) and (b).

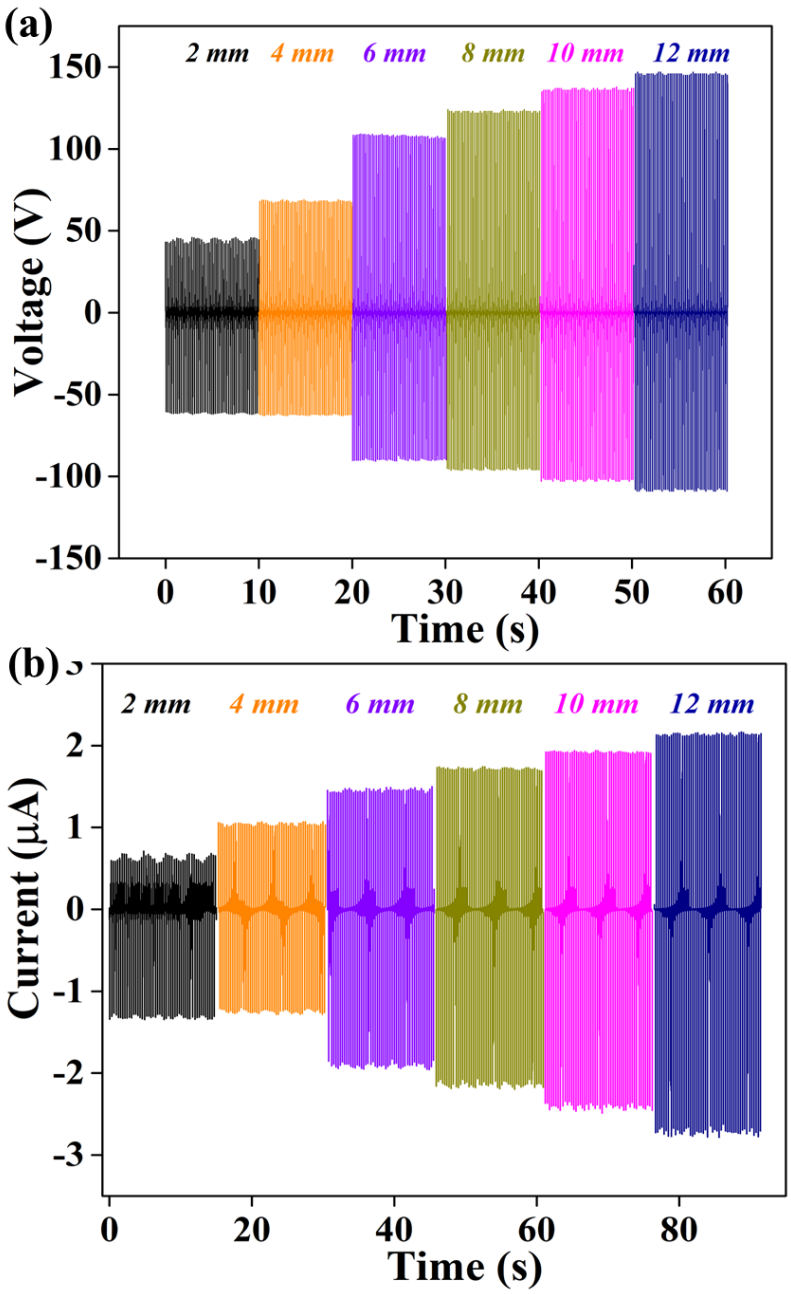

Figure 5.9 (a)&(b) V_{oc} and I_{sc} evaluation under different CS distance (2 to12 mm) with a constant load of 50 N and frequency of 4 Hz.

Due to the weaker electric field generated between the two surfaces, the smaller CS distance has attained a low I_{sc} of 2.0494 μA and V_{oc} of

107.42 V. At the larger CS distance (12 mm), the DL_2 device has obtained a notable output V_{oc} of 254 V and I_{sc} of 4.848 μA compared to other distances. According to Eq(3), the larger contact separation distance improves relative contact velocity which leads to drive the electron flow very fast [49,151]. Above a certain distance, the system performance gets slowly saturated.

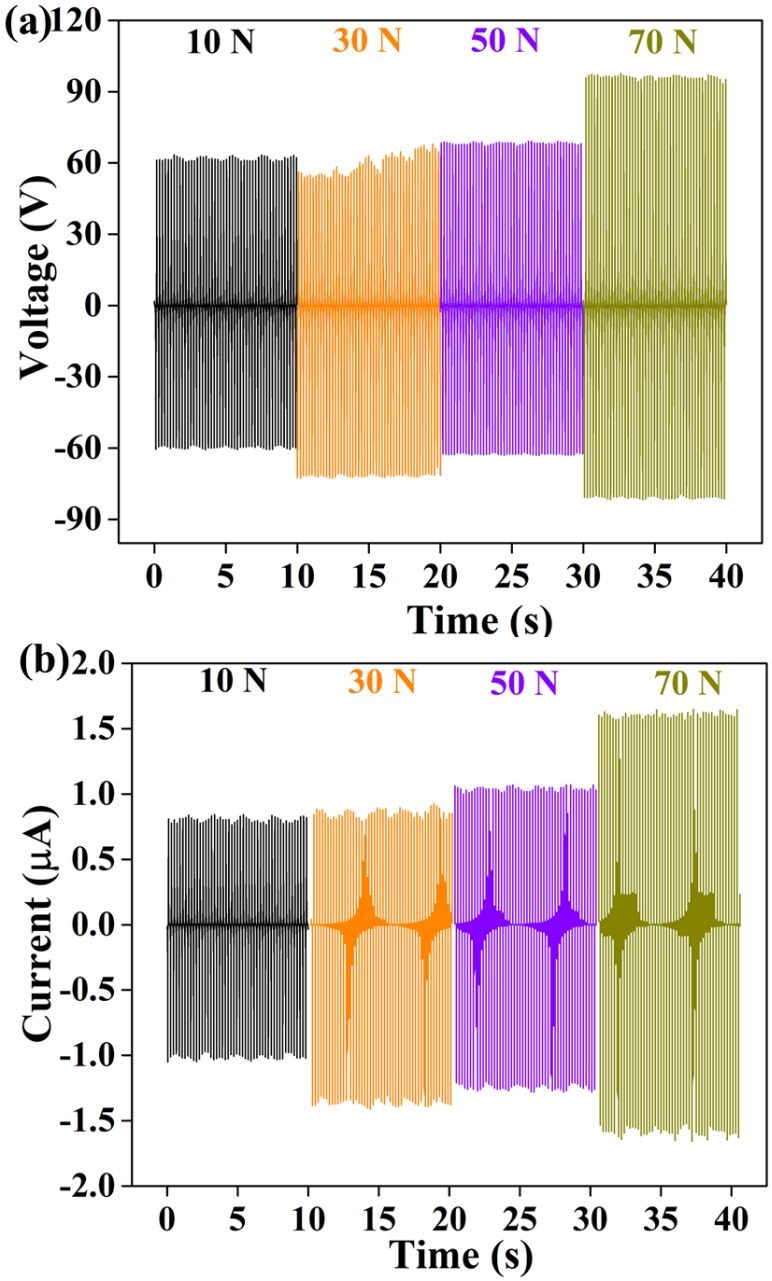

Figure 5.10 (a) and (b) shows the performance of V_{oc} and I_{sc} for different contact forces (10- 70 N) with a set value of frequency and CS distance (4 Hz and 4 mm).

Mechanical force is a vital parameter that assists to correlate the effective contact area with induced charges. Hence, the DL_2 TENG device performance was investigated thoroughly with various contact forces from 10 N to 70 N and it depicted in Figure 5.10(c) and (d). It is observed that the lower contact force of 10 N yields a smaller potential of 123.08 V and I_{sc} of 1.864 μA. The output range progressively improved (123.08 to 178.25 V) as the contact force was increased from 10 N to 70 N. At the higher level of contact force, the PTFE layer completely contacts each corner of the DL_2 surface due to the elastic in nature. The higher contact area has more interaction between the two subjected dielectric layers which increases the kinetic energy of electron transfer [154,174,175].

The endurance of a mechanical energy harvesting system is essential for assessing its stability and reliability. The DL_2 TENG device was operated for 10,000 cycles at 4 Hz frequency, 50 N mechanical force, and 4 mm CS distance (Figure 5.11(a)). In the graph, the last 500 cycles of each consecutive 1000 has been plotted like (1-500, 1501-2000, 2501-3000…..). The device exhibits excellent mechanical robustness without any notable deterioration in the I_{sc}.

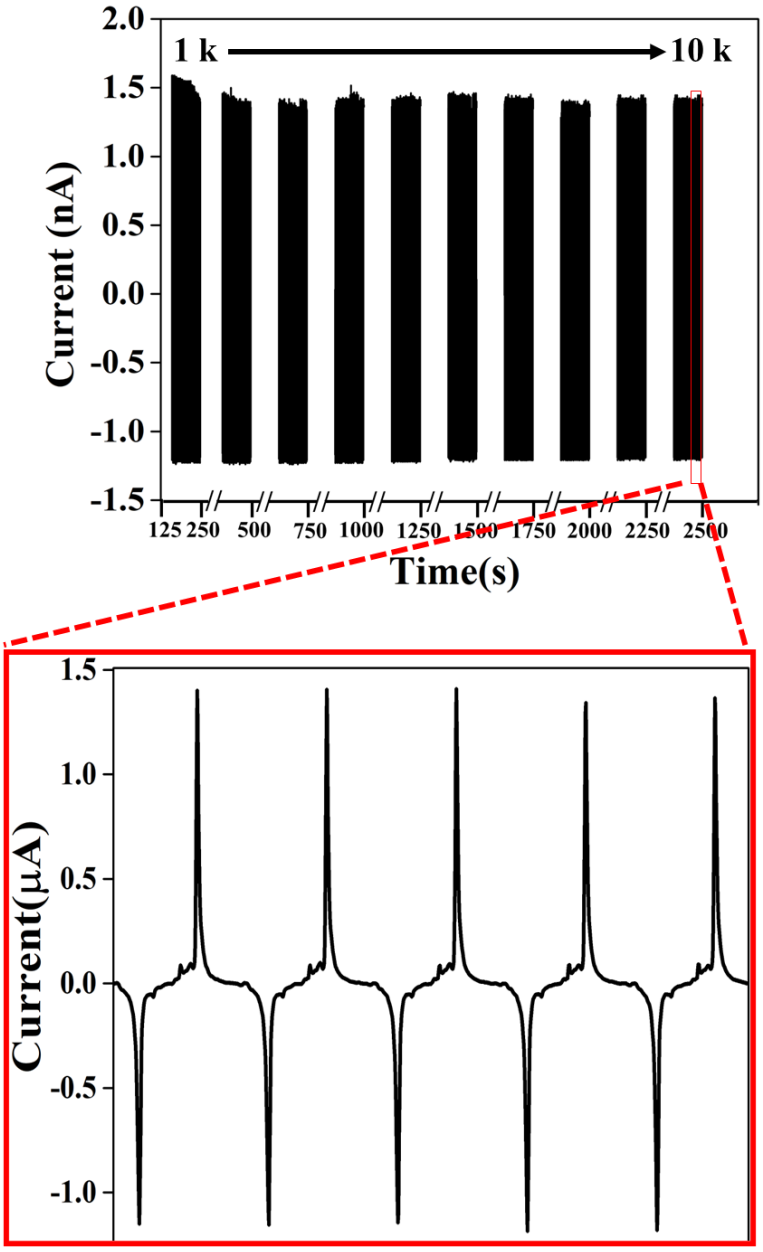

Figure 5.11 Endurance evaluation of I_{sc} for DL_2 device operated up to 10,000 cycles with a force of 50 N, frequency of 4 Hz, and CS distance of 4mm

The various load resistance (1 kΩ to 4 GΩ) was used for maximum output voltage and I_{sc} drop shown in Figure 5.12(a). The V_{oc} has gradually increased from 0 to 363.72 V as load resistance increases and saturated after 1 GΩ but the I_{sc} was reversed, due to higher resistance, the current flow decreased drastically beyond 110 MΩ.

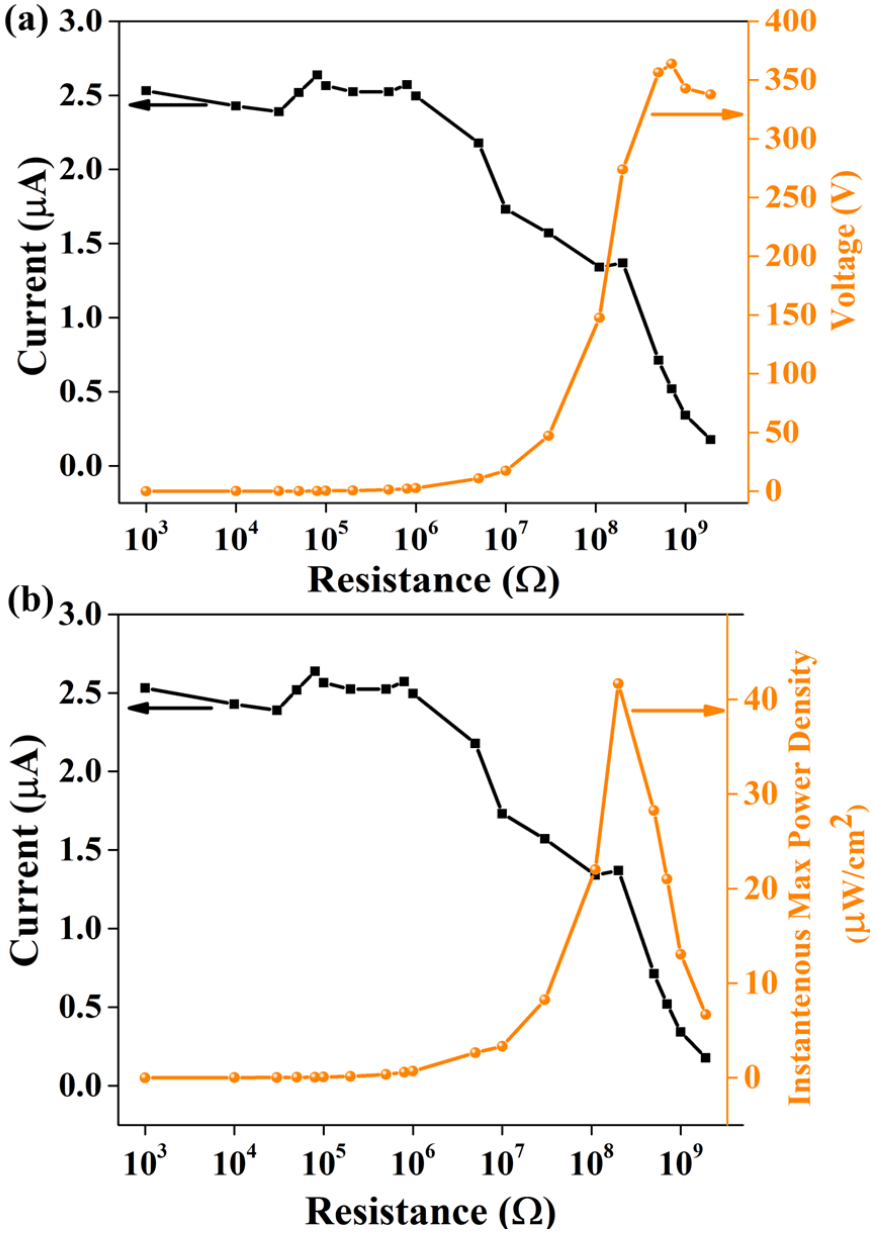

Figure 5.12 (a) voltage and across the different load resistance (1 KΩ to 4 GΩ) (b) Power density measurement with respect to the different load resistance.

The output power density was estimated from Eqn. (5.12).

$$P = \frac{I^2 R}{A} \quad \text{..... 5.12}$$

Where *I* denoted as current, *R* is the load resistance and *A* is the area. Also, the above Eq (5) was used to appraise the instantaneous max power density and I_{sc} drop (Figure 5.12(b)). The power density steadily increased when the load resistance increased from 1 kΩ to 110 MΩ. The maximum power density of 41.6 μW/cm^2 was obtained at 110 MΩ load

resistance. Hence, this maximum power density can be used to power up the microsensors and low-power electronic devices [176,97,103].

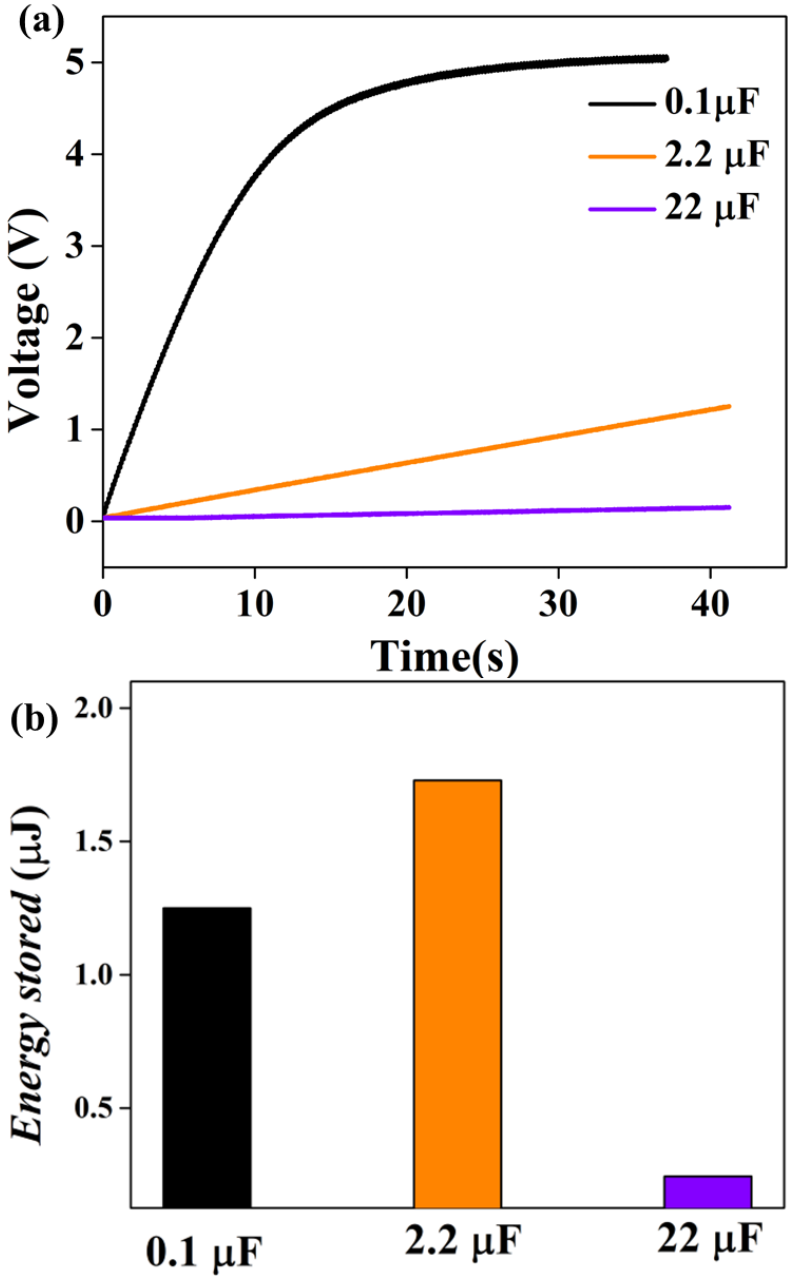

Figure 5.13 (a) the DL_2 device deployed to generate the voltage that stored in the different capacitor (b) the amount of energy stored in various capacitors

Furthermore, Figure 5.11(b) depicts the storage capability of the DL_2 device in which the generated energy is stored in three different capacitors (0.1 μF, 2.2 μF, 22 μF) with a length of 40 s by using the external circuit connection (Figure 5.11(a)). It observed that the device charged a maximum of 5 V with a small capacitance of 0.1 μF at 40 s,

in case of higher capacitance it required more time to store maximum voltage. Figure 5.11(c) shows the energy stored in various capacitance commercial capacitors in that the 2.2 μF capacitor has stored the maximum energy of 1.73 μJ with a short period than others. It noticed that increasing capacitance will increase the time for charging and discharging, hence the optimal capacitance (2.2 μF) will be appropriate. The charged capacitor was deployed to glow ten LEDs with high intensity and shown in (Figure 5.11(d). Thus, the DL_2 device can able to power up the micro and nanoelectronics devices.

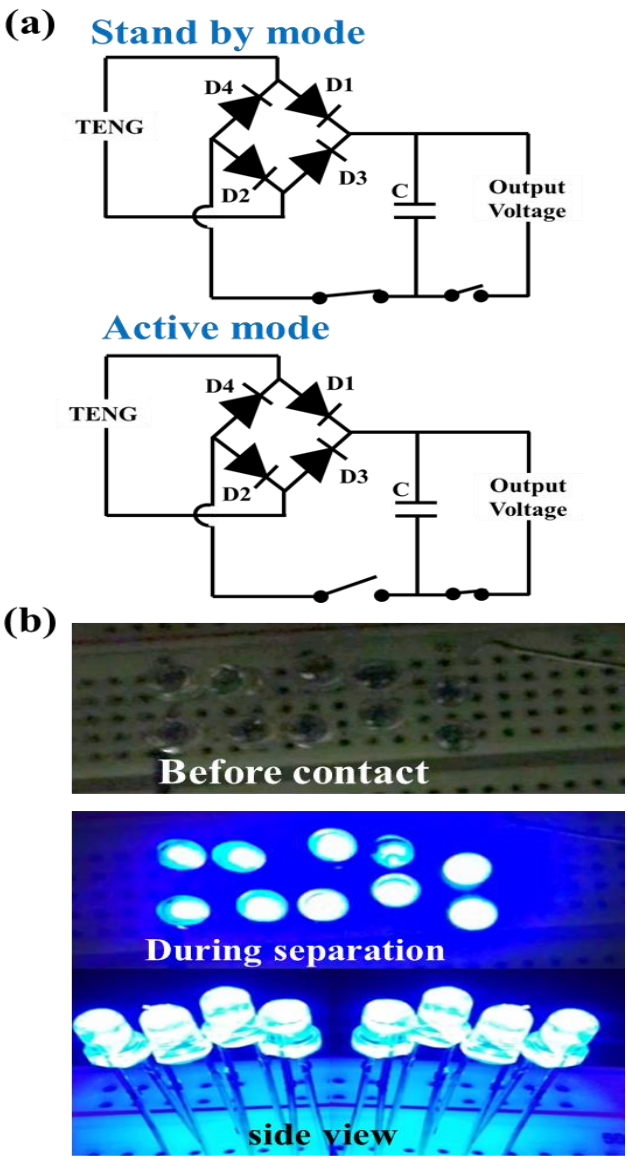

Figure 5.14 (a) Schematic diagram of charging circuit and (d) digital image of ten LED lighting up when contact separation of DL_2 device.

5.5 Summary:

- Single and two different double layers (DL_1, DL_2) coated LP TENG device was demonstrated to boost the triboelectric output performance.
- The DL_2 device was obtained higher performance than the DL_1 and single-layer device due to enhanced interfacial area as well surface contact area. Subsequently, the triboelectric behaviours were thoroughly investigated with different mechanical parameters such as mechanical force (10-70 N), frequency (1-5 Hz), CS distance (2-12 mm), and load resistance (1000- 4 GΩ).
- The optimized mechanical parameters resulted in a higher output voltage, current, and instantaneous power density of 131 V and 2.32 μA, 41.6 W/cm^2 for the DL_2 device (4 Hz, 4 mm, and 50 N). It enhanced 2-fold of single layer TENG device and 4-fold higher than the PA6-laser patterned PET TENG device (our previous report), which satisfies the motivation of this work.
- Additionally, the DL_2 device endurance was evaluated for 10,000 cycles which shows no negligible degradation. Eventually, the serially connected ten LEDs glowed with charged capacitor. Hence, the PEO coated LP TENG device will be suitable for powering micro and nano-electronic devices.

Chapter 6

Conclusion and Future Scope

The eco-friendly piezoelectric and triboelectric nanogenerators have been successfully developed and demonstrated. The effective parameters for the performance enhancement have been studied thoroughly. Thus, the overall research work can be concluded as follows

6.1 Conclusion

6.1.1 Development of Sn doped ZnO-based eco-friendly piezoelectric nanogenerator for energy harvesting applications.

- An eco-friendly ZnO piezoelectric nanogenerator was successfully fabricated by the cost-effective hydrothermal method.
- Enhancing the pristine PENG device performance, Sn was doped with different concentration (0%, 2.5%, and 5%) and optimized.
- The 2.5% Sn doped ZnO PENG device achieved higher performance than the pristine PENG device under 30 N external force and 940 MΩ load resistance.
- The Sn doped PENG ZnO device achieved the maximum output voltage of 3.86 V and short circuit current of 67.92 nA. It is due to increment in the carrier concentration. Eventually, all PENG devices were deployed in musical drums condition and investigated the piezo performance. It observed that the developed device could generate energy from non-uniform load conditions.
- In the as-prepared PENG device, the electrode and PENG device material was chosen as eco-friendly, which accomplishes our primary objective.

However, the output performance of the doped and pristine PENG device is not sufficient to power the microwatt rating electronic device, though it is flexible and eco-friendly. Further widening the applicability of the mechanical energy harvesting, the triboelectric nanogenerator would be the appropriate method, which investigated and concluded in the next chapter.

6.1.2 Enhancement of Triboelectric Nanogenerator Output Performance by Laser 3D-Surface Pattern Method for Energy Harvesting Application.

In this chapter, the eco-friendly material's triboelectric performance has been enhanced by the surface modification method. There are several methods involved in surface modification. However, laser surface patterning (LSP) is an alternative approach due to large-scale manufacturing, ease of fabricating complex structures, and not requiring a sophisticated environment.

- To affirm the suitability of the surface modification process, the TENG was designed with a simple line pattern and evaluated the performance. It confirms that the surface modification or pattern technique is a suitable method for enhancing the TENG output.
- Primarily, the COMSOL theoretical simulation has been used to evaluate electric potential (V) and transferred charges (nC) of the TENG device. It observed that the line patterned TENG has attained higher performance than pristine.
- The laser surface patterning process was used as surface modification and optimized the laser process parameters.
- In addition, to investigate the effect of geometrical features, three different micro patterns have been developed by LSP, such as circle, line, and X pattern, which enhanced the surface contact area of the TENG.
- The line patterned TENG device has notably improved the peak-to-peak OC voltage of 36 V and short circuit current of 0.46 μA compared to other patterns due to improved surface contact area and surface charge density. The maximum power density (0.8 $\mu W/cm^2$) was attained at 100 MΩ load resistance.
- Moreover, to achieve maximum output in the mechanical energy harvesting, the influence of mechanical parameters has been optimized such as force 50 N, 5 Hz frequency, 4 mm contact separation distance.

- The line patterned TENG device has shown stable output performance for 10000 cycles without negligible loss.

However, the generated TENG output performance is low compared to the existing device, although the fabricated device satisfies the primary motivation and objective. Since the line pattern TENG has a potential application for self-powered sensors such as vectors, motion sensors, velocity sensors, and so on. Therefore, the line patterned output needs to be boosted.

6.1.3 Enhancement of line patterned triboelectric output performance by an interfacial polymer layer for energy harvesting application.

The line patterned (LP) TENG device performance has been further enhanced by the use of interfacial layer.

- To ensure the device's functionality with an interfacial layer, the device structure was demonstrated in the COMSOL tool. It affirms that the interfacial layer boosted the TENG performance.
- Single and two different double layers (DL1, DL2) coated LP TENG devices were demonstrated to boost the triboelectric output performance. The DL_2 device exhibited higher performance than the DL_1 and single-layer device due to the enhanced interfacial and surface contact area.
- Subsequently, the triboelectric behaviours were thoroughly investigated experimentally with different mechanical parameters such as mechanical force (10-70 N), frequency (1-5 Hz), CS distance (2-12 mm), and load resistance (1000- 4 GΩ).
- The optimized mechanical parameters resulted in a higher voltage, current, and instantaneous power density of 131 V and 2.32 μA, 41.6 W cm^{-2} for the DL2 device (4 Hz, 4 mm, and 50 N).
- The performance was enhanced 2-fold for the single-layer TENG device and 4-fold for the DL2 device compared to the PA6-laser patterned PET TENG device (our previous report), which satisfies the motivation of this work.

- Additionally, the DL_2 device endurance was evaluated for 10,000 cycles which shows no negligible degradation. Eventually, the serially connected ten LEDs glowed with the charged capacitor. Hence, the PEO-coated (DL_2) LP TENG device will be suitable for powering micro and nano-electronic devices.

Table 6.1 summaries the output responses of as fabricated PENG and TENG device in the overall thesis. It clearly evidences that the PEO coated LP TENG has achieved a maximum output performance than others. Additionally, the as developed eco-friendly materials and its performances have good agreements with motivation and main objectives.

Table 6.1 Summarized output response of Piezo and Tribo Nanogenerators

Device	Voltage	Current	Power or Power density
ZnO Piezo	2.85 V	17 nA	
Sn doped ZnO	4.15 V	36 nA	149 nW
PET-PA6	23 V	0.33 µA	7.59 µW/cm^2
LP PET-PA6	35.7 V	0.46 µA	16.42 µW/cm^2
PEO coated LP PET-PA6	131.85 V	2.327 µA	41.6 µW/cm^2

6.2 Future scope:

The eco-friendly device will be inevitable for future electronic devices. Therefore, there are vast opportunities for eco-friendly TENG sensors. Here are some suggestions for the future work:

1. The external power conversion circuits are one major e-waste in the past two decades. The laser fabricated DC triboelectric energy harvester can be a viable route to reduce e-waste.
2. Due to inherent functionality option in the TENG, laser processing will be an incipient field in the TENG based human health monitoring sensors.

Reference

1. Li, Z.B., Li, H.Y., Fan, Y.J., Liu, L., Chen, Y.H., Zhang, C. and Zhu, G., 2019. Small-Sized, Lightweight, and Flexible Triboelectric Nanogenerator Enhanced by PTFE/PDMS Nanocomposite Electret. ACS applied materials & interfaces, 11(22), pp.20370-20377.
2. Zhao, S., Li, J., Cao, D., Zhang, G., Li, J., Li, K., Yang, Y., Wang, W., Jin, Y., Sun, R. and Wong, C.P., 2017. Recent advancements in flexible and stretchable electrodes for electromechanical sensors: strategies, materials, and features. ACS applied materials & interfaces, 9(14), pp.12147-12164.
3. Zhang, X.S., Han, M., Kim, B., Bao, J.F., Brugger, J. and Zhang, H., 2018. All-in-one self-powered flexible microsystems based on triboelectric nanogenerators. Nano Energy, 47, pp.410-426.
4. Yi, F., Zhang, Z., Kang, Z., Liao, Q. and Zhang, Y., 2019. Recent advances in triboelectric nanogenerator-based health monitoring. Advanced Functional Materials, 29(41), p.1808849.
5. Zhang, Q., Zhang, Z., Liang, Q., Gao, F., Yi, F., Ma, M., Liao, Q., Kang, Z. and Zhang, Y., 2019. Green hybrid power system based on triboelectric nanogenerator for wearable/portable electronics. Nano Energy, 55, pp.151-163.
6. Mao, Y., Zhang, N., Tang, Y., Wang, M., Chao, M. and Liang, E., 2017. A paper triboelectric nanogenerator for self-powered electronic systems. Nanoscale, 9(38), pp.14499-14505.
7. Cheng, T., Li, Y., Wang, Y.C., Gao, Q., Ma, T. and Wang, Z.L., 2019. Triboelectric nanogenerator by integrating a cam and a movable frame for ambient mechanical energy harvesting. Nano Energy, 60, pp.137-143.
8. Lin, L., Wang, S., Xie, Y., Jing, Q., Niu, S., Hu, Y. and Wang, Z.L., 2013. Segmentally structured disk triboelectric nanogenerator for harvesting rotational mechanical energy. Nano letters, 13(6), pp.2916-2923.

9. S. P. Beeby and T. O'Donnell, 2009,"Electromagnetic energy harvesting," in Energy Harvesting Technologies, ed: Springer, pp. 129-161.
10. Wang, P., Pan, L., Wang, J., Xu, M., Dai, G., Zou, H., Dong, K. and Wang, Z.L., 2018. An ultra-low-friction triboelectric–electromagnetic hybrid nanogenerator for rotation energy harvesting and self-powered wind speed sensor. ACS nano, 12(9), pp.9433-9440.
11. X. Wu, D.W. Lee, 2019, Miniaturized piezoelectric energy harvester for battery-free portable electronics, Int. J. Energy Res. 43 (6) 2402–2409.
12. Chen, X., Han, M., Chen, H., Cheng, X., Song, Y., Su, Z., Jiang, Y. and Zhang, H., 2017. A wave-shaped hybrid piezoelectric and triboelectric nanogenerator based on P (VDF-TrFE) nanofibers. Nanoscale, 9(3), pp.1263-1270.
13. Zeng, Q., Wu, Y., Tang, Q., Liu, W., Wu, J., Zhang, Y., Yin, G., Yang, H., Yuan, S., Tan, D. and Hu, C., 2020. A high-efficient breeze energy harvester utilizing a full-packaged triboelectric nanogenerator based on flow-induced vibration. Nano Energy, 70, p.104524.
14. Fan, F.R., Tian, Z.Q. and Wang, Z.L., 2012. Flexible triboelectric generator. Nano energy, 1(2), pp.328-334.
15. Zheng, Q., Shi, B., Li, Z. and Wang, Z.L., 2017. Recent progress on piezoelectric and triboelectric energy harvesters in biomedical systems. Advanced Science, 4(7), p.1700029.
16. Zhu, G., Pan, C., Guo, W., Chen, C.Y., Zhou, Y., Yu, R. and Wang, Z.L., 2012. Triboelectric-generator-driven pulse electrodeposition for micropatterning. Nano letters, 12(9), pp.4960-4965.
17. C Jacques and C Pierre, 1880, "Development, via compression, of electric polarization in hemihedral crystals with inclined faces". In: Bull. Soc. Minérologique Fr 3, pp. 90–3.
18. Gabriel Lippmann, 1881 "Principe de la conservation de l'électricité, ou second principe de la théorie des phénomènes électriques". In: J. Phys. Theor. Appl. 10.1, pp. 381–394.

19. Fu, Y.Q., Luo, J.K., Nguyen, N.T., Walton, A.J., Flewitt, A.J., Zu, X.T., Li, Y., McHale, G., Matthews, A., Iborra, E. and Du, H., 2017. Advances in piezoelectric thin films for acoustic biosensors, acoustofluidics and lab-on-chip applications. Progress in Materials Science, 89, pp.31-91.
20. Dagdeviren, C., Joe, P., Tuzman, O.L., Park, K.I., Lee, K.J., Shi, Y., Huang, Y. and Rogers, J.A., 2016. Recent progress in flexible and stretchable piezoelectric devices for mechanical energy harvesting, sensing and actuation. Extreme Mechanics Letters, 9, pp.269-281.
21. S. Roundy and P. K. Wright, 2004 "A piezoelectric vibration-based generator for wireless electronics," Smart Materials and structures, vol. 13, p. 1131.
22. N. White, P. Glynne-Jones, and S. Beeby , 2001 "A novel thick-film piezoelectric micro-generator," Smart Materials and Structures, vol. 10, pp. 850-852.
23. Dhakar, L., Liu, H., Tay, F.E.H. and Lee, C., 2013. A new energy harvester design for high power output at low frequencies. Sensors and Actuators A: Physical, 199, pp.344-352.
24. J. Kymissis, C. Kendall, J. Paradiso, and N. Gershenfeld, "Parasitic power harvesting in shoes," in Wearable Computers, 1998. Digest of Papers. Second International Symposium on, 1998, pp. 132-139.
25. K. Uchino. Advanced Piezoelectric Materials: Science and Technology. Woodhead Publishing Series in Electronic and Optical Materials. ISBN: 9781845695347.
26. Zhu, G., Yang, R., Wang, S. and Wang, Z.L., 2010. Flexible high-output nanogenerator based on lateral ZnO nanowire array. Nano letters, 10(8), pp.3151-3155.
27. Park, K.I., Lee, M., Liu, Y., Moon, S., Hwang, G.T., Zhu, G., Kim, J.E., Kim, S.O., Kim, D.K., Wang, Z.L. and Lee, K.J., 2012. Flexible nanocomposite generator made of BaTiO3 nanoparticles and graphitic carbons. Advanced materials, 24(22), pp.2999-3004.
28. Kwon, S.H., Park, J., Kim, W.K., Yang, Y., Lee, E., Han, C.J., Park, S.Y., Lee, J. and Kim, Y.S., 2014. An effective energy harvesting

method from a natural water motion active transducer. Energy & Environmental Science, 7(10), pp.3279-3283.

29. Hwang, G.T., Park, H., Lee, J.H., Oh, S., Park, K.I., Byun, M., Park, H., Ahn, G., Jeong, C.K., No, K. and Kwon, H., 2014. Self-powered cardiac pacemaker enabled by flexible single crystalline PMN-PT piezoelectric energy harvester. Advanced materials, 26(28), pp.4880-4887.
30. Mokrý, P., 2016, "100 years of piezoelectric materials in acoustics: From a sonar to active metasurfaces. In Proceedings of meetings on acoustics 22ICA, Acoustical Society of America, 28(1), p. 045008.
31. Dagdeviren, C., Yang, B.D., Su, Y., Tran, P.L., Joe, P., Anderson, E., Xia, J., Doraiswamy, V., Dehdashti, B., Feng, X. and Lu, B., 2014. Conformal piezoelectric energy harvesting and storage from motions of the heart, lung, and diaphragm. Proceedings of the National Academy of Sciences, 111(5), pp.1927-1932.
32. Lu, B., Chen, Y., Ou, D., Chen, H., Diao, L., Zhang, W., Zheng, J., Ma, W., Sun, L. and Feng, X., 2015. Ultra-flexible piezoelectric devices integrated with heart to harvest the biomechanical energy. Scientific reports, 5(1), pp.1-9.
33. Zhu, G., Yang, W.Q., Zhang, T., Jing, Q., Chen, J., Zhou, Y.S., Bai, P. and Wang, Z.L., 2014. Self-powered, ultrasensitive, flexible tactile sensors based on contact electrification. Nano letters, 14(6), pp.3208-3213.
34. Sun, Q., Seung, W., Kim, B.J., Seo, S., Kim, S.W. and Cho, J.H., 2015. Active matrix electronic skin strain sensor based on piezopotential-powered graphene transistors. Advanced Materials, 27(22), pp.3411-3417.
35. Shenck, N.S. and Paradiso, J.A., 2001. Energy scavenging with shoe-mounted piezoelectrics. IEEE micro, 21(3), pp.30-42.
36. Ishida, K., Huang, T.C., Honda, K., Shinozuka, Y., Fuketa, H., Yokota, T., Zschieschang, U., Klauk, H., Tortissier, G., Sekitani, T. and Toshiyoshi, H., 2012. Insole pedometer with piezoelectric energy harvester and 2 V organic circuits. IEEE Journal of Solid-State Circuits, 48(1), pp.255-264.

37. Khalifa, S., Lan, G., Hassan, M., Seneviratne, A. and Das, S.K., 2017. Harke: Human activity recognition from kinetic energy harvesting data in wearable devices. IEEE Transactions on Mobile Computing, 17(6), pp.1353-1368.
38. Xue, H., Yang, Q., Wang, D., Luo, W., Wang, W., Lin, M., Liang, D. and Luo, Q., 2017. A wearable pyroelectric nanogenerator and self-powered breathing sensor. Nano Energy, 38, pp.147-154.
39. Deterre, M., Lefeuvre, E., Zhu, Y., Woytasik, M., Boutaud, B. and Dal Molin, R., 2013. Micro blood pressure energy harvester for intracardiac pacemaker. Journal of Microelectromechanical Systems, 23(3), pp.651-660.
40. Hwang, G.T., Kim, Y., Lee, J.H., Oh, S., Jeong, C.K., Park, D.Y., Ryu, J., Kwon, H., Lee, S.G., Joung, B. and Kim, D., 2015. Self-powered deep brain stimulation via a flexible PIMNT energy harvester. Energy & Environmental Science, 8(9), pp.2677-2684.
41. Cheng, X., Xue, X., Ma, Y., Han, M., Zhang, W., Xu, Z., Zhang, H. and Zhang, H., 2016. Implantable and self-powered blood pressure monitoring based on a piezoelectric thinfilm: Simulated, in vitro and in vivo studies. Nano Energy, 22, pp.453-460.
42. Kim, D.H., Shin, H.J., Lee, H., Jeong, C.K., Park, H., Hwang, G.T., Lee, H.Y., Joe, D.J., Han, J.H., Lee, S.H. and Kim, J., 2017. In vivo self-powered wireless transmission using biocompatible flexible energy harvesters. Advanced Functional Materials, 27(25), p.1700341.
43. S. Matsusaka, H. Maruyama, T. Matsuyama, and M. Ghadiri, 2010, "Triboelectric charging of powders: A review," Chemical Engineering Science, 65, pp. 5781-5807.
44. W. Harper, 1951, "The Volta effect as a cause of static electrification," Proceedings of the Royal Society of London. Series A. Mathematical and Physical Sciences, 205, pp. 83-103.
45. D. Davies, 1969, "Charge generation on dielectric surfaces," Journal of Physics D: Applied Physics, 2, pp. 1533.

46. Y. Murata and S. Kittaka, "Evidence of electron transfer as the mechanism of static charge generation by contact of polymers with metals," Japanese Journal of Applied Physics, vol. 18, p. 421, 1979.
47. J. Henniker, 1962 "Triboelectricity in polymers," Nature, 196, p. 474.
48. A. Diaz and R. Felix-Navarro, 2004, "A semi-quantitative tribo-electric series for polymeric materials: the influence of chemical structure and properties," Journal of Electrostatics, 62, pp. 277-290.
49. Muthu, M., Pandey, R., Wang, X., Chandrasekhar, A., Palani, I.A. and Singh, V., 2020. Enhancement of triboelectric nanogenerator output performance by laser 3D-surface pattern method for energy harvesting application. Nano Energy, 78, p.105205.
50. Q. Jiang, C. Wu, Z. Wang, A.C. Wang, J.-H. He, Z.L. Wang, et al., 2018, "MXene electrochemical micro supercapacitor integrated with triboelectric nanogenerator as a wearable self-charging power unit", Nano Energy, 45, 266–272.
51. X. Pu, H. Guo, J. Chen, X. Wang, Y. Xi, C. Hu, 2017, Eye motion triggered self-powered mechno sensational communication system using triboelectric nanogenerator, Sci. Adv. 3, e1700694.
52. Q. Zheng, H. Zhang, B. Shi, X. Xue, Z. Liu, Y. Jin, 2016, In vivo self-powered wireless cardiac monitoring via implantable triboelectric nanogenerator, ACS Nano, 10, 6510–6518.
53. F. Arab Hassani, R.P. Mogan, G.G. Gammad, H. Wang, S.-C. Yen, N.V. Thakor, 2018, Toward self-control systems for neurogenic underactive bladder: a triboelectric nanogenerator sensor integrated with a bistable micro-actuator, ACS Nano, 12, 3487–3501.
54. Dhakar, L., 2017, Triboelectric devices for power generation and self-powered sensing applications. Springer.
55. C. Li, Y. Yin, B. Wang, T. Zhou, J. Wang, J. Luo, 2017, Self-powered electrospinning system driven by a triboelectric nanogenerator, ACS Nano, 11, 10439–10445.
56. Z. Li, J. Chen, H. Guo, X. Fan, Z. Wen, M.H. Yeh, 2016, Triboelectrification-enabled self-powered detection and removal of heavy metal ons in wastewater, Adv. Mater., 28, 2983–2991.

57. Y.S. Zhou, G. Zhu, S. Niu, Y. Liu, P. Bai, Q. Jing, 2014, Nano meter resolution self-powered static and dynamic motion sensor based on micro-grated triboelectrification, Adv. Mater. 26, 1719 1724.
58. J. Nie, Z. Ren, J. Shao, C. Deng, L. Xu, X. Chen, 2018, Self-powered microfluidic transport system based on triboelectric nanogenerator and electrowetting technique, ACS Nano 12, 1491–1499.
59. Mohith, S., Upadhya, A.R., Navin, K.P., Kulkarni, S.M. and Rao, M., 2020. Recent trends in piezoelectric actuators for precision motion and their applications: A review. Smart Materials and Structures, 30(1), p.013002.
60. Priya, S. and Inman, D.J. eds., 2009. Energy harvesting technologies New York: Springer, 21, p. 2.
61. Heywang, W., Lubitz, K. and Wersing, W. eds., 2008. Piezoelectricity: evolution and future of a technology, Springer Science & Business Media, 114.
62. MS Ramachandra Rao and Tatsuo Okada. ZnO nanocrystals and allied materials. Springer, 2014.
63. CW Bunn. “The lattice-dimensions of zinc oxide”. In: Proceedings of the Physical Society 47.5 (1935), p. 835.
64. Magnus Willander et al. “Zinc oxide nanorod based photonic devices: recent progress in growth, light emitting diodes and lasers”. In: Nanotechnology 20.33 (2009), p. 332001.
65. Ü Özgür et al. “A comprehensive review of ZnO materials and devices”. In: Journal of applied physics 98.4 (2005), p. 11.
66. Yang, R., Qin, Y., Dai, L. and Wang, ZL, Power Generation with Side-Packed Piezoelectric Fine Wires. Nature's Nanotechnology, 4 (1), pp.34-39.
67. Yang, R., Qin, Y., Li, C., Zhu, G. and Wang, Z.L., 2009. Converting biomechanical energy into electricity by a muscle-movement-driven nanogenerator. Nano letters, 9(3), pp.1201-1205.
68. Xu, S., Qin, Y., Xu, C., Wei, Y., Yang, R. and Wang, Z.L., 2010. Self-powered nanowire devices. Nature nanotechnology, 5(5), pp.366-373.

69. Zhu, G., Yang, R., Wang, S. and Wang, Z.L., 2010. Flexible high-output nanogenerator based on lateral ZnO nanowire array. Nano letters, 10(8), pp.3151-3155.
70. Hu, Y., Zhang, Y., Xu, C., Zhu, G. and Wang, Z.L., 2010. High-output nanogenerator by rational unipolar assembly of conical nanowires and its application for driving a small liquid crystal display. Nano letters, 10(12), pp.5025-5031.
71. Qin, Y., Wang, X. and Wang, Z.L., 2008. Microfibre–nanowire hybrid structure for energy scavenging. nature, 451(7180), pp.809-813.
72. Choi, D., Choi, M.Y., Choi, W.M., Shin, H.J., Park, H.K., Seo, J.S., Park, J., Yoon, S.M., Chae, S.J., Lee, Y.H. and Kim, S.W., 2010. Fully rollable transparent nanogenerators based on graphene electrodes. Advanced Materials, 22(19), pp.2187-2192.
73. Lee, S., Hinchet, R., Lee, Y., Yang, Y., Lin, Z.H., Ardila, G., Montès, L., Mouis, M. and Wang, Z.L., 2014. Ultrathin nanogenerators as self-powered/active skin sensors for tracking eye ball motion. Advanced Functional Materials, 24(8), pp.1163-1168.
74. Li, Z. and Wang, Z.L., 2011. Air/liquid-pressure and heartbeat-driven flexible fiber nanogenerators as a micro/nano-power source or diagnostic sensor. Advanced Materials, 23(1), pp.84-89.
75. Lee, M., Chen, C.Y., Wang, S., Cha, S.N., Park, Y.J., Kim, J.M., Chou, L.J. and Wang, Z.L., 2012. A hybrid piezoelectric structure for wearable nanogenerators. Advanced Materials, 24(13), pp.1759-1764.
76. Fukumura, T., Jin, Z., Ohtomo, A., Koinuma, H. and Kawasaki, M., 1999. An oxide-diluted magnetic semiconductor: Mn-doped ZnO. Applied physics letters, 75(21), pp.3366-3368.
77. Zhao, M.H., Wang, Z.L. and Mao, S.X., 2004. Piezoelectric characterization of individual zinc oxide nanobelt probed by piezo response force microscope. Nano Letters, 4(4), pp.587-590.
78. Yang, Y.C., Song, C., Wang, X.H., Zeng, F. and Pan, F., 2008. Giant piezoelectric d 33 coefficient in ferroelectric vanadium doped ZnO films. Applied Physics Letters, 92(1), p.012907.

79. Yang, Y.C., Song, C., Zeng, F., Pan, F., Xie, Y.N. and Liu, T., 2007. V 5+ ionic displacement induced ferroelectric behavior in V-doped ZnO films. Applied physics letters, 90(24), p.242903.
80. Gupta, M.K., Lee, J.H., Lee, K.Y. and Kim, S.W., 2013. Two-dimensional vanadium-doped ZnO nanosheet-based flexible direct current nanogenerator. ACS nano, 7(10), pp.8932-8939.
81. Ong, W.L., Huang, H., Xiao, J., Zeng, K. and Ho, G.W., 2014. Tuning of multifunctional Cu-doped ZnO films and nanowires for enhanced piezo/ferroelectric-like and gas/photoresponse properties. Nanoscale, 6(3), pp.1680-1690.
82. Lee, K.M., Lai, C.W., Ngai, K.S. and Juan, J.C., 2016. Recent developments of zinc oxide based photocatalyst in water treatment technology: a review. Water research, 88, pp.428-448.
83. Liu, Y., Li, Y. and Zeng, H., 2013. ZnO-based transparent conductive thin films: doping, performance, and processing. Journal of Nanomaterials, 2013.
84. Schmidt-Mende, L. and MacManus-Driscoll, J.L., 2007. ZnO–nanostructures, defects, and devices. Materials today, 10(5), pp.40-48.
85. Agrawal, J., Dixit, T., Palani, I.A. and Singh, V., 2019. Development of Al Doped ZnO nanowalls based flexible, ultralow voltage UV photodetector. IEEE Sensors Letters, 3(9), pp.1-4.
86. Li, S.Y., Lin, P., Lee, C.Y., Tseng, T.Y. and Huang, C.J., 2004. Effect of Sn dopant on the properties of ZnO nanowires. Journal of Physics D: Applied Physics, 37(16), p.2274.
87. Ajili, M., Castagné, M. and Turki, N.K., 2013. Study on the doping effect of Sn-doped ZnO thin films. Superlattices and Microstructures, 53, pp.213-222.
88. Tsay, C.Y., Cheng, H.C., Tung, Y.T., Tuan, W.H. and Lin, C.K., 2008. Effect of Sn-doped on microstructural and optical properties of ZnO thin films deposited by sol–gel method. Thin Solid Films, 517(3), pp.1032-1036.
89. Ismail, A.S., Mamat, M.H., Banu, I.S., Malek, M.F., Yusoff, M.M., Mohamed, R., Ahmad, W.R.W., Abdullah, M.A.R., Sin, N.M.,

Suriani, A.B. and Ahmad, M.K., 2018. Modulation of Sn concentration in ZnO nanorod array: intensification on the conductivity and humidity sensing properties. Journal of Materials Science: Materials in Electronics, 29(14), pp.12076-12088.

90. Rakshit, T., Manna, I. and Ray, S.K., 2013. Shape controlled Sn doped ZnO nanostructures for tunable optical emission and transport properties. AIP Advances, 3(11), p.112112.
91. Ravichandran, K., Vasanthi, M., Thirumurugan, K., Sakthivel, B. and Karthika, K., 2014. Annealing induced reorientation of crystallites in Sn doped ZnO films. Optical Materials, 37, pp.59-64.
92. Chen, S.W., Cao, X., Wang, N., Ma, L., Zhu, H.R., Willander, M., Jie, Y. and Wang, Z.L., 2017. An ultrathin flexible single-electrode triboelectric-nanogenerator for mechanical energy harvesting and instantaneous force sensing. Advanced Energy Materials, 7(1), p.1601255.
93. Ra, Y., Choi, J.H., Choi, S.J., La, M., Park, S.J., Kim, M.J. and Choi, D., 2020. Cold rolled robust metal assisted triboelectric nanogenerator for extremely durable operation. Extreme Mechanics Letters, 40, p.100910.
94. Lin, L., Wang, S., Niu, S., Liu, C., Xie, Y. and Wang, Z.L., 2014. Noncontact free-rotating disk triboelectric nanogenerator as a sustainable energy harvester and self-powered mechanical sensor. ACS applied materials & interfaces, 6(4), pp.3031-3038.
95. Stanford, M.G., Li, J.T., Chyan, Y., Wang, Z., Wang, W. and Tour, J.M., 2019. Laser-induced graphene triboelectric nanogenerators. ACS nano, 13(6), pp.7166-7174.
96. Chung, C.K. and Ke, K.H., 2020. High contact surface area enhanced Al/PDMS triboelectric nanogenerator using novel overlapped microneedle arrays and its application to lighting and self-powered devices. Applied Surface Science, 508, p.145310.
97. Phan, H., Hoa, P.N., Tam, H.A., Thang, P.D. and Duc, N.H., 2020. Multi-directional triboelectric nanogenerator based on industrial Q-switched pulsed laser etched Aluminum film. Extreme Mechanics Letters, 40, p.100886.

98. Wang, R., Gao, S., Yang, Z., Li, Y., Chen, W., Wu, B. and Wu, W., 2018. Engineered and laser-processed chitosan biopolymers for sustainable and biodegradable triboelectric power generation. Advanced Materials, 30(11), p.1706267.
99. Chen, Y., Xie, B., Long, J., Kuang, Y., Chen, X., Hou, M., Gao, J., Zhou, S., Fan, B., He, Y. and Zhang, Y.T., 2021. Interfacial Laser-Induced Graphene Enabling High-Performance Liquid− Solid Triboelectric Nanogenerator. Advanced Materials, 33(44), p.2104290.
100. Zhang, X.S., Han, M.D., Wang, R.X., Zhu, F.Y., Li, Z.H., Wang, W. and Zhang, H.X., 2013. Frequency-multiplication high-output triboelectric nanogenerator for sustainably powering biomedical microsystems. Nano letters, 13(3), pp.1168-1172.
101. Hu, Y., Wang, X., Li, H., Li, H. and Li, Z., 2020. Effect of humidity on tribological properties and electrification performance of sliding-mode triboelectric nanogenerator. Nano Energy, 71, p.104640.
102. Fan, F.R., Lin, L., Zhu, G., Wu, W., Zhang, R. and Wang, Z.L., 2012. Transparent triboelectric nanogenerators and self-powered pressure sensors based on micropatterned plastic films. Nano letters, 12(6), pp.3109-3114.
103. Bui, V.T., Zhou, Q., Kim, J.N., Oh, J.H., Han, K.W., Choi, H.S., Kim, S.W. and Oh, I.K., 2019. Treefrog toe pad-inspired micropatterning for high-power triboelectric nanogenerator. Advanced Functional Materials, 29(28), p.1901638.
104. Mule, A.R., Dudem, B. and Yu, J.S., 2018. High-performance and cost-effective triboelectric nanogenerators by sandpaper-assisted micropatterned polytetrafluoroethylene. Energy, 165, pp.677-684.
105. Rabek, J.F., 2012. Polymer photodegradation: mechanisms and experimental methods. Springer Science & Business Media. Springer Science & Business Media, 2012, chapter-9.
106. Greiner, C., Merz, T., Braun, D., Codrignani, A. and Magagnato, F., 2015. Optimum dimple diameter for friction reduction with laser surface texturing: the effect of velocity gradient. Surface Topography: Metrology and Properties, 3(4), p.044001.

107. Riveiro, A., Chantada, A., Soto, R., del Val, J., Arias-González, F., Comesaña, R., Boutinguiza, M., Quintero, F., Lusquiños, F. and Pou, J., 2019. Laser surface texturing of thermoplastics to improve biological performance. In Materials for Biomedical Engineering (pp. 29-56). Elsevier.
108. Huang, J., Fu, X., Liu, G., Xu, S., Li, X., Zhang, C. and Jiang, L., 2019. Micro/nano-structures-enhanced triboelectric nanogenerators by femtosecond laser direct writing. Nano Energy, 62, pp.638-644.
109. Wang, R., Gao, S., Yang, Z., Li, Y., Chen, W., Wu, B. and Wu, W., 2018. Engineered and laser-processed chitosan biopolymers for sustainable and biodegradable triboelectric power generation. Advanced Materials, 30(11), p.1706267.
110. Kim, D., Tcho, I.W., Jin, I.K., Park, S.J., Jeon, S.B., Kim, W.G., Cho, H.S., Lee, H.S., Jeoung, S.C. and Choi, Y.K., 2017. Direct-laser-patterned friction layer for the output enhancement of a triboelectric nanogenerator. Nano Energy, 35, pp.379-386.
111. Goel, S., Sinha, N., Yadav, H., Joseph, A.J. and Kumar, B., 2017. Experimental investigation on the structural, dielectric, ferroelectric and piezoelectric properties of La doped ZnO nanoparticles and their application in dye-sensitized solar cells. Physica E: Low-dimensional Systems and Nanostructures, 91, pp.72-81
112. Baviskar, P.K., Nikam, P.R., Gargote, S.S., Ennaoui, A. and Sankapal, B.R., 2013. Controlled synthesis of ZnO nanostructures with assorted morphologies via simple solution chemistry. Journal of Alloys and Compounds, 551, pp.233-242.
113. Baruah, S. and Dutta, J., 2009. Hydrothermal growth of ZnO nanostructures. Science and technology of advanced materials, 10(1), p.013001.
114. Strano, V., Urso, R.G., Scuderi, M., Iwu, K.O., Simone, F., Ciliberto, E., Spinella, C. and Mirabella, S., 2014. Double role of HMTA in ZnO nanorods grown by chemical bath deposition. The Journal of Physical Chemistry C, 118(48), pp.28189-28195

115. Shishiyanu, S.T., Shishiyanu, T.S. and Lupan, O.I., 2005. Sensing characteristics of tin-doped ZnO thin films as NO2 gas sensor. Sensors and Actuators B: Chemical, 107(1), pp.379-386.
116. Selvakumar, M., Bhat, D.K., Aggarwal, A.M., Iyer, S.P. and Sravani, G., 2010. Nano ZnO-activated carbon composite electrodes for supercapacitors. Physica B: Condensed Matter, 405(9), pp.2286-2289
117. Nour, E.S., Sandberg, M.O., Willander, M. and Nur, O., 2014. Handwriting enabled harvested piezoelectric power using ZnO nanowires/polymer composite on paper substrate. Nano energy, 9, pp.221-22.
118. Chandrakala, H.N., Ramaraj, B. and Lee, J.H., 2013. Polyvinyl alcohol/carbon coated zinc oxide nanocomposites: Electrical, optical, structural and morphological characteristics. Journal of Alloys and Compounds, 580, pp.392-400.
119. Hmar, J.J.L., 2018. Flexible resistive switching bistable memory devices using ZnO nanoparticles embedded in polyvinyl alcohol (PVA) matrix and poly (3, 4-ethylenedioxythiophene) polystyrene sulfonate (PEDOT: PSS). RSC advances, 8(36), pp.20423-20433
120. Sheini, F.J., More, M.A., Jadkar, S.R., Patil, K.R., Pillai, V.K. and Joag, D.S., 2010. Observation of photoconductivity in Sn-doped ZnO nanowires and their photo enhanced field emission behavior. The Journal of Physical Chemistry C, 114(9), pp.3843-3849
121. Mohamed, R., Mamat, M.H., Ismail, A.S., Malek, M.F., Zoolfakar, A.S., Khusaimi, Z., Suriani, A.B., Mohamed, A., Ahmad, M.K. and Rusop, M., 2017. Hierarchically assembled tin-doped zinc oxide nanorods using low-temperature immersion route for low temperature ethanol sensing. Journal of Materials Science: Materials in Electronics, 28(21), pp.16292-16305.
122. Russo, V., Ghidelli, M., Gondoni, P., Casari, C.S. and Li Bassi, A., 2014. Multi-wavelength Raman scattering of nanostructured Al-doped zinc oxide. Journal of Applied Physics, 115(7), p.073508.
123. Júnior, E.A.A., Nobre, F.X., da Silva Sousa, G., Cavalcante, L.S., Santos, M.R.D.M.C., Souza, F.L. and de Matos, J.M.E., 2017.

Synthesis, growth mechanism, optical properties and catalytic activity of ZnO microcrystals obtained via hydrothermal processing. RSC Advances, 7(39), pp.24263-24281.

124. Rajagopalan, P., Khandelwal, G., Palani, I.A., Singh, V. and Kim, S.J., 2019. La-doped ZnO ultra-flexible flutter-Piezoelectric Nanogenerator for Energy Harvesting and Sensing Applications: A Novel Renewable Source of Energy. Nanoscale.

125. Pan, Z., Zhang, P., Tian, X., Cheng, G., Xie, Y., Zhang, H., Zeng, X., Xiao, C., Hu, G. and Wei, Z., 2013. Properties of fluorine and tin co-doped ZnO thin films deposited by sol–gel method. Journal of Alloys and Compounds, 576, pp.31-37.

126. Ganesh, V., Yahia, I.S., AlFaify, S. and Shkir, M., 2017. Sn-doped ZnO nanocrystalline thin films with enhanced linear and nonlinear optical properties for optoelectronic applications. Journal of Physics and Chemistry of Solids, 100, pp.115-125.

127. Junlabhut, P., Mekprasart, W., Noonuruk, R., Chongsri, K. and Pecharapa, W., 2014. Characterization of ZnO: Sn nanopowders synthesized by co-precipitation method. Energy Procedia, 56, pp.560-565.

128. Ameen, S., Akhtar, M.S., Seo, H.K., Kim, Y.S. and Shin, H.S., 2012. Influence of Sn doping on ZnO nanostructures from nanoparticles to spindle shape and their photoelectrochemical properties for dye sensitized solar cells. Chemical Engineering Journal, 187, pp.351-356.

129. Yamani, Z.H., Iqbal, J., Qurashi, A. and Hakeem, A., 2014. Rapid sonochemical synthesis of In2O3 nanoparticles their doping optical, electrical and hydrogen gas sensing properties. Journal of Alloys and Compounds, 616, pp.76-80.

130. Junlabhut, P., Mekprasart, W., Noonuruk, R., Chongsri, K. and Pecharapa, W., 2014. Characterization of ZnO: Sn nanopowders synthesized by co-precipitation method. Energy Procedia, 56, pp.560-565.

131. Arif, M., Shkir, M., AlFaify, S., Ganesh, V., Sanger, A., Algarni, H., Vilarinho, P.M. and Singh, A., 2019. A structural,

morphological, linear, and nonlinear optical spectroscopic studies of nanostructured Al-doped ZnO thin films: An effect of Al concentrations. Journal of Materials Research, 34(8), pp.1309-1317

132. Agarwal, M.B., Sharma, A., Malaidurai, M. and Thangavel, R., 2018. Effect of Sn doping on structural, mechanical, optical and electrical properties of ZnO nanoarrays prepared by sol-gel and hydrothermal process. Superlattices and Microstructures, 117, pp.342-350.

133. Fakhri, P., Amini, B., Bagherzadeh, R., Kashfi, M., Latifi, M., Yavari, N., Kani, S.A. and Kong, L., 2019. Flexible hybrid structure piezoelectric nanogenerator based on ZnO nanorod/PVDF nanofibers with improved output. RSC advances, 9(18), pp.10117-10123.

134. Shin, S.H., Kwon, Y.H., Lee, M.H., Jung, J.Y., Seol, J.H. and Nah, J., 2016. A vanadium-doped ZnO nanosheets–polymer composite for flexible piezoelectric nanogenerators. Nanoscale, 8(3), pp.1314-1321.

135. Bougrine, A., Addou, M., Kachouane, A., Bérnède, J.C. and Morsli, M., 2005. Effect of tin incorporation on physicochemical properties of ZnO films prepared by spray pyrolysis. Materials Chemistry and Physics, 91(2-3), pp.247-252

136. Rajagopalan, P., Singh, V. and Palani, I.A., 2018. Enhancement of ZnO-based flexible nano generators via a sol–gel technique for sensing and energy harvesting applications. Nanotechnology, 29(10), p.105406.

137. Sheini, F.J., Joag, D.S. and More, M.A., 2010. Electrochemical synthesis of Sn doped ZnO nanowires on zinc foil and their field emission studies. Thin Solid Films, 519(1), pp.184-189.

138. Alam, M.M. and Mandal, D., 2016. Native cellulose microfiber-based hybrid piezoelectric generator for mechanical energy harvesting utility. ACS applied materials & interfaces, 8(3), pp.1555-1558.

139. Kim, K.H., Lee, K.Y., Seo, J.S., Kumar, B. and Kim, S.W., 2011. Paper-based piezoelectric nanogenerators with high thermal stability. Small, 7(18), pp.2577-2580.
140. Liu, S., Zheng, W., Yang, B. and Tao, X., 2018. Triboelectric charge density of porous and deformable fabrics made from polymer fibers. Nano energy, 53, pp.383-390.
141. Zhao, P., Soin, N., Prashanthi, K., Chen, J., Dong, S., Zhou, E., Zhu, Z., Narasimulu, A.A., Montemagno, C.D., Yu, L. and Luo, J., 2018. Emulsion electrospinning of polytetrafluoroethylene (PTFE) nanofibrous membranes for high-performance triboelectric nanogenerators. ACS applied materials & interfaces, 10(6), pp.5880-5891.
142. Soin, N., Zhao, P., Prashanthi, K., Chen, J., Ding, P., Zhou, E., Shah, T., Ray, S.C., Tsonos, C., Thundat, T. and Siores, E., 2016. High performance triboelectric nanogenerators based on phase-inversion piezoelectric membranes of poly (vinylidene fluoride)-zinc stannate (PVDF-ZnSnO3) and polyamide-6 (PA6). Nano Energy, 30, pp.470-480.
143. Dhakar, L., Gudla, S., Shan, X., Wang, Z., Tay, F.E.H., Heng, C.H. and Lee, C., 2016. Large scale triboelectric nanogenerator and self-powered pressure sensor array using low-cost roll-to-roll UV embossing. Scientific reports, 6, p.22253.
144. Rebollar, E., Pérez, S., Hernández, M., Domingo, C., Martín, M., Ezquerra, T.A., García-Ruiz, J.P. and Castillejo, M., 2014. Physicochemical modifications accompanying UV laser induced surface structures on poly (ethylene terephthalate) and their effect on adhesion of mesenchymal cells. Physical Chemistry Chemical Physics, 16(33), pp.17551-17559.
145. Ma, C., Gao, S., Gao, X., Wu, M., Wang, R., Wang, Y., Tang, Z., Fan, F., Wu, W., Wan, H. and Wu, W., 2019. Chitosan biopolymer-derived self-powered triboelectric sensor with optimized performance through molecular surface engineering and data-driven learning. InfoMat, 1(1), pp.116-125.

146. Shin, S.H., Park, D., Jung, J.Y., Park, P. and Nah, J., 2018. An ultraviolet and electric field activated photopolymer–ferroelectric nanoparticle composite for the performance enhancement of triboelectric nanogenerators. Nanoscale, 10(45), pp.20995-21000.
147. Wang, Z.L., Lin, L., Chen, J., Niu, S. and Zi, Y., 2016. Triboelectric nanogenerators. Berlin, Germany: Springer International Publishing, chapter 2.
148. Jeong, C.K., Baek, K.M., Niu, S., Nam, T.W., Hur, Y.H., Park, D.Y., Hwang, G.T., Byun, M., Wang, Z.L., Jung, Y.S. and Lee, K.J., 2014. Topographically-designed triboelectric nanogenerator via block copolymer self-assembly. Nano letters, 14(12), pp.7031-7038.
149. Zhang, X.W., Li, G.Z., Wang, G.G., Tian, J.L., Liu, Y.L., Ye, D.M., Liu, Z., Zhang, H.Y. and Han, J.C., 2018. High-performance triboelectric nanogenerator with double-surface shape-complementary microstructures prepared by using simple sandpaper templates. ACS Sustainable Chemistry & Engineering, 6(2), pp.2283-2291.
150. Ding, P., Chen, J., Farooq, U., Zhao, P., Soin, N., Yu, L., Jin, H., Wang, X., Dong, S. and Luo, J., 2018. Realizing the potential of polyethylene oxide as new positive tribo-material: Over 40 W/m2 high power flat surface triboelectric nanogenerators. Nano energy, 46, pp.63-72.
151. Xia, K., Chi, Y., Fu, J., Zhu, Z., Zhang, H., Du, C. and Xu, Z., 2019. A triboelectric nanogenerator based on cosmetic fixing powder for mechanical energy harvesting. Microsystems & nanoengineering, 5(1), pp.1-9.
152. Wang, S., Lin, L. and Wang, Z.L., 2012. Nanoscale triboelectric-effect-enabled energy conversion for sustainably powering portable electronics. Nano letters, 12(12), pp.6339-6346.
153. Pan, R., Xuan, W., Chen, J., Dong, S., Jin, H., Wang, X., Li, H. and Luo, J., 2018. Fully biodegradable triboelectric nanogenerators based on electrospun polylactic acid and nanostructured gelatin films. Nano Energy, 45, pp.193-202.

154. Dudem, B., Kim, D.H., Mule, A.R. and Yu, J.S., 2018. Enhanced performance of microarchitectured PTFE-based triboelectric nanogenerator via simple thermal imprinting lithography for self-powered electronics. ACS applied materials & interfaces, 10(28), pp.24181-24192.
155. Saadatnia, Z., Esmailzadeh, E. and Naguib, H.E., 2019. High Performance Triboelectric Nanogenerator by Hot Embossing on Self-Assembled Micro-Particles. Advanced Engineering Materials, 21(1), p.1700957.
156. Seol, M.L., Han, J.W., Moon, D.I. and Meyyappan, M., 2017. Hysteretic behavior of contact force response in triboelectric nanogenerator. Nano Energy, 32, pp.408-413.
157. Wang, A.E., Gil, P.S., Holonga, M., Yavuz, Z., Baytekin, H.T., Sankaran, R.M. and Lacks, D.J., 2017. Dependence of triboelectric charging behavior on material microstructure. Physical Review Materials, 1(3), p.035605.
158. Sow, M., Widenor, R., Kumar, A., Lee, S.W., Lacks, D.J. and Sankaran, R.M., 2012. Strain-Induced Reversal of Charge Transfer in Contact Electrification. Angewandte Chemie International Edition, 51(11), pp.2695-2697.
159. Rajagopalan, P., Huang, S., Shi, L., Kuang, H., Jin, H., Dong, S., Shi, W., Wang, X. and Luo, J., 2021. Novel insights from the ultra-thin film, strain-modulated dynamic triboelectric characterizations. Nano Energy, 80, p.105560.
160. Chen, A., Zhang, C., Zhu, G. and Wang, Z.L., 2020. Polymer materials for high-performance triboelectric Nanogenerators. Advanced Science, 7(14), p.2000186.
161. Shao, J.J., Tang, W., Jiang, T., Chen, X.Y., Xu, L., Chen, B.D., Zhou, T., Deng, C.R. and Wang, Z.L., 2017. A multi-dielectric-layered triboelectric nanogenerator as energized by corona discharge. Nanoscale, 9(27), pp.9668-9675.
162. Wang, H.S., Jeong, C.K., Seo, M.H., Joe, D.J., Han, J.H., Yoon, J.B. and Lee, K.J., 2017. Performance-enhanced triboelectric

nanogenerator enabled by wafer-scale nanograte of multistep pattern downscaling. Nano Energy, 35, pp.415-423.

163. Chun, J., Ye, B.U., Lee, J.W., Choi, D., Kang, C.Y., Kim, S.W., Wang, Z.L. and Baik, J.M., 2016. Boosted output performance of triboelectric nanogenerator via electric double layer effect. Nature communications, 7(1), pp.1-9.
164. Elashmawi, I.S. and Gaabour, L.H., 2015. Raman, morphology and electrical behavior of nanocomposites based on PEO/PVDF with multi-walled carbon nanotubes. Results in Physics, 5, pp.105-110.
165. Chen, A., Zhang, C., Zhu, G. and Wang, Z.L., 2020. Polymer materials for high-performance triboelectric Nanogenerators. Advanced Science, 7(14), p.2000186.
166. Zou, H., Zhang, Y., Guo, L., Wang, P., He, X., Dai, G., Zheng, H., Chen, C., Wang, A.C., Xu, C. and Wang, Z.L., 2019. Quantifying the triboelectric series. Nature communications, 10(1), pp.1-9.
167. Kim, D.W., Lee, J.H., Kim, J.K. and Jeong, U., 2020. Material aspects of triboelectric energy generation and sensors. NPG Asia Materials, 12(1), pp.1-17.
168. Yoo, D., Go, E.Y., Choi, D., Lee, J.W., Song, I., Sim, J.Y., Hwang, W. and Kim, D.S., 2019. Increased interfacial area between dielectric layer and electrode of triboelectric nanogenerator toward robustness and boosted energy output. Nanomaterials, 9(1), p.71.
169. Wu, J.M., Lin, Y.H. and Yang, B.Z., 2016. Force-pad made from contact-electrification poly (ethylene oxide)/InSb field-effect transistor. Nano Energy, 22, pp.468-474.
170. Raman, V., Jo, J. and Kim, H.K., 2020. ITO and graphene-covered Ag grids embedded in PET substrate by thermal roll imprinting for flexible organic solar cells. Materials Science in Semiconductor Processing, 120, p.105277.
171. Xiong, J., Cui, P., Chen, X., Wang, J., Parida, K., Lin, M.F. and Lee, P.S., 2018. Skin-touch-actuated textile-based triboelectric

nanogenerator with black phosphorus for durable biomechanical energy harvesting. Nature communications, 9(1), pp.1-9.

172. Zhang, M., Xia, L., Dang, S., Shi, L., Cao, A., Deng, Q. and Du, C., 2019. A flexible single-electrode-based triboelectric nanogenerator based on double-sided nanostructures. AIP Advances, 9(7), p.075221.
173. Seol, M.L., Lee, S.H., Han, J.W., Kim, D., Cho, G.H. and Choi, Y.K., 2015. Impact of contact pressure on output voltage of triboelectric nanogenerator based on deformation of interfacial structures. Nano Energy, 17, pp.63-71.
174. Chandrasekhar, A., Alluri, N.R., Sudhakaran, M.S.P., Mok, Y.S. and Kim, S.J., 2017. A smart mobile pouch as a biomechanical energy harvester towards self-powered smart wireless power transfer applications. Nanoscale, 9(28), pp.9818-9824.
175. Nozariasbmarz, A., Collins, H., Dsouza, K., Polash, M.H., Hosseini, M., Hyland, M., Liu, J., Malhotra, A., Ortiz, F.M., Mohaddes, F. and Ramesh, V.P., 2020. Review of wearable thermoelectric energy harvesting: From body temperature to electronic systems. Applied Energy, 258, p.114069.